Energy Reviews 5 (2026) 100216

Contents lists available at ScienceDirect

Energy Reviews

journal homepage: www.journals.elsevier.com/energy-reviews

Full Review Article

Advanced engineering of inorganic semiconductor nanowires: Materials-by-design for next-generation green energy technologies

Sunday Temitope Oyinbo [a,*], Hoe-Gil Lee [a], Sikiru Oluwarotimi Ismail [b], Tien-Chien Jen [c]

[a] Department of Mechanical, Environmental, and Civil Engineering, Tarleton State University, Stephenville, TX, 76402, United States
[b] Department of Engineering, Centre for Engineering Research, School of Physics, Engineering and Computer Science, University of Hertfordshire, England, AL10 9AB, UK
[c] Department of Mechanical Engineering Science, University of Johannesburg, South Africa

ARTICLE INFO

Keywords:
Inorganic semiconductor NWs
Intelligent materials engineering
Computational materials design
Artificial intelligence
Sustainable energy technologies

ABSTRACT

Inorganic semiconductor nanowires (NWs) provide an unusually versatile platform for green-energy technologies because composition, crystal phase, defects, interfaces, morphology, and dimensionality can be engineered across multiple length scales. This review critically examines how these coupled design variables govern charge generation and transport, surface recombination, catalytic activity, ion diffusion, thermal transport, and operational stability. Rather than cataloguing individual materials, we identify transferable structure–property–performance relationships across photovoltaics, photoelectrochemical water splitting, photocatalysis, electrochemical energy storage, and thermoelectric conversion. A central conclusion is that nanoscale advantages are intrinsically conditional: reduced dimensions can enhance light trapping, carrier collection, reaction kinetics, and strain accommodation, but simultaneously intensify surface recombination, interfacial instability, defect sensitivity, and integration losses. We therefore evaluate competing engineering strategies in terms of these trade-offs and their implications for device-scale performance, durability, manufacturability, and sustainability. Recent advances in operando characterization, multiscale simulation, density functional theory, machine learning, and active learning are further assessed as tools for connecting synthesis conditions with experimentally validated material states and functional performance. Particular attention is given to the remaining gap between idealized computational predictions and structurally complex experimental NWs. Finally, we identify reproducibility, standardized data, device integration, scalable manufacturing, long-term stability, and uncertainty-aware human-supervised automation as critical requirements for translating semiconductor NWs from laboratory optimization toward deployable green-energy systems.

1. Introduction

Semiconductor nanowire (NW) research has progressed from the demonstration of one-dimensional crystal growth to the deliberate engineering of composition, interfaces, defects, and device functionality. The vapor–liquid–solid mechanism established the catalytic basis for anisotropic single-crystal growth [1,2], while laser-ablation synthesis later demonstrated controlled production of crystalline semiconductor NWs across technologically relevant material systems [3,4]. These advances positioned NWs as quasi-one-dimensional building blocks whose electronic and optical behavior can differ substantially from bulk and thin-film counterparts because of radial confinement, large surface-to-volume ratios, directional carrier transport, and geometry-dependent light–matter interactions [5–9]. Subsequent developments in catalyst selection, epitaxy, doping, heterostructure formation, and substrate integration expanded the field from exploratory synthesis to functional device engineering [10–14].

The current scientific challenge is no longer simply whether a semiconductor NW can be synthesized, but whether its atomic structure, surface chemistry, interfaces, defects, and operating environment can be controlled sufficiently to deliver reproducible performance. Nominally identical NWs may exhibit markedly different carrier lifetimes, mobilities, surface recombination velocities, catalytic activities, and degradation rates because of variations in diameter, tapering, crystal phase, stacking-fault density, dopant activation, native oxides, and contact resistance. Such variations become increasingly consequential when NWs are assembled into large-area arrays, hierarchical architectures, or integrated devices. Therefore, synthesis-centered approaches must

* Corresponding author.
E-mail address: soyinbo@tarleton.edu (S.T. Oyinbo).

https://doi.org/10.1016/j.enrev.2026.100216
Received 27 July 2026; Received in revised form 18 September 2026; Accepted 30 September 2026
2772-9702/Published by Elsevier Ltd on behalf of State Key Laboratory of Intelligent Construction and Healthy Operation and Maintenance of Deep Underground Engineering, Shenzhen University. This is an open access article under the CC BY license (http://creativecommons.org/licenses/by/4.0/).

evolve toward materials engineering frameworks in which growth, structure, chemistry, properties, and performance are optimized concurrently.

This transition is particularly important for green-energy technologies. Semiconductor NWs can decouple optical absorption from carrier-collection length, intensify electromagnetic fields, expose large catalytic surface areas, and provide direct pathways for electron, hole, ion, and phonon transport [15,16]. Radial and axial junctions have enabled single-NW and array-based photovoltaic (PV) devices [16,17], while integrated semiconductor–catalyst architectures have demonstrated direct solar-water splitting [17]. In electrochemical storage, one-dimensional structures accommodate reaction-induced strain and shorten ion-diffusion distances, although their high surface area may also accelerate interphase formation and parasitic reactions [18,19]. Similar structure-dependent benefits have been reported in photocatalysis, thermoelectric conversion, piezoelectric harvesting, and electrocatalysis [19,20]. These advantages are therefore conditional rather than intrinsic: performance gains occur only when surface recombination, unstable interfaces, defect-assisted trapping, contact losses, catalyst detachment, and chemical degradation are adequately controlled.

Computational materials science now provides a route for replacing sequential experimental optimization with predictive design. Density functional theory (DFT) can quantify surface energies, band offsets, defect formation energies, adsorption thermodynamics, and reaction barriers; molecular dynamics (MD) can resolve temperature-dependent growth and interface evolution; phase-field and continuum models can describe morphology, transport, and device-scale responses. These methods are increasingly coupled with high-throughput screening, machine learning (ML), and uncertainty-aware optimization to navigate composition–structure–process spaces that are too large for exhaustive experimentation. However, predictive reliability remains constrained by model fidelity, scarce standardized datasets, differences between idealized calculations and real NW surfaces, and limited transferability across material classes.

The next stage is consequently computational intelligence, in which simulations, experiments, characterization data, and manufacturing parameters form a continuously learning materials-development system. Artificial intelligence (AI) can identify hidden synthesis–structure–property relationships, automate microscopy and spectroscopy, and guide experiment selection. Scientific ML can impose conservation laws and transport equations on data-driven models, while digital twins can continuously synchronize physical NW synthesis or device operation with virtual representations. When integrated with robotic synthesis and autonomous characterization, these capabilities could establish closed-loop laboratories that select, execute, evaluate, and refine experiments with progressively reduced human intervention.

The breadth of semiconductor NW research makes an exhaustive material-by-material catalogue neither practical nor particularly instructive. Accordingly, this review is organized around three interconnected questions: how NW structure is engineered, how the resulting material state is established experimentally, and how these relationships translate into energy-device performance and durability. Individual material systems and characterization techniques are therefore treated as representative case studies within this structure-property-performance framework rather than as independent topics of equal weight. This approach enables comparison of transferable mechanisms, including confinement, surface recombination, defect-mediated transport, band alignment, strain accommodation, interfacial charge transfer, and ion diffusion, across otherwise dissimilar NW systems.

Rather than evaluating semiconductor NWs solely by material class or application-specific record performance, this review examines the field through a materials-by-design framework that connects controllable structural descriptors with experimentally measurable properties, device-level performance, degradation, and manufacturability. The central question is therefore not which NW material is universally superior, but which combinations of composition, crystal phase, defects, interfaces, dimensions, and processing conditions produce the required balance of transport, reactivity, stability, scalability, and sustainability for a particular energy function. This framework also provides the basis for evaluating where computational prediction and data-driven optimization are sufficiently validated for engineering decisions and where experimental complexity continues to limit predictive transferability.

Accordingly, this review progresses from materials engineering and interface engineering to advanced characterization, sustainable manufacturing, and autonomous NW discovery. The evolution of inorganic semiconductor NWs has progressed far beyond the early demonstration of one-dimensional crystal growth toward an integrated paradigm that combines advanced materials engineering, interface design, computational intelligence, multiscale characterization, sustainable manufacturing, and autonomous scientific discovery [21]. Fig. 1 summarizes the conceptual evolution of inorganic semiconducting NW research over the past two decades and provides the organizing framework for this review. Early investigations primarily focused on catalyst-assisted crystal growth and the demonstration of fundamental one-dimensional semiconductor properties [5,22]. Subsequent research shifted toward precise control of composition, crystal structure, doping, heterostructure formation, and surface chemistry to enhance electronic and optical performance [6,7,10,11]. As NW-based devices matured, increasing attention was devoted to interface engineering, defect management, and multifunctional device integration for photovoltaics, photoelectrochemical (PEC) water splitting, photocatalysis, electrochemical energy storage, thermoelectric conversion, and flexible electronics [12–14]. More recently, advances in computational materials science, DFT, high-throughput simulations, ML, and digital engineering have transformed NW research from empirical optimization toward predictive materials design [13,19,23]. Emerging technologies—including autonomous synthesis, robotic experimentation, AI, scientific ML, and digital twins—are expected to establish self-improving materials discovery ecosystems capable of continuously accelerating innovation. The subsequent sections of this review follow this scientific progression, emphasizing the integration of materials engineering, computational intelligence, advanced characterization, sustainable manufacturing, and autonomous discovery as the foundation for next-generation semiconductor NW technologies.

2. Advanced nanowire materials engineering

2.1. Material classification and electronic structure engineering

The exceptional versatility of inorganic semiconductor NWs arises from the ability to tailor their electronic structure through simultaneous control of composition, crystal structure, dimensionality, and surface chemistry. Unlike bulk semiconductors, whose properties are primarily governed by intrinsic crystal chemistry, NWs introduce additional design variables including quantum confinement, high surface-to-volume ratios, anisotropic charge transport, and engineered interfaces. Consequently, their functional performance is determined by the coupled interactions among composition, defects, morphology, and surface electronic states rather than by bandgap alone [30–32]. This integrated materials engineering approach has established semiconductor NWs as leading candidates for photovoltaic cells, PEC water splitting, photocatalysis, thermoelectric devices, lithium-ion batteries (LIBs), and electrochemical energy storage [33–35].

The hierarchical materials engineering strategy adopted throughout this review is illustrated in Fig. 2, which links atomic composition to crystal structure, defect chemistry, band structure, surface engineering, morphology optimization, and ultimately device performance. Rather than treating these parameters independently, Fig. 2 emphasizes their strong interdependence in governing the structure–property–performance relationship of NW-based energy materials.

The fundamental electronic property of a semiconductor is its

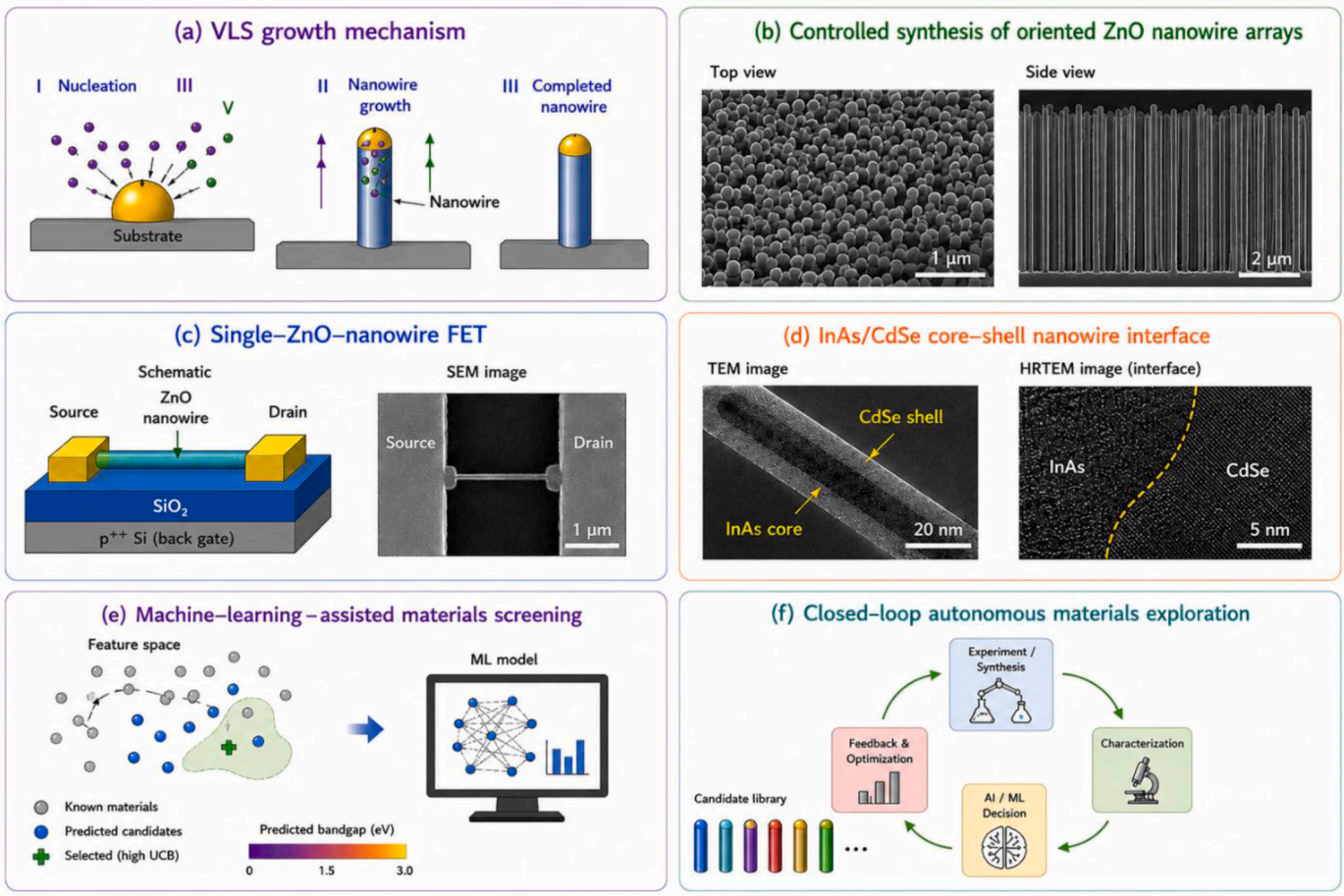


Fig. 1. Evolution of inorganic semiconductor nanowire engineering from controlled growth to autonomous materials discovery. (a) VLS growth mechanism; (b) controlled synthesis of oriented ZnO nanowire arrays; (c) single-ZnO-nanowire FET; (d) InAs/CdSe core–shell interface; (e) machine-learning-assisted materials screening; and (f) closed-loop autonomous materials exploration. Panels adapted from Refs. [Hijazi et al. [24]; Lin et al. [25]; Yoon et al. [26]; Kaladzhian et al. [27]; Ward et al. [28]; Kusne et al. [29], respectively, under the Creative Commons Attribution 4.0 International License (CC BY 4.0). Changes include cropping, resizing, relabeling, and integration into the present composite figure.

bandgap energy,

$$E_g = E_{CBM} - E_{VBM} \tag{1}$$

where E_{CBM} and E_{VBM} represent the conduction-band minimum and valence-band maximum, respectively. The magnitude and nature of E_g determine photon absorption, carrier excitation, optical emission, and electrochemical redox capability. However, in NWs, the effective bandgap may deviate from its bulk value because of quantum confinement, strain, crystal phase transitions, and surface electronic states [31,32].

The electronic properties of representative semiconductor NWs are summarized in Table 1. Group-IV materials, particularly Si and Ge, remain technologically important because of their compatibility with mature semiconductor manufacturing. Silicon possesses an indirect bandgap of 1.12 eV, electron mobility approaching 1450 $cm^2\ V^{-1}\ s^{-1}$, and excellent chemical stability, making it suitable for PVs, LIBs, and thermoelectric devices. Germanium exhibits an even higher electron mobility (2500–3900 $cm^2\ V^{-1}\ s^{-1}$), although its smaller bandgap (0.66 eV) increases thermal carrier generation and recombination losses [33,34].

In contrast, III–V semiconductor NWs such as GaAs and InP possess direct bandgaps of approximately 1.42 and 1.34 eV, respectively, enabling absorption coefficients exceeding $10^5 cm^{-1}$. Combined with electron mobilities frequently above 5000 $cm^2\ V^{-1}\ s^{-1}$ these materials are highly attractive for high-efficiency PVs and optoelectronic devices. Nevertheless, their widespread implementation remains limited by expensive epitaxial growth, arsenic toxicity, and severe surface Fermi-level pinning [34,35,73]. Wide-bandgap oxide NWs—including ZnO, TiO_2, WO_3, and Fe_2O_3—provide exceptional chemical stability and corrosion resistance but generally exhibit lower carrier mobilities and reduced visible-light absorption because of their large bandgaps (2.0–3.4 eV). Their performance is therefore enhanced through NW architectures that shorten minority-carrier transport distances while preserving efficient axial charge collection [35,73,74].

Carrier transport in semiconductors is fundamentally governed by the effective carrier mass,

$$m^* = \hbar^2 \left(\frac{d^2E}{dk^2} \right)^{-1} \tag{2}$$

which reflects the curvature of the electronic bands. A smaller effective mass generally produces higher carrier mobility; however, mobility is simultaneously influenced by phonon scattering, impurities, crystal defects, and surface scattering. Consequently, the electrical conductivity is expressed as

$$\sigma = q(n\mu_n + p\mu_p) \tag{3}$$

where n and p are the electron and hole concentrations, while the carrier mobility is given by

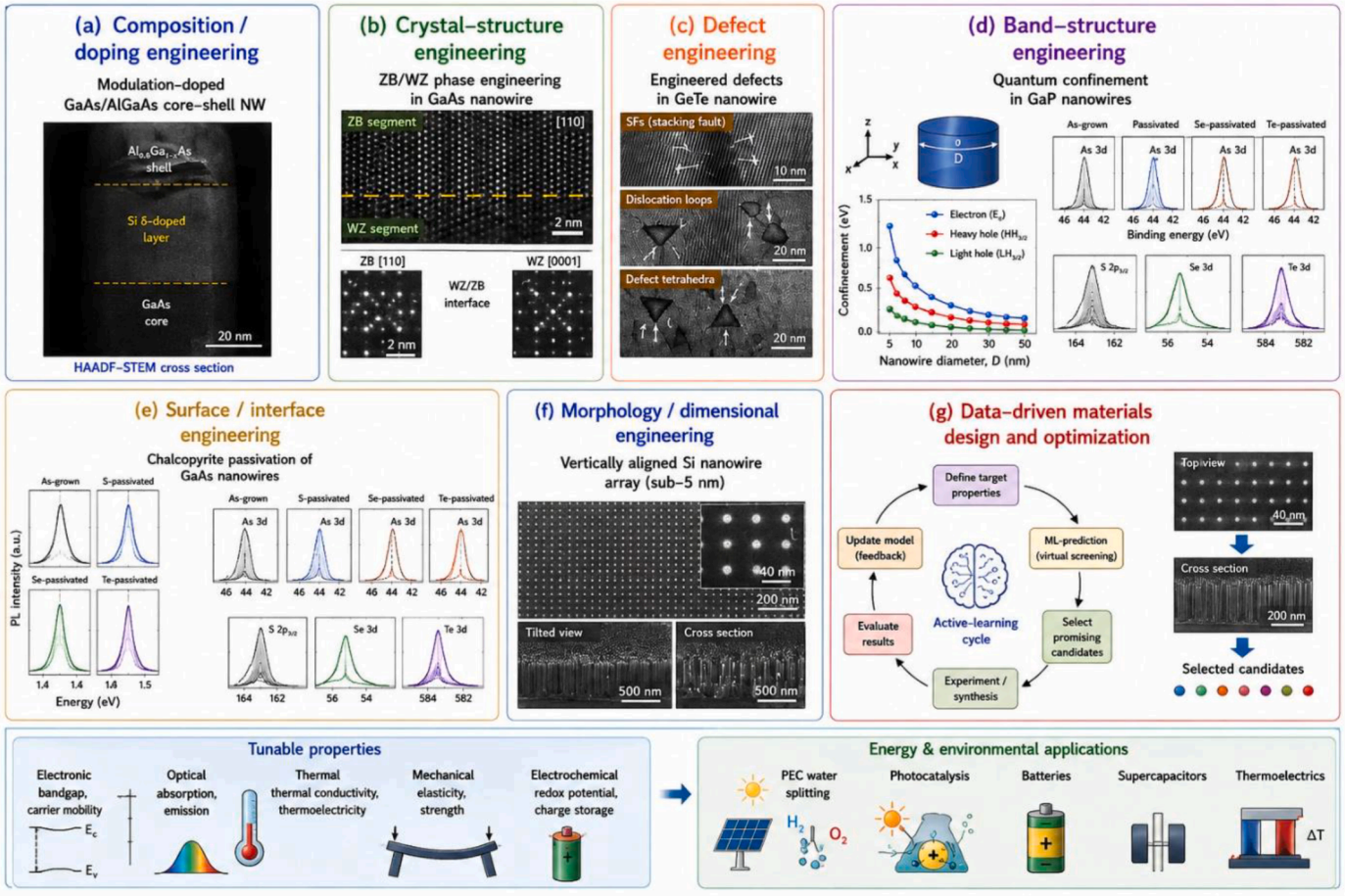


Fig. 2. Integrated materials-engineering pathways for controlling the structure–property–performance relationships of inorganic semiconductor NWs. Representative examples illustrate (a) composition and modulation-doping engineering in GaAs/AlGaAs core–shell NWs, (b) zinc blende/wurtzite crystal-phase engineering in GaAs NWs, (c) controlled defect engineering in GeTe NWs, (d) quantum-confinement-driven band-structure engineering in GaP NWs, (e) chalcogen-mediated surface engineering of GaAs NWs, (f) morphology and dimensional engineering of vertically aligned Si nanowire arrays, and (g) machine-learning-assisted materials design and active-learning optimization. Panels are adapted from Boland et al. [36], Liu et al. [37], Nukala et al. [38], Liao et al. [39], Yang et al. [40], Gao et al. [41], and Ma et al. [42], respectively, under the Creative Commons Attribution 4.0 International License (CC BY 4.0). Changes include cropping, resizing, relabeling, graphical harmonization, and integration into the present composite figure.

$$\mu = \frac{q\tau_s}{m^*}, \tag{4}$$

where τ_s denotes the momentum relaxation time. These relationships demonstrate that the exceptionally high intrinsic mobilities predicted from band-structure calculations are rarely achieved experimentally because scattering mechanisms become increasingly significant at nanoscale dimensions [73,74].

As NW diameters decrease below approximately 100 nm, surface phenomena increasingly dominate electronic behavior. The large fraction of surface atoms introduces dangling bonds, native oxides, and adsorption-induced trap states that strongly influence carrier transport and recombination. Consequently, electronic performance depends not only on intrinsic crystal quality but also on effective surface passivation. Chemical and dielectric passivation strategies have been shown to substantially reduce interface-state densities, suppress non-radiative recombination, enhance minority-carrier lifetimes, and improve optical emission in Si, Ge, GaAs, InP, and GaN NWs [75–77]. Similarly, epitaxial core–shell architectures simultaneously provide surface passivation, strain relaxation, carrier confinement, and improved interface quality, thereby enabling significant improvements in photovoltaic, photocatalytic, and PEC efficiencies [76,77].

Overall, Table 1 demonstrates that no single semiconductor simultaneously offers optimal optical absorption, carrier mobility, chemical stability, and manufacturability. Instead, high-performance NW systems emerge through coordinated engineering of composition, crystal structure, defects, and surfaces, as summarized in Fig. 2. This integrated design philosophy forms the foundation of modern NW materials engineering and provides the basis for the subsequent discussion of crystal structure engineering in Section 2.2.

2.2. *Crystal structure engineering*

Crystal structure engineering has emerged as one of the most powerful strategies for tailoring the electronic, optical, mechanical, and electrochemical properties of inorganic semiconductor NWs. Unlike bulk semiconductors, NWs frequently exhibit metastable crystal phases, crystallographic anisotropy, and coherent heterointerfaces that are inaccessible in equilibrium materials. Consequently, crystal chemistry not only governs atomic arrangement but also determines carrier transport, defect formation, phonon scattering, and interface stability, thereby exerting a profound influence on device performance [48,50,52,54,58].

Fig. 3 illustrates the crystal structure engineering framework adopted in this review, highlighting the relationships among crystal phase, growth orientation, polytypism, strain, lattice mismatch, and defect evolution. These structural descriptors collectively dictate the electronic band structure and ultimately the functional performance of semiconductor NWs.

Table 1
Representative properties, advantages, limitations, and green-energy applications of inorganic semiconductor NWs.

NW material	Class/ predominant crystal structure	Bandgap, Eg (eV, 300 K)	Carrier mobility (cm^2 V^{-1} s^{-1})	Thermal property	Key NW-specific advantages	Principal limitations	Representative green-energy applications	Refs.
Si	Group IV; diamond cubic	1.12 (indirect)	e^-: 1000–1450; h^+: 350–500	NW κ strongly size/defect dependent	Mature processing; tunable diameter; strong light trapping; radial junction formation; high theoretical Li-storage capacity	Surface-state recombination; native-surface effects; indirect absorption; lithiation-induced volume expansion	PVs; Li-ion batteries; thermoelectrics; photoelectrochemistry	[43–45]
Ge	Group IV; diamond cubic	0.66 (indirect)	e^-: 2500–3900; h^+: 1500–1900	NW κ strongly size/defect dependent	High carrier mobility; strong near-IR absorption; low-voltage carrier injection	Small bandgap; oxidation; thermal instability; high dark current	Infrared PVs; photodetectors; high-rate battery anodes	[46,47]
GaAs	III–V; zinc blende; wurtzite in thin NWs	1.42 (direct)	e^-: 4000–8500; h^+: 200–400	NW κ strongly size/defect dependent	High absorption coefficient; long minority-carrier diffusion length; efficient radial/ axial junctions	Surface Fermi-level pinning; As toxicity; costly epitaxy; surface recombination	High-efficiency PVs; PEC devices; optoelectronics	[48,49]
InP	III–V; zinc blende/wurtzite polytypes	1.34 (direct)	e^-: 3000–5400; h^+: 100–200	NW κ strongly size/defect dependent	Near-optimal single-junction bandgap; efficient light trapping; high absorption; radiation tolerance	Surface oxidation; contact resistance; expensive precursors and epitaxy	NW PVs; solar hydrogen; photodetectors	[50,51]
GaN	III–V nitride; wurtzite	3.40 (direct)	e^-: 200–1000; h^+: 5–30	NW κ strongly size/defect dependent	Wide bandgap; chemical stability; high breakdown field; polarization effects; UV absorption	Difficult p-type doping; high growth temperature; contact resistance	PEC water splitting; UV devices; power electronics; piezoelectric harvesting	[52,53]
ZnO	II–VI oxide; wurtzite	3.20–3.37 (direct)	e^-: 100–300; h^+: not reported	NW κ strongly size/defect dependent	Low-temperature growth; piezoelectricity; high exciton binding energy; dense vertical arrays	Unstable p-type doping; photocorrosion; native donor defects; surface-adsorption sensitivity	Piezoelectric nanogenerators; photocatalysis; sensors; photoanodes	[54–57]
TiO_2	Transition-metal oxide; anatase/ rutile	3.0–3.2 (phase dependent)	e^-: 0.1–10; h^+: very low	NW κ strongly size/defect dependent	Chemical durability; favorable band alignment; low toxicity; efficient axial electron transport	UV-limited absorption; low conductivity; electron trapping; slow interfacial kinetics	Photocatalysis; dye-sensitized solar cells; PEC water splitting; batteries	[58–60]
WO_3	Transition-metal oxide; monoclinic/ orthorhombic	2.6–2.8 (indirect)	e^-: 1–20; h^+: very low	NW κ strongly size/defect dependent	Visible-light absorption; strong oxidation potential; electrochromism; stable photoanode behavior	Conduction-band edge generally unsuitable for H_2 evolution; poor carrier mobility; recombination	PEC water oxidation; photocatalysis; electrochromic energy devices	[61,62]
α-Fe_2O_3	Transition-metal oxide; corundum	2.0–2.2 (indirect)	e^-: ~1; h^+: not reported	NW κ strongly size/defect dependent	Abundant; nontoxic; visible-light absorption; high theoretical photocurrent potential	Very short hole-diffusion length; poor conductivity; slow OER kinetics	PEC water oxidation; photocatalysis; photo-Fenton systems	[63,64]
CdS	II–VI chalcogenide; wurtzite/zinc blende	2.42 (direct)	e^-: 100–350; h^+: 10–50	NW κ strongly size/defect dependent	Visible-light absorption; favorable conduction band for H_2 evolution; facile heterojunction formation	Cd toxicity; severe photocorrosion; sulfur loss; limited long-term stability	Photocatalytic H_2; PEC cells; sensitized solar cells	[65–67]
CdSe	II–VI chalcogenide; wurtzite/zinc blende	1.70–1.75 (direct)	e^-: 450–900; h^+: 20–100	NW κ strongly size/defect dependent	Strong visible absorption; composition- and diameter-tunable optical response	Cd toxicity; oxidation; surface-trap sensitivity	PVs; photocatalysis; quantum-confined optoelectronics	[65–67]
SnO_2	Transition-metal oxide; rutile	3.6–3.7 (direct/ indirect debated)	e^-: 70–250; h^+: very low	NW κ strongly size/defect dependent	High conductivity when defect-doped; chemical stability; transparent-conducting behavior	Wide bandgap; oxygen-vacancy-induced trap states; poor visible absorption	Battery anodes; transparent electrodes; gas sensors; photocatalytic supports	[68,69]
CuO	p-type oxide; monoclinic	1.2–1.7 (indirect)	e^-: ~10; h^+: 1–100	NW κ strongly size/defect dependent	Intrinsic p-type behavior; visible-light absorption; low cost; catalytic activity	Low minority-carrier diffusion length; phase instability; recombination	Photocathodes; batteries; supercapacitors; photocatalysis	[70]
$BiVO_4$	Complex oxide; monoclinic scheelite	2.4–2.5 (indirect)	e^-: ~1; h^+: not reported	NW κ strongly size/defect dependent	Strong visible absorption; suitable valence-band position for oxygen evolution	Low electron mobility; short diffusion length; slow surface kinetics	PEC water oxidation; photocatalysis	[71,72]
SiC	Group IV compound; 3C/ 4H/6H polytypes	2.36–3.26 (indirect)	e^-: 400–1000; h^+: 80–120	NW κ strongly size/defect dependent	High thermal stability; high breakdown strength; corrosion resistance	Difficult low-temperature synthesis; polytype control; contact barriers	High-temperature electronics; photocatalysis; harsh-environment energy devices	[43–45]

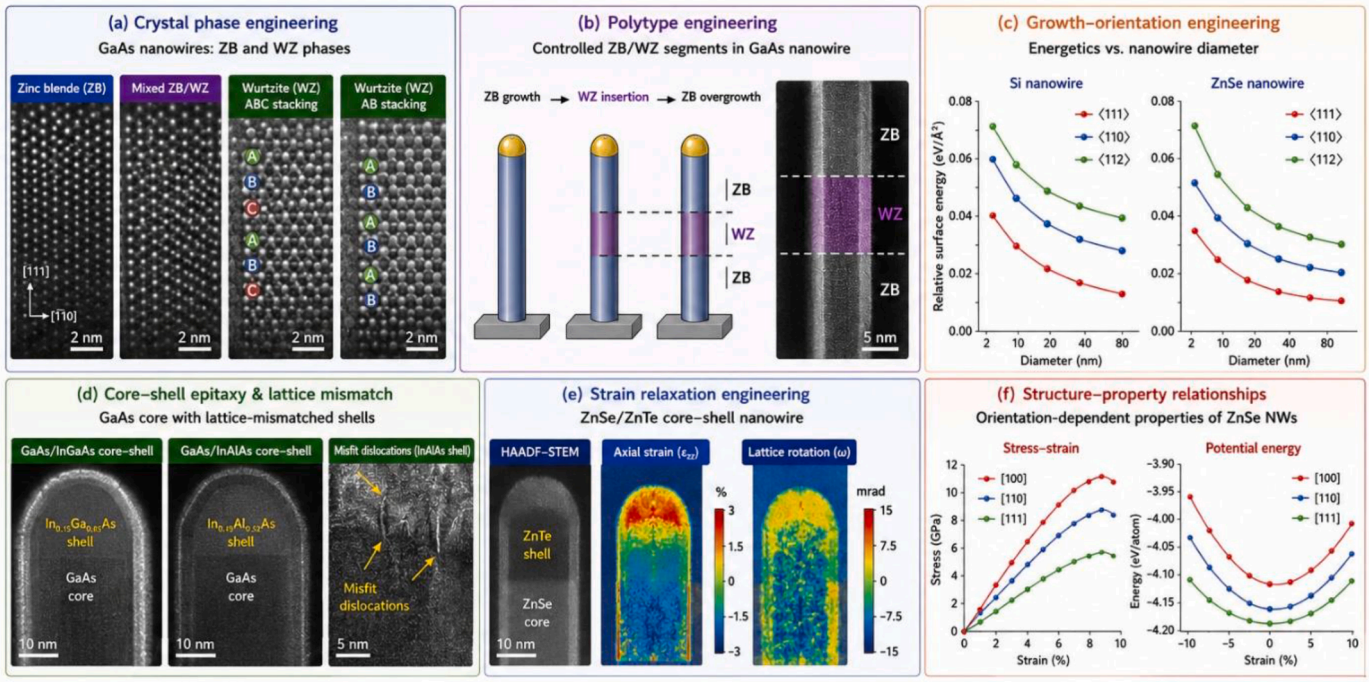


Fig. 3. Crystal-structure engineering strategies governing structure–property relationships in inorganic semiconductor NWs. Representative examples illustrate (a) zinc blende and wurtzite phase coexistence and atomic stacking in GaAs NWs; (b) controlled zinc blende/wurtzite polytype engineering in self-catalyzed GaAs NWs; (c) diameter-dependent crystallographic growth-orientation selection in semiconductor NWs; (d) coherent core–shell epitaxy and lattice-mismatch accommodation in GaAs-based heterostructure NWs; (e) atomic-scale strain relaxation and lattice rotation in ZnSe/ZnTe core–shell NWs; and (f) crystallographic-orientation-dependent mechanical response of zinc blende ZnSe NWs. Panels are adapted from Zeng and Olsson [78], Dursap et al. [79], Li et al. [80], Balaghi et al. [81], Martí-Sánchez et al. [82] and Islam et al. [83], respectively. Panels (a) and (c–f) are adapted under the Creative Commons Attribution 4.0 International License (CC BY 4.0); panel (b) is adapted under the Creative Commons Attribution 3.0 Unported License (CC BY 3.0). Changes include cropping, resizing, relabeling, graphical harmonization, and integration into the present composite figure.

Crystal quality is commonly evaluated using X-ray diffraction (XRD), where the diffraction condition obeys Bragg's law,

$$n\lambda = 2d_{hkl}\sin\theta \tag{5}$$

where n is the diffraction order, λ is the incident X-ray wavelength, d_{hkl} is the interplanar spacing, and θ is the Bragg angle. Analysis of diffraction patterns enables accurate determination of crystal phase, preferred orientation, lattice distortion, and structural defects, providing essential insight into NW crystallinity and epitaxial quality [50,54,58,84].

One of the defining structural characteristics of semiconductor NWs is polytypism, in which different stacking sequences coexist within the same chemical composition. While bulk III–V semiconductors such as GaAs, InP, and InAs generally crystallize in the zinc blende cubic structure, NWs frequently stabilize the metastable wurtzite hexagonal phase owing to their one-dimensional growth kinetics and reduced surface energy. Alternating zinc blende and wurtzite segments may even coexist along a single NW, producing axial crystal-phase heterostructures with atomically sharp interfaces. These phase transitions modify band alignment, spontaneous polarization, carrier confinement, and phonon dispersion, offering an additional degree of freedom for engineering optoelectronic and quantum devices without altering chemical composition [48,50–53,85,86].

Crystal-phase selection in III–V NWs is highly sensitive to the supersaturation and interfacial energetics established by the growth conditions [87,88]. In Au-catalyzed III–V NWs, Joyce et al. showed that lower growth temperature combined with a higher V/III ratio can stabilize phase-pure zinc blende, whereas higher temperature combined with a lower V/III ratio favors phase-pure wurtzite [87]. In self-assisted GaAs molecular-beam epitaxy, extended wurtzite segments have been obtained at a V/III flux ratio of approximately 4.0, with the Ga-droplet wetting angle maintained in an approximate 90–125° window [88]. Catalyst or droplet size also affects phase selection indirectly through curvature, contact angle, supersaturation, and the location/energy of nucleation at the triple-phase line [87,88]. These quantitative values should therefore be interpreted as process-specific benchmarks rather than universal thresholds: the V/III ratio reported for MBE is not directly transferable to MOVPE because precursor decomposition, surface kinetics, and catalyst composition differ [87,88].

Crystal engineering becomes even more important in heterostructured NWs, where lattice mismatch between adjacent materials introduces elastic strain. The lattice mismatch is defined as

$$f = \frac{a_{shell} - a_{core}}{a_{core}} \tag{6}$$

where a_{shell} and a_{core} are the lattice parameters of the core and shell materials. Small lattice mismatches permit coherent epitaxial growth, whereas larger mismatches promote the formation of misfit dislocations that degrade carrier transport and increase non-radiative recombination. Consequently, careful selection of lattice-compatible materials is essential for realizing high-quality core–shell NWs with minimal structural defects [48,51,57,67,71,72].

The thermodynamic stability of coherent interfaces is governed by the elastic strain energy density,

$$u_{strain} = \frac{1}{2}\sigma_{ij}\varepsilon_{ij} \tag{7}$$

which, under uniaxial loading, simplifies to

$$u_{strain} = \frac{1}{2}E_Y\varepsilon^2 \tag{8}$$

where E_Y is Young's modulus and ε is the elastic strain. As strain energy accumulates with increasing shell thickness or lattice mismatch, the

system eventually relaxes through dislocation formation or phase transformation. Therefore, optimizing shell thickness and interface coherence is critical for balancing strain relaxation with electronic performance [48,51,57,67,71,72].

Core–shell optimization therefore involves a deliberate trade-off. A coherent shell can passivate surface states, suppress non-radiative recombination, and confine carriers through favorable band offsets, but increasing shell thickness or lattice mismatch raises elastic strain energy and can ultimately generate misfit dislocations, roughening, or plastic relaxation [81]. Strain, however, is not necessarily a defect to be eliminated. In GaAs/$In_xGa_{1-x}As$ and GaAs/$In_xAl_{1-x}As$ core–shell NWs, lattice mismatch up to approximately 4% was accommodated coherently for suitable dimensions, producing tensile hydrostatic strain in the GaAs core approaching 7%. By varying shell composition and thickness, the GaAs bandgap was reduced continuously by as much as ~40% (~600 meV) [81]. This demonstrates intentional strain engineering: the design objective is to remain within a coherent or controllably relaxed regime in which passivation and carrier confinement are retained while strain is exploited to tune band edges, rather than simply minimizing lattice mismatch.

Beyond lattice matching, crystallographic growth orientation also strongly influences NW properties. Growth along ⟨111⟩, ⟨110⟩, or ⟨0001⟩ directions modifies atomic packing density, surface facet stability, and carrier transport anisotropy, thereby affecting electron mobility, thermal conductivity, and mechanical strength. For example, Si and Ge NWs grown along the ⟨111⟩ direction generally exhibit superior crystallinity and reduced surface defect density, whereas GaN and ZnO NWs preferentially grow along the polar *c*-axis (⟨0001⟩), enhancing piezoelectric and PEC performance [43–47,52–54,57].

From a materials engineering perspective, crystal structure should not be viewed as a static characteristic but rather as an actively tunable design variable that interacts with composition, defects, interfaces, and morphology. Modern synthesis techniques—including vapor–liquid–solid growth, molecular beam epitaxy, metal–organic chemical vapor deposition, and selective-area epitaxy—now enable atomic-scale control over crystal phase, stacking sequence, interface coherence, and strain distribution. Such advances have transformed crystal engineering into a central strategy for optimizing electronic structure and functional performance, providing the structural foundation for the band structure engineering discussed in the following section [48,50–53,57,71,72,85,86].

2.3. Band structure and quantum-confinement engineering

Band structure engineering represents a central principle of semiconductor NW design because it directly governs optical absorption, carrier generation, transport, recombination, and interfacial charge transfer [89]. While crystal structure engineering determines the atomic framework of a material, band engineering modifies the electronic-energy landscape through quantum confinement, alloy composition, elastic strain, heterojunction formation, surface chemistry, and electrostatic potential [90]. The reduced dimensionality and high surface-to-volume ratio of NWs permit manipulation of their electronic density of states beyond that achievable in bulk semiconductors, enabling improved photovoltaic, photocatalytic, PEC, thermoelectric, and electronic devices [89–91].

Fig. 4 presents the fundamental mechanisms of band structure engineering in semiconductor NWs, illustrating the interconnected roles of quantum confinement, strain, alloying, heterostructure formation, and electrostatic modulation in tailoring carrier transport and optoelectronic performance.

The electronic structure of a semiconductor is fundamentally described by the time-independent Schrödinger equation,

$$\widehat{H}\psi = E\psi \tag{9}$$

where the Hamiltonian operator is

$$\widehat{H} = -\frac{\hbar^2}{2m^*}\nabla^2 + V(\mathrm{r}) \tag{10}$$

with m^* representing the carrier effective mass and $V(\mathrm{r})$ the confinement potential. In NWs, the finite radial dimension imposes quantum confinement, producing discrete electronic sub-bands rather than the quasi-continuous energy spectrum characteristic of bulk materials. Consequently, the carrier effective mass, band dispersion, and density of states become diameter dependent, profoundly influencing optical absorption and carrier transport [89,90].

Quantum confinement becomes particularly significant when the NW diameter approaches or becomes smaller than the exciton Bohr radius. Within an effective-mass approximation, the confinement-induced bandgap shift may be expressed as

$$\Delta E_g \approx \frac{\hbar^2\beta_{01}^2}{2R^2}\left(\frac{1}{m_e^*}+\frac{1}{m_h^*}\right) - E_{\mathrm{Coul}}, \tag{11}$$

leading to

$$E_g(R) = E_{g,\mathrm{bulk}} + \Delta E_g \tag{12}$$

where R is the NW radius, β_{01} is the first zero of the relevant radial Bessel function, m_e^* and m_h^* are the electron and hole effective masses, respectively, and E_{Coul} represents the electron–hole Coulomb interaction. These relationships predict a systematic widening of the bandgap as the NW diameter decreases. First-principles calculations and experimental studies of silicon NWs have demonstrated pronounced diameter-dependent changes in bandgap, band dispersion, and carrier states under strong radial confinement [89,90]. Comparable confinement-related shifts are also observed in compound-semiconductor NWs, although their magnitude depends on effective mass, dielectric screening, surface termination, crystal phase, and growth direction [91,94].

For silicon NWs with diameters of only a few nanometers, the bandgap can increase substantially above the bulk value of approximately 1.12 eV [89,90]. Similar diameter-sensitive optical and electronic behavior is important in InP NW solar cells, where NW diameter affects optical resonances, absorption, carrier collection, and open-circuit voltage [51]. Although confinement can improve spectral tunability and increase the achievable photovoltage, excessive confinement may reduce carrier mobility and increase sensitivity to surface states because a larger fraction of the electronic wavefunction is localized near the NW surface [89,95].

The interpretation of bandgap shifts in ultrathin Si NWs remains more nuanced than a simple diameter-only quantum-confinement model [90,95,96]. First-principles calculations of well-passivated Si NWs support strong confinement-induced widening of the bandgap as diameter decreases [90]. However, surface termination and reconstruction can alter near-edge states by comparable energies: different terminating species can shift the calculated gap substantially at fixed diameter, and incomplete passivation can introduce surface-derived HOMO/LUMO states that reduce the gap or change its direct/indirect character [95,96]. Thus, quantum confinement and surface effects should not be treated as mutually exclusive mechanisms. In the ultrathin regime, the confined Si core establishes a strong size dependence, while surface bonding, reconstruction, oxidation, dielectric environment, and strain renormalize the observed electronic structure [90,95,96]. This coupling helps explain why reported diameter–bandgap relations vary across calculations and experiments and why surface chemistry must be specified when comparing nominally similar Si NWs [90,95,96].

The optical response of confined carriers is also influenced by the exciton binding energy,

$$E_B = \frac{\mu_r}{m_0}\frac{R_y}{\varepsilon_r^2}, \tag{13}$$

Where

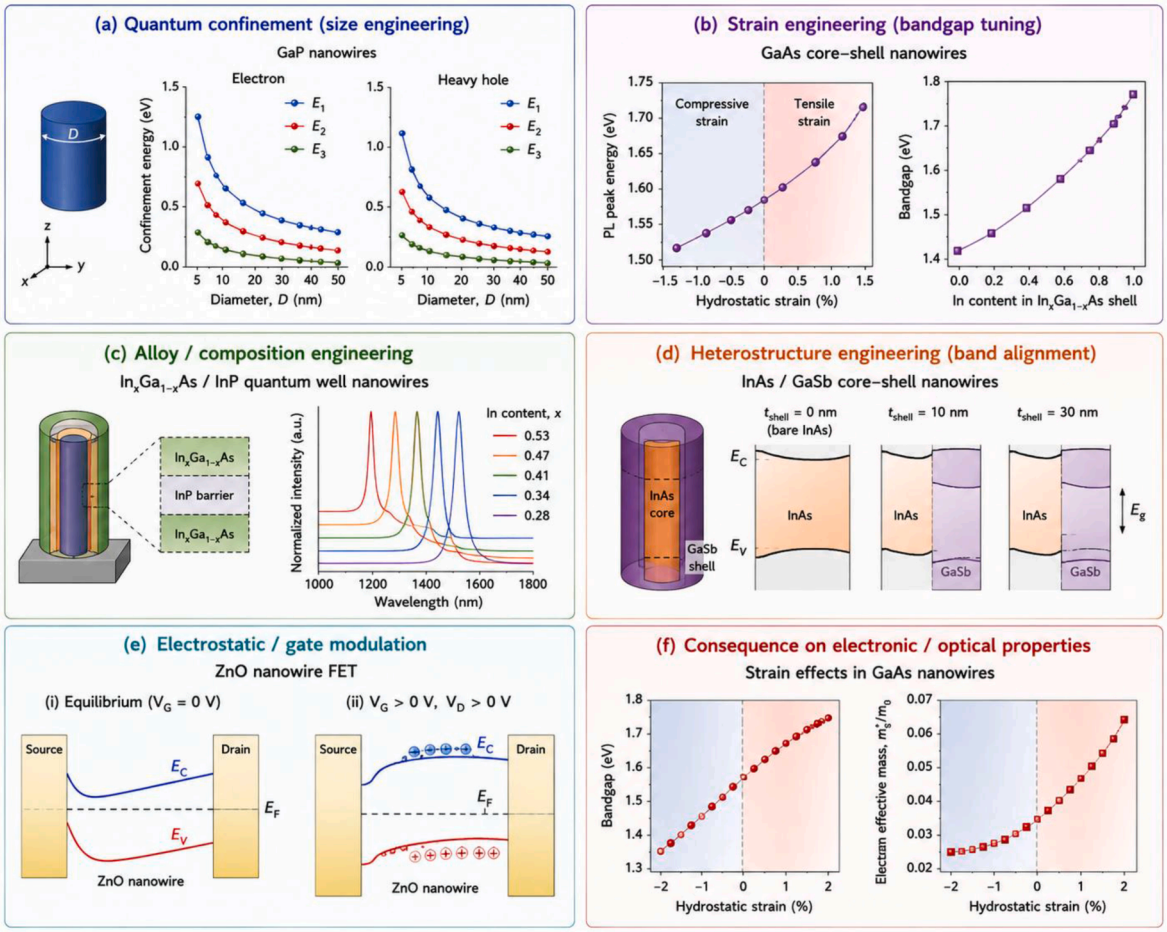


Fig. 4. Band-structure engineering mechanisms in inorganic semiconductor NWs. Representative examples show (a) size-dependent quantum confinement in GaP NWs, (b) strain-induced bandgap tuning in GaAs core–shell NWs, (c) composition-dependent optical tuning in InGaAs/InP quantum-well NWs, (d) heterostructure-induced band alignment and band inversion in InAs/GaSb core–shell NWs, (e) gate-controlled band modulation in a ZnO nanowire field-effect transistor, and (f) the resulting strain-dependent changes in GaAs bandgap and electron effective mass. Panels are adapted from Liao et al. [39], Balaghi et al. [81], Zhang et al. [92], Luo et al. [93], Yoon et al., and Balaghi et al. [26], respectively, under the Creative Commons Attribution 4.0 International License (CC BY 4.0). Changes include cropping, resizing, relabeling, and integration into the present composite figure.

$$\mu_r = \frac{m_e^* m_h^*}{m_e^* + m_h^*} \tag{14}$$

is the reduced effective mass, m_0 is the free-electron mass, R_y is the Rydberg energy, and ε_r is the relative dielectric constant. Reduced dielectric screening and enhanced electron–hole overlap in nanoscale systems may increase exciton binding energy relative to the corresponding bulk material. These effects influence optical-transition energies, exciton dissociation, carrier separation, radiative recombination, and photocatalytic efficiency [89,91].

Beyond dimensional confinement, alloy engineering provides a powerful route for continuously tuning NW electronic properties. For a binary alloy formed from compounds A and B, the composition-dependent bandgap may be approximated by

$$E_g(x) = xE_g^A + (1-x)E_g^B - bx(1-x), \tag{15}$$

where b is the bandgap-bowing parameter. The lattice parameter may simultaneously be estimated using Vegard's law,

$$a(x) = xa_A + (1-x)a_B \tag{16}$$

Alloy NWs therefore provide coupled control over bandgap, lattice compatibility, strain, and carrier confinement. For example, theoretical analysis of SiGe NWs shows that both composition and diameter strongly modify their band structure and electronic properties [97]. Composition grading in ZnCdSe/ZnO core–shell NW arrays has similarly been used to tune interfacial energetics and promote directional carrier transfer for PEC hydrogen generation [98].

Mechanical strain provides another effective mechanism for modifying electronic bands without changing chemical composition. To first order, hydrostatic strain shifts the conduction- and valence-band edges according to

$$\Delta E_C = a_c \mathrm{Tr}\,(\varepsilon) \tag{17}$$

$$\Delta E_V = a_v \mathrm{Tr}\,(\varepsilon) + \Delta E_{\mathrm{shear}} \tag{18}$$

where a_c and a_v are the conduction- and valence-band deformation potentials, respectively. The direction and magnitude of the resulting bandgap shift depend on the material, crystal orientation, strain tensor, and electronic-band symmetry. In core–shell NWs, elastic strain can be sustained over larger lattice mismatches than in planar heterostructures because free sidewalls facilitate partial elastic relaxation. This characteristic has enabled wide bandgap tuning in highly mismatched GaAs-based core–shell NWs [81]. Atomic-resolution investigations have also shown that nanoscale strain variations can produce spatially localized changes in band structure across core–shell NW heterostructures [82].

Band engineering in practical devices rarely relies on a single mechanism. Modern NW architectures instead combine dimensional confinement, alloying, crystal-phase control, strain, doping, and radial

or axial heterojunctions to establish favorable band offsets and carrier-transport pathways. Type-I heterojunctions confine electrons and holes within the same constituent and are therefore attractive for radiative-recombination and light-emission applications. By contrast, Type-II heterojunctions spatially separate photogenerated electrons and holes, suppressing recombination and facilitating directional charge transfer in photovoltaic and PEC systems.

The effectiveness of Type-II band alignment has been demonstrated in $TiO_2/BiVO_4$ NW heterostructure photoanodes, in which $BiVO_4$ functions as the visible-light absorber and TiO_2 provides an electron-transport pathway [72]. Similarly, $WO_3/BiVO_4$ core–shell NWs combine strong visible-light absorption with improved charge separation and carrier collection during PEC water oxidation [71]. Sequential CdSe/CdS NW architectures also exploit staggered band alignment to improve charge separation and solar-cell performance [67]. These examples demonstrate that band alignment must be designed together with NW geometry, interface quality, optical absorption depth, and carrier-diffusion length.

Despite these advances, band structure engineering remains constrained by several practical limitations. Strong confinement increases sensitivity to surface reconstruction, oxidation, adsorbates, and trap states, making device performance dependent on effective surface passivation [89,95]. Alloy fluctuations can generate local bandgap inhomogeneity and carrier localization, while excessive lattice mismatch may eventually produce misfit dislocations and non-radiative recombination centers [81,82]. Moreover, simplified effective-mass treatments frequently neglect atomistic surface structure, crystal-phase mixing, dielectric confinement, many-body interactions, and defect-induced band-tail states. These omissions can lead to substantial differences between predicted and experimentally measured electronic properties [89,90,97].

Consequently, band structure engineering is increasingly moving toward integrated computational–experimental strategies combining DFT, atomistic electronic-structure calculations, strain mapping, advanced spectroscopy, and data-driven modeling. Such approaches can establish quantitative relationships among NW diameter, composition, strain, interface structure, band alignment, and carrier dynamics before extensive experimental synthesis [81,82,97]. Predictive optimization of these coupled variables will accelerate the discovery of NWs with tailored electronic and optical properties. Nevertheless, electronic performance cannot be fully optimized through band engineering alone because defect chemistry strongly governs carrier trapping, recombination, ion transport, and long-term stability. This motivates the following discussion of defect engineering, in which atomic-scale imperfections are treated as controllable functional variables rather than exclusively as undesirable structural defects.

2.4. Defect engineering

Defect engineering is a cornerstone of semiconductor NW design because atomic-scale imperfections can either degrade or enhance functional performance depending on their nature, concentration, distribution, and electronic character. Unlike bulk semiconductors, NWs possess an exceptionally large surface-to-volume ratio and abundant interfaces, making defect formation energetically favorable while simultaneously providing opportunities for deliberate manipulation of electronic, optical, catalytic, and electrochemical properties [58,60,68,69]. Crystal defects are generally classified as point defects (vacancies, interstitials, antisites, and substitutional impurities), line defects (dislocations), and planar defects (stacking faults, twin boundaries, and grain boundaries), each influencing carrier transport, recombination, and structural stability through distinct physical mechanisms [48,50,52,53].

The thermodynamic stability of a defect is quantified by its formation energy,

$$E_f(D^q) = E_{\text{defect}} - E_{\text{perfect}} - \sum_i n_i \mu_i + qE_F \tag{19}$$

where E_{defect} and E_{perfect} are the total energies of the defective and pristine crystals, respectively, n_i and μ_i represent the number and chemical potential of exchanged atomic species, q is the defect charge state, and E_F is the Fermi level. Defects with lower formation energies are more readily incorporated during synthesis and therefore exert a stronger influence on the electronic structure and transport behavior [48,50].

Among point defects, oxygen vacancies can act as shallow donors, alter adsorption energetics, and increase carrier density, but the same defects can become deep trapping or recombination centers when their concentration, charge state, or spatial distribution is unfavorable [99–101]. A quantitative example is nanostructured WO_3, for which an intermediate bulk oxygen-vacancy population of approximately 2% of oxygen sites produced the highest photoinduced carrier density and slowest recombination, whereas lower (~0.5%) and higher (~5.8%) vacancy populations gave poorer photoelectrochemical response [99]. This non-monotonic behavior illustrates why "more vacancies" is not a general optimization rule.

For TiO_2 and ZnO, a single transferable optimum atomic-percent range is not established because reported vacancy populations depend strongly on synthesis route, surface/bulk location, charge state, and measurement method [100,101]. XPS estimates near-surface reduced-cation/oxygen components; EPR detects paramagnetic vacancy-related centers; positron-annihilation methods probe vacancy-type defects; and optical/electrical measurements infer electronically active trap or donor populations [101,102]. In ZnO photoanodes, controlled electrochemical vacancy generation demonstrates an optimum balance among reactive sites, charge separation, and interfacial charge transfer, whereas excessive or improperly located defects can enhance recombination [100]. TiO_2 studies similarly report beneficial donor-like/surface vacancies under some conditions and detrimental bulk trap-mediated recombination under others [101,102]. Accordingly, vacancy optimization should be defined by a material- and process-specific response curve that combines quantitative defect characterization with carrier lifetime, conductivity, photocurrent/quantum efficiency, and stability, rather than by a universal vacancy percentage [99–102].

Modern defect engineering increasingly combines DFT, high-resolution transmission electron microscopy (HRTEM), electron paramagnetic resonance (EPR), positron annihilation spectroscopy (PAS), and operando electron microscopy to identify defect configurations and establish quantitative relationships between atomic-scale imperfections and macroscopic performance [48,50,63,69]. Rather than being regarded solely as structural imperfections, defects are now recognized as tunable design variables that regulate carrier concentration, band alignment, catalytic activity, ionic transport, and electrochemical kinetics, thereby providing a critical bridge between crystal engineering and the controlled doping strategies discussed in the following section [54,58,60,68,69].

2.5. Doping engineering

Doping engineering is one of the most effective approaches for tailoring the electrical conductivity, carrier concentration, Fermi-level position, and band alignment of semiconductor NWs through the intentional incorporation of impurity atoms into the crystal lattice [45–47,51]. Depending on the dopant species, NWs can exhibit n-type conductivity through donor dopants (e.g., phosphorus in Si or Sn in ZnO) or p-type conductivity through acceptor dopants (e.g., boron in Si or Mg in GaN), enabling precise control of charge transport for electronic, optoelectronic, and energy-conversion devices [45,51,84,103]. Beyond conventional uniform doping, semiconductor NWs support

advanced architectures including axial doping, radial doping, modulation doping, and core–shell doping, which spatially tailor carrier distributions while minimizing ionized-impurity scattering. These strategies facilitate the fabrication of nanoscale p–n junctions, tunnel junctions, and high-mobility transport channels within individual NWs [46,51,84,103].

The equilibrium electron concentration is governed by

$$n = N_C \exp\left(-\frac{E_C - E_F}{k_B T}\right) \tag{20}$$

where N_C is the effective density of states in the conduction band, E_C is the conduction-band minimum, E_F is the Fermi level, k_B is Boltzmann's constant, and T is the absolute temperature. Increasing donor or acceptor concentrations shifts the Fermi level toward the conduction or valence band, respectively, thereby enhancing electrical conductivity and modifying carrier transport characteristics [45,51].

The effectiveness of doping is ultimately determined by dopant activation, which depends on dopant solubility, lattice incorporation, self-compensation, and defect interactions. In nanoscale semiconductors, incomplete dopant activation, surface segregation, and defect compensation frequently reduce the free-carrier concentration despite substantial dopant incorporation [45,46,84]. Consequently, optimization of dopant concentration, spatial distribution, activation efficiency, and interface quality remains essential for achieving high-performance NW devices with improved conductivity, carrier mobility, junction quality, and long-term operational stability [46,51,84,103].

2.6. Surface and interface chemistry

Surface and interface chemistry plays a decisive role in determining the functional performance of semiconductor NWs because their exceptionally large surface-to-volume ratios make electronic, optical, and electrochemical processes highly sensitive to surface states. During synthesis and post-processing, NW surfaces frequently contain dangling bonds, native oxides, catalyst residues, adsorbed species, and surface reconstruction, all of which modify the local electronic structure and influence carrier transport. These surface imperfections introduce localized electronic states within the bandgap, resulting in Fermi-level pinning, surface band bending, carrier trapping, and enhanced nonradiative recombination, thereby limiting photovoltaic efficiency, PEC activity, photodetector performance, and long-term device stability [104–107]. Recent experimental and theoretical studies further demonstrate that surface scattering remains one of the dominant factors limiting carrier mobility in one-dimensional semiconductor NWs.

The influence of surface states is commonly quantified by the surface recombination velocity,

$$R_s = S(n - n_0) \tag{21}$$

where R_s is the surface recombination rate, S is the surface recombination velocity, n is the excess carrier concentration, and n_0 is the equilibrium carrier concentration. A large value of S indicates rapid carrier recombination at the surface, leading to reduced carrier lifetime, shorter diffusion lengths, and lower charge-collection efficiency.

Effective surface passivation is therefore essential for maximizing NW performance. Dielectric coatings deposited by atomic layer deposition (ALD), including Al_2O_3, HfO_2, SiO_2, and ZnO, together with sulfur treatments and molecular self-assembled monolayers, substantially suppress dangling bonds and interface trap states while improving carrier lifetime, open-circuit voltage, responsivity, and photoconversion efficiency [71,72,105]. Recent work has shown that ultrathin ALD-grown ZnO passivation layers on GaAs NWs increase photoluminescence intensity by nearly an order of magnitude while dramatically improving detector responsivity and specific detectivity.

Beyond passivation, interface engineering through epitaxial core–shell heterostructures, band-aligned junctions, and catalyst-functionalized surfaces enables precise regulation of band alignment, interfacial electric fields, and directional charge-transfer pathways. Cocatalysts such as Pt, Ni, CoO_x, and MoS_2 further accelerate interfacial redox reactions while suppressing electron–hole recombination in photocatalytic and PEC systems [51,58,71,72]. Consequently, surface and interface chemistry has evolved from a strategy for mitigating surface defects into a comprehensive engineering approach for controlling electronic structure, catalytic activity, charge-transfer kinetics, and long-term operational stability, thereby establishing the mechanistic foundation for morphology engineering discussed in the following section.

2.7. Morphology engineering

Morphology engineering provides one of the most effective approaches for optimizing the performance of inorganic semiconductor NWs through deliberate control of diameter, aspect ratio, tapering, branching, hierarchical architecture, surface roughness, and array density. Because NWs possess strong quantum confinement and exceptionally high surface-to-volume ratios, their geometric characteristics directly influence optical absorption, carrier transport, catalytic activity, and electrochemical performance [51,107,108].

The influence of NW geometry is commonly described by the surface-to-volume ratio,

$$\frac{S}{V} = \frac{4}{D} \tag{22}$$

where D is the NW diameter. This relationship illustrates that decreasing the diameter substantially increases the fraction of surface atoms, thereby enhancing adsorption, catalytic activity, and interfacial reaction kinetics. However, extremely small diameters also increase carrier scattering, surface recombination, and sensitivity to surface defects, necessitating careful optimization of NW dimensions [104,107,108].

Morphology also governs light management and charge transport. Subwavelength NWs support resonant optical modes, multiple scattering pathways, and enhanced light trapping, thereby increasing photon absorption while shortening carrier diffusion distances in photovoltaic and PEC devices [51,109]. High-aspect-ratio NWs simultaneously provide continuous one-dimensional pathways for electron transport with fewer grain boundaries than polycrystalline thin films, whereas excessive tapering or uncontrolled surface roughness introduces structural inhomogeneity that degrades electrical conductivity and mechanical reliability [75,107,109].

Hierarchical and branched NW architectures have recently emerged as particularly attractive because they combine large electrochemically active surface areas with interconnected transport networks. These three-dimensional structures improve electrolyte accessibility, facilitate rapid ion diffusion, accommodate volumetric expansion during electrochemical cycling, and provide abundant catalytic active sites for batteries, supercapacitors, photocatalysis, and hydrogen evolution [58,108,110]. Furthermore, recent advances in orientation-controlled and non-⟨111⟩ NW growth demonstrate that morphology, crystallographic orientation, and interface structure are intrinsically coupled design parameters that collectively determine device performance.

The principal materials-engineering strategies discussed throughout this section, together with their mechanisms, advantages, limitations, representative applications, and supporting literature, are summarized in Table 2.

Across these engineering strategies, the most transferable design variables are not the material names themselves but the competing characteristic length and energy scales [90,99,171,172]. These include NW radius relative to carrier- or exciton-diffusion length, defect-state depth relative to the band edges, band offsets relative to thermal energy, shell thickness relative to the coherent-strain limit, and

Table 2
Comparative assessment of advanced engineering strategies for inorganic semiconductor NWs.

Engineering strategy	Control variable/dominant mechanism	Typical implementation routes	Representative NW systems	Most relevant performance gains	Principal limitations/risks	Refs.
Composition engineering	Elemental identity and stoichiometry; modifies orbital hybridization, bonding, carrier concentration, and phase stability	Binary-to-ternary alloying; cation/anion substitution; quaternary compositions; nonstoichiometric growth	SiGe; InGaAs; AlGaN; additional systems require source verification	Bandgap tuning; expanded absorption; conductivity optimization; catalytic selectivity	Phase segregation; composition gradients; precursor incompatibility; miscibility gaps; stoichiometric control	[111–113]
Crystal-phase engineering	Crystal structure, polytype, and growth orientation; changes symmetry, orbital overlap, polarization, phonon dispersion, and band alignment	Catalyst-size and growth-temperature control; precursor-ratio control; substrate orientation; epitaxial strain	ZB/WZ GaAs; InP; GaN; ZnO; TiO_2 phase engineering	Improved optical emission; carrier transport; polarization-driven charge separation	Polytype mixing; stacking faults; metastability; nonuniform phase distribution	[114–117]
Diameter/quantum-confinement engineering	NW diameter; modifies carrier wavefunctions, density of states, exciton binding, and phonon scattering	Catalyst-size control; template confinement; selective-area growth; etching	Si; Ge; CdSe; ZnO; GaAs; InP	Bandgap/absorption control; photoluminescence tuning; thermoelectric enhancement	Surface recombination; quantum trapping; reduced robustness; fabrication variability	[51, 118–120]
Alloy bandgap engineering	Alloy fraction; continuously modulates electronic band structure through chemical substitution	Vapor-phase alloying; co-evaporation; mixed precursors; sequential precursor modulation	Representative systems in source table are text-corrupted and require verification	Optimized solar absorption; wavelength-selective emission; tandem integration	Alloy disorder; bowing uncertainty; segregation; nonradiative recombination	[97, 121–123]
Strain engineering	Elastic strain and lattice mismatch; alters band edges, effective masses, polarization, phonons, and defect energetics	Core-shell growth; epitaxial mismatch; substrate bending; thermal-expansion mismatch	Si/Ge; GaAs/InGaAs; ZnO heterostructures; III-nitrides	Improved carrier separation; band alignment; mobility; catalytic activity	Strain relaxation; dislocation formation; fracture; thermal instability	[81,82, 124,125]
Defect engineering	Vacancy, interstitial, antisite, dislocation, stacking-fault, and twin-boundary populations; introduces electronic states, scattering centers, catalytic sites, and diffusion pathways	Growth-atmosphere control; annealing; plasma treatment; irradiation; chemical reduction/oxidation	ZnO; hematite; other oxygen-deficient systems require source verification	Higher catalytic activity; pseudocapacitance; dopant activation; visible-light response	Deep traps; recombination; structural instability; uncontrolled defect clustering	[63, 126–128]
Doping engineering	Dopant species, concentration, distribution, and activation; shifts Fermi level and controls carrier density, conductivity, band bending, and junction behavior	In situ doping; ion implantation; diffusion; modulation doping; co-doping	B/P-doped Si; Si-doped GaAs; Mg-doped GaN; Al-doped ZnO	Higher conductivity; built-in fields; reduced contact resistance; optimized carrier extraction	Compensation; segregation; incomplete activation; surface depletion; lattice damage	[64, 129–131]
Gradient doping	Axial/radial dopant profile; creates internal electric fields and spatially controlled carrier transport	Time-dependent precursor flow; sequential epitaxy; shell doping	Si; GaAs; InP; ZnO radial and axial junctions	Reduced recombination; improved collection efficiency; tailored junction response	Profile quantification; dopant diffusion; abruptness control	[132–134]
Co-doping	Two or more complementary dopants; modifies defect compensation, solubility, and band-edge states	Simultaneous/sequential precursor addition; post-growth diffusion	Li/N-doped ZnO; compensated III–V NWs; one source-table system requires verification	Enhanced conductivity; visible-light photocatalysis; stabilized p-type behavior	Complex defect interactions; unpredictable compensation; reproducibility	[135–137]
Surface passivation	Surface-state density and chemistry; saturates dangling bonds and suppresses nonradiative surface recombination	Oxide shells; sulfide treatment; hydrogenation; ALD; organic ligands	Sulfide-passivated III–V NWs; oxide-shell examples require source verification	Reduced recombination; increased carrier lifetime; improved device efficiency and stability	Thermal instability; barrier formation; incomplete coverage; added processing complexity	[32,34,73, 74]
Surface functionalization	Surface ligands, catalytic species, and molecular dipoles; alters surface energy, wetting, charge transfer, adsorption, and selectivity	Ligand exchange; molecular grafting; plasma treatment; catalyst decoration	ZnO; GaN; InP; Si NWs; one source-table system requires verification	Improved catalytic selectivity; charge transfer; chemical affinity	Ligand desorption; contamination; poor stability; blocked active sites	[68,138, 139]
Catalyst decoration	Catalyst composition, size, loading, and interface contact; lowers reaction barriers and accelerates interfacial charge transfer	Electrodeposition; photodeposition; ALD; sputtering; nanoparticle attachment	Pt/Si; other source-table catalyst/NW pairs require verification	Lower overpotential; higher current density; improved selectivity and catalytic kinetics	Noble-metal cost; agglomeration; detachment; parasitic shading	[18,66, 140]
Core-shell engineering	Radial composition and shell thickness; combines passivation, confinement, strain distribution, and radial band alignment	Sequential epitaxy; ALD; solution coating	GaAs/AlGaAs; InP/InGaP; additional source-table pairs require verification	Higher carrier lifetime; photovoltaic efficiency; chemical durability	Interface defects; lattice mismatch; shell nonuniformity; radial strain	[71,77, 141,142]
Axial heterostructure engineering	Composition and axial band alignment; forms quantum wells, barriers, and axial junctions	Precursor switching during growth; selective-area epitaxy	InP/InAs; GaAs/GaP; Si/Ge	Spatial carrier separation; multijunction and multifunction device integration	Interface abruptness; dopant memory; axial diffusion; contact complexity	[143–146]
Radial heterostructure engineering	Core-shell radial band profile; decouples optical absorption from carrier-collection direction	Shell epitaxy; ALD; conformal deposition	Si radial p–n; GaAs/AlGaAs; InP shells	Enhanced photovoltaic and PEC collection; short radial collection paths	Shell coverage; junction uniformity; surface depletion	[57,147, 148]
Morphology engineering	Length, tapering, branching, roughness, porosity, and alignment; controls optical resonances, transport access, diffusion, stress accommodation, and active area	Template growth; hydrothermal synthesis; selective-area epitaxy; etching; hierarchical growth	Branched ZnO; porous Si; additional hierarchical arrays require source verification	Higher photocurrent; capacity; capacitance; catalytic activity	Nonuniformity; fragility; transport bottlenecks; difficult scale-up	[149–152]

(*continued on next page*)

Table 2 (*continued*)

Engineering strategy	Control variable/dominant mechanism	Typical implementation routes	Representative NW systems	Most relevant performance gains	Principal limitations/risks	Refs.
Porosity engineering	Pore size, density, and connectivity; increases accessible area, shortens diffusion pathways, and reduces thermal conductivity	Dealloying; etching; templating; thermal oxidation/reduction	Porous Si; additional source-table systems require verification	Higher capacity; faster kinetics; lower thermal conductivity	Reduced mechanical strength; side reactions; difficult pore-size control	[152–155]
Array-density/orientation engineering	NW pitch, tilt, fill fraction, and alignment; alters collective optics, diffusion, capillary transport, and current collection	Patterned catalysts; nanoimprint lithography; selective-area growth	Si; InP; GaAs; ZnO arrays; one source-table system requires verification	Improved light trapping; current density; substrate-scale performance	Shadowing; crowding; nonuniform precursor access; coalescence	[48,156, 157]
Thermal engineering	Phonon mean free path, roughness, defects, and interface density; enhances phonon scattering while seeking to preserve electrical transport	Diameter reduction; roughening; alloying; superlattices	Rough Si NWs; SiGe; one source-table system requires verification	Reduced thermal conductivity; improved thermoelectric response and waste-heat conversion	Carrier-mobility penalty; contact resistance; mechanical instability	[158–161]
Electrostatic/field engineering	External bias, gate field, polarization, and surface charge; modulates depletion, accumulation, band bending, and carrier separation	Gate electrodes; ferroelectric coupling; electrolyte gating; polarized heterostructures	ZnO; GaN; Si; InP NW devices	Improved photocurrent; carrier extraction; sensing; switching	Screening; dielectric breakdown; hysteresis; device complexity	[162–164]
Multiscale computational engineering	Atomic-, mesoscale-, and device-level design variables; predicts stability, transport, interfaces, growth, and performance before synthesis	DFT; MD; phase-field; FEA; CFD; ML; high-throughput simulation; surrogate models; inverse design	Cross-cutting across material classes	Faster discovery; optimized synthesis windows; reduced experimental search space and development cost	Model error; idealized structures; dataset scarcity; limited transferability	[163, 165–167]
Sustainable process engineering	Energy demand, precursor toxicity, material criticality, and recyclability; reduces life-cycle environmental and economic burden	Low-temperature growth; aqueous processing; catalyst recovery; precursor substitution	ZnO; Si; abundant oxides and sulfides; one source-table system requires verification	Lower cost; reduced emissions; safer manufacturing; improved circularity and scalability	Performance tradeoffs; purity constraints; limited green precursor options	[168–170]

ion-diffusion distance relative to electrode radius. These variables rarely improve performance monotonically. Decreasing diameter, for example, can strengthen optical confinement and increase active surface area while simultaneously increasing surface recombination and chemical instability [171]; increasing defect density can enhance conductivity or catalytic-site density until deep trapping and structural degradation dominate [99]. Materials-by-design must therefore be understood as constrained multi-objective optimization rather than maximization of an isolated nanoscale property [99,172].

2.8. Computationally enabled nanowire materials design: capability and validation limits

Computational methods become most valuable for NW engineering when they resolve experimentally testable mechanisms rather than operate as an independent layer of prediction [171,172]. Density functional theory (DFT), for example, can quantify facet-dependent surface energies, adsorption energies, defect formation energies, band offsets, and strain-dependent electronic structure, thereby helping explain why changes in surface termination, vacancy population, crystal phase, or heterointerface chemistry alter measured carrier transport and catalytic activity [171,172]. Atomistic simulations can extend this description to temperature-dependent reconstruction, diffusion, nucleation, and mechanically driven interface evolution, whereas continuum and device-scale models connect these nanoscale descriptors to optical absorption, carrier collection, thermal transport, and electrochemical response [172].

Nevertheless, the predictive hierarchy introduces systematic scale-transfer errors [171,172]. DFT calculations commonly employ idealized facets, periodic cells, selected defect charge states, and controlled surface termination, whereas experimentally synthesized NWs may simultaneously contain native oxides, adsorbates, reconstruction, stacking faults, dopant segregation, strain gradients, catalyst residues, and spatially heterogeneous interfaces [171,172]. Likewise, molecular simulations are constrained by accessible length and time scales, while continuum models require effective parameters that may themselves vary with NW diameter, defect density, surface chemistry, and operating environment. Agreement between a calculated property and an experimental trend should therefore not be interpreted automatically as validation of the assumed microscopic mechanism.

Data-driven approaches introduce a complementary but different limitation. Machine-learning models can identify nonlinear synthesis–structure–property relationships and prioritize candidate experiments, but their reliability is bounded by dataset size, reporting bias, inconsistent metadata, laboratory-to-laboratory domain shift, and the scarcity of failed synthesis experiments [173–175]. Consequently, computation should function within an iterative prediction–synthesis–characterization–validation loop [174,175]. Predictions of defect energetics, band alignment, surface reactivity, morphology, or device response should be confronted with quantitative microscopy, spectroscopy, electrical measurements, and operando characterization before being propagated into higher-level optimization or digital-twin models [174,175].

3. Advanced characterization techniques for inorganic semiconductor NWs

Advanced characterization is indispensable for understanding the structure–property–performance relationships of inorganic semiconductor NWs. Owing to their nanoscale dimensions and complex hierarchical architectures, NWs exhibit structural, chemical, and electronic characteristics that cannot be fully resolved using a single characterization technique. Instead, comprehensive evaluation requires the integration of complementary analytical methods capable of probing materials across multiple length and time scales, ranging from atomic bonding and crystallographic defects to mesoscale interfaces

and device-level functionality. Such multiscale characterization provides the experimental foundation for validating synthesis strategies, optimizing interface engineering, and establishing quantitative correlations between nanostructure and functional performance [143,176–178].

The characterization of semiconductor NWs extends far beyond simple morphological observation to encompass investigations of crystal structure, elemental composition, defect distribution, interface chemistry, electronic band structure, optical behavior, and electrochemical performance. High-resolution electron microscopy and diffraction techniques—including scanning electron microscopy (SEM), Transmission electron microscopy (TEM), HRTEM, STEM, Selected-area electron diffraction (SAED), and EBSD—provide direct information on crystal orientation, lattice defects, grain boundaries, and phase evolution [6,137,179]. Complementary spectroscopic methods such as energy-dispersive X-ray spectroscopy (EDS), electron energy-loss spectroscopy (EELS), X-ray photoelectron spectroscopy (XPS), Raman spectroscopy, Fourier-transform infrared spectroscopy (FTIR), ultraviolet–visible (UV–Vis) spectroscopy, and photoluminescence (PL) spectroscopy reveal elemental composition, chemical bonding, oxidation states, phonon behavior, and electronic transitions [3,14,180,181]. Electrical, optical, and electrochemical measurements further quantify carrier mobility, recombination dynamics, charge-transfer kinetics, catalytic activity, and energy-conversion efficiency, thereby linking nanoscale structural features with device performance [177,178,182].

Recent developments have transformed characterization from conventional ex situ measurements toward in situ and operando methodologies, enabling direct observation of NW nucleation, crystal growth, phase transformations, ion diffusion, charge transfer, and catalytic reactions under realistic operating conditions [183–186]. In parallel, correlative characterization—where multiple complementary techniques are integrated within a unified experimental workflow—has emerged as a powerful strategy for connecting atomic-scale structural evolution with macroscopic electrical, optical, and electrochemical responses. These multidimensional approaches significantly improve mechanistic understanding and accelerate the rational design of next-generation semiconductor NWs for energy conversion, nanoelectronics, sensing, and optoelectronic applications [184–186]. Recent characterization platforms are also beginning to collapse the conventional separation between structural and functional measurements [187]. TEM-compatible microdevices and related correlative platforms can enable structural examination of an individual NW while the same object is subjected to electrical, thermal, optical, or electrochemical measurements, reducing uncertainty associated with comparing nominally similar but physically different specimens. Such same-object measurements are particularly valuable for establishing causal relationships among defects, interfaces, dimensions, dynamic structural evolution, and measured transport or reaction properties [187].

As illustrated in Fig. 5, modern characterization follows a hierarchical workflow that connects characterization with structure, composition, defects, interfaces, and performance. This integrated framework provides the experimental evidence necessary to validate advanced materials engineering (Section 2), interface engineering (Section 3), and computational predictions while establishing the scientific foundation for the advanced structural characterization techniques discussed in the following sections [176,177,184,188].

3.1. Structural characterization

Structural characterization is essential for resolving the morphology, crystallography, interfaces, and defect structures of inorganic semiconductor NWs. Because these features strongly influence electronic, optical, mechanical, and electrochemical behavior, complementary imaging and diffraction methods are required to correlate synthesis conditions with functional performance across multiple length scales [6,14,143,176,178].

SEM and field-emission SEM are widely used to evaluate NW diameter, length, aspect ratio, density, alignment, branching, surface roughness, catalyst distribution, and array uniformity. These techniques provide rapid assessment of morphological evolution during vapor–liquid–solid, chemical vapor deposition, and hydrothermal growth. However, because SEM primarily reveals surface morphology, it is generally complemented by transmission electron microscopy for detailed internal and crystallographic analysis [3,192,193].

TEM and HRTEM directly reveal internal crystal structures at subnanometer and atomic resolution. Lattice-fringe imaging enables determination of interplanar spacing, growth orientation, interface coherence, and defects such as stacking faults, twins, grain boundaries, and dislocations [179,194,195]. Aberration-corrected microscopy further resolves atomic columns and local lattice distortions, while scanning transmission electron microscopy combined with energy-dispersive X-ray spectroscopy or electron EELS correlates crystallography with elemental distribution, dopant segregation, and interface chemistry [195–197].

SAED identifies crystal symmetry, phase, epitaxial relationships, and NW growth direction. Electron backscatter diffraction (EBSD) complements SAED by mapping crystallographic orientation, texture, grain boundaries, and local strain over larger areas, including NW arrays and associated thin-film architectures [179,198–201]. Quantitative diffraction analysis follows Bragg's law:

$$n\lambda = 2d_{hkl}\sin\theta \tag{23}$$

where n is the diffraction order, λ is the incident wavelength, d_{hkl} is the interplanar spacing, and θ is the diffraction angle. This relationship supports lattice-parameter, phase, and orientation determination [200,202].

Recent advances in aberration-corrected TEM, 4D-STEM, differential phase-contrast STEM, and electron tomography enable three-dimensional mapping of interfaces, strain, defects, electric fields, and atomic configurations [188,196,203–205]. Machine-learning-assisted microscopy further supports automated defect recognition, orientation indexing, strain analysis, and image segmentation [206–208]. As demonstrated in Fig. 6, integrating SEM, TEM, HRTEM, STEM–EDS, SAED, and EBSD establishes comprehensive structure–composition–defect–interface–performance relationships for rational NW design [7,188,199,209].

3.2. Chemical and compositional characterization

Chemical and compositional characterization is fundamental to understanding the elemental distribution, chemical bonding, oxidation states, dopant incorporation, and interface chemistry of inorganic semiconductor NWs. While structural characterization reveals crystallography and defect structures, compositional analysis establishes the chemical origins of the electronic, optical, catalytic, and electrochemical properties that govern NW performance. Because these properties are highly sensitive to local compositional variations, advanced spectroscopic and microanalytical techniques are essential for correlating chemistry with functionality across multiple length scales [6,14].

Energy-dispersive X-ray spectroscopy (EDS), integrated with scanning electron microscopy (SEM) or scanning transmission electron microscopy (STEM), is widely used for rapid qualitative and quantitative elemental analysis. High-resolution elemental mapping reveals dopant distributions, alloy compositions, and core–shell architectures, enabling direct evaluation of compositional uniformity and interface integrity [194,196,209]. Electron EELS complements EDS by probing elemental composition, electronic structure, and chemical bonding with near-atomic spatial resolution, making it particularly effective for investigating oxidation states, band alignment, and interface chemistry in semiconductor heterostructures [196,197,214].

XPS provides quantitative information on surface composition,

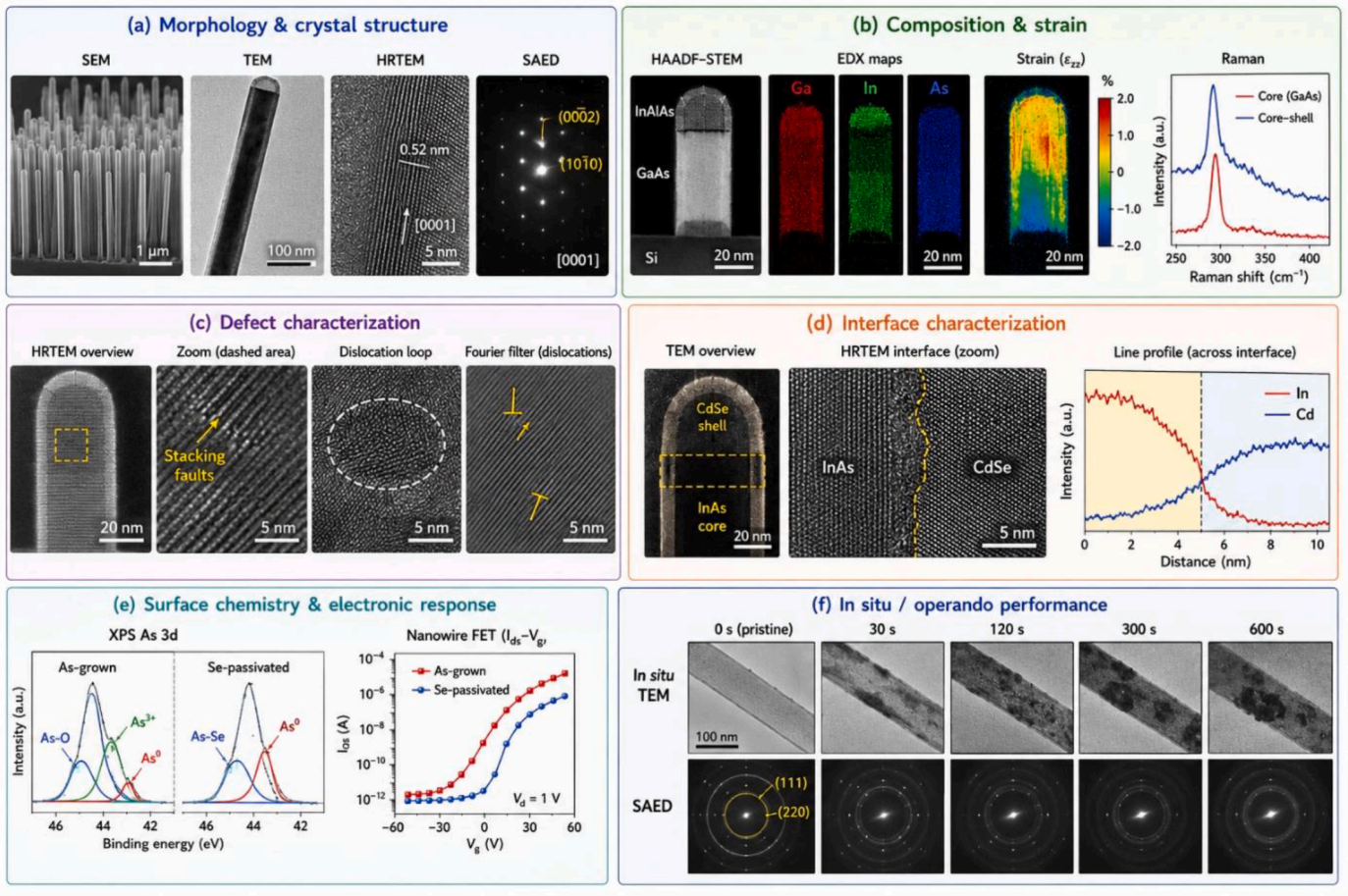


Fig. 5. Integrated multiscale characterization of inorganic semiconductor NWs for establishing structure–composition–defect–interface–performance relationships. Representative examples show (a) SEM/TEM/HRTEM/SAED characterization of ZnO nanowire morphology and crystallinity; (b) EDXS, strain mapping, and Raman analysis of GaAs-based core–shell NWs; (c) HRTEM identification of interfacial dislocations; (d) atomic-scale TEM/HRTEM analysis of an InAs/CdSe core–shell interface; (e) XPS surface-chemistry analysis correlated with electrical transport in GaAs NWs; and (f) in situ TEM/SAED tracking of structural evolution during Si-nanowire lithiation. Panels are adapted from Lin et al. [25], Balaghi et al. [189], Jo et al. [190], Kaladzhian et al. [27], Yang et al. [40], and Shen et al. [191], respectively, under the Creative Commons Attribution 4.0 International License (CC BY 4.0). Changes include cropping, resizing, relabeling, and integration into the present composite figure.

chemical bonding, oxidation states, and Fermi-level shifts through binding-energy analysis of photoemitted electrons [215–217]. Auger electron spectroscopy (AES) offers highly surface-sensitive elemental analysis with excellent lateral resolution, whereas secondary ion mass spectrometry (SIMS) enables depth-resolved dopant profiling with parts-per-million sensitivity for axially and radially doped NWs [198,218]. Inductively coupled plasma mass spectrometry (ICP–MS) further provides highly sensitive bulk elemental quantification for trace impurities and compositional verification [219].

The interaction of electromagnetic radiation with matter is commonly described by the Beer–Lambert law,

$$A = \varepsilon c l \tag{24}$$

where A is absorbance, ε is the molar absorption coefficient, c is the concentration of the absorbing species, and l is the optical path length. This relationship forms the basis of numerous spectroscopic techniques used to quantify chemical species and monitor compositional changes during NW synthesis and surface functionalization [220].

Recent advances in atom probe tomography (APT), cryogenic electron microscopy (cryo-EM), synchrotron-based X-ray spectroscopy, and correlative STEM–EELS–XPS have enabled three-dimensional chemical mapping with near-atomic resolution, providing unprecedented insight into dopant segregation, interface diffusion, compositional gradients, and defect chemistry [221,222]. Furthermore, ML-assisted spectral analysis is accelerating automated peak identification, oxidation-state determination, and multicomponent spectral interpretation, significantly improving analytical accuracy and throughput [203,208]. Together, these complementary techniques provide a comprehensive understanding of elemental composition and chemical bonding, forming the foundation for advanced crystal structure and phase characterization of semiconductor NWs.

3.3. Crystal structure and phase characterization

Crystal structure and phase characterization are essential for understanding the atomic arrangement, phase composition, crystallinity, and structural evolution of inorganic semiconductor NWs. Because their electronic, optical, catalytic, and mechanical properties are intrinsically governed by crystal structure, accurate identification of crystalline phases, lattice distortions, and structural defects is critical for optimizing device performance. Advanced diffraction and vibrational spectroscopic techniques provide complementary insights into crystallographic order, phase purity, lattice strain, and structural transformations under both synthesis and operating conditions [14,200].

XRD remains the principal technique for identifying crystal structure and phase composition in semiconductor NWs. Diffraction peak positions reveal crystalline phases, while peak intensities and widths provide information on preferred orientation, crystallinity, crystallite size, and

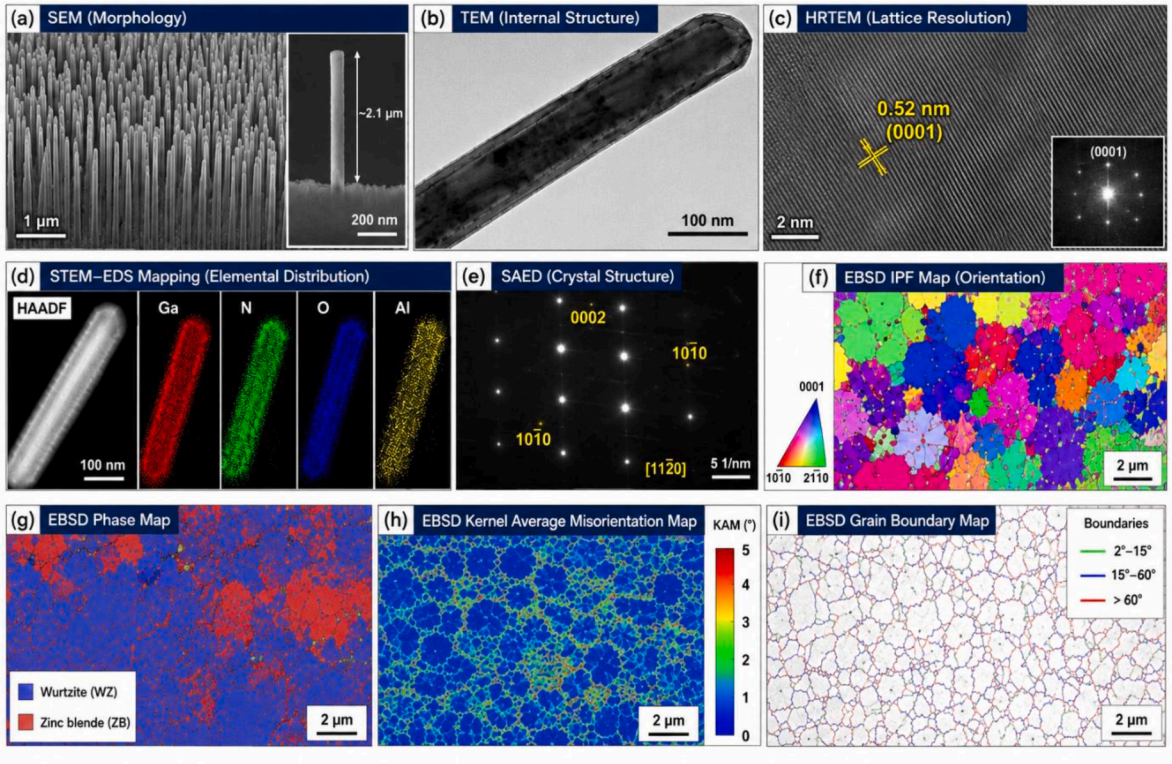


Fig. 6. Integrated structural characterization of inorganic semiconductor NWs using complementary electron microscopy and diffraction techniques. (a) SEM image showing the morphology, vertical alignment, diameter uniformity, and surface topology of semiconductor NW arrays, providing information on growth quality, density, and aspect ratio. (b) TEM image of an individual NW revealing the internal microstructure, crystallinity, shell thickness, and structural integrity. (c) HRTEM image displaying atomic lattice fringes and interplanar spacing together with the corresponding fast Fourier transform (FFT) pattern for crystallographic analysis and lattice indexing. (d) High-angle annular dark-field scanning transmission electron microscopy (HAADF-STEM) image and STEM–energy-dispersive X-ray spectroscopy (STEM–EDS) elemental maps illustrating nanoscale elemental distribution, compositional uniformity, and core–shell architecture. (e) SAED pattern confirming crystal phase, crystallographic orientation, lattice symmetry, and single-crystalline growth characteristics. (f) Electron backscatter diffraction (EBSD) inverse pole figure (IPF) orientation map showing grain orientation and crystallographic texture. (g) EBSD phase map identifying the spatial distribution of different crystal phases within the NW system. (h) EBSD kernel average misorientation (KAM) map revealing local lattice distortion, plastic deformation, and strain accumulation. (i) EBSD grain-boundary misorientation map illustrating grain-boundary networks and the distribution of low- and high-angle grain boundaries. Panels are reproduced or adapted from the following sources: (a) Dávila et al., *Nano Energy*, 2012 [210]; (b,c) Dogan et al., *Nature Communications*, 2018 [211]; (d) Seifner et al., *ACS Nano*, 2018 [212], distributed under a Creative Commons Attribution licence; (e) Zhu et al., *Advanced Science*, 2017 [213]; and (f–i) Prikhodko et al., *Ultramicroscopy*, 2008 [198]. Copyright and licensing remain with the respective authors and publishers.

microstrain [200,223]. High-resolution XRD is particularly effective for distinguishing polymorphs such as zinc blende and wurtzite in III–V semiconductor NWs and anatase–rutile phase transitions in TiO_2 NWs [179,224]. Synchrotron XRD further improves structural characterization through its high brilliance and angular resolution, enabling detection of subtle lattice distortions, residual stresses, and phase transformations inaccessible to conventional laboratory XRD [225,226].

Crystallite size is commonly estimated using the Scherrer equation

$$D = \frac{K\lambda}{\beta \cos\theta} \tag{25}$$

where D is the average crystallite size, K is the shape factor, λ is the X-ray wavelength, β is the full width at half maximum (FWHM), and θ is the Bragg diffraction angle. This relationship is widely used to quantify crystal growth, grain refinement, and phase evolution in semiconductor NWs [223].

Neutron diffraction complements XRD by providing enhanced sensitivity to light elements, including hydrogen, lithium, and oxygen, making it valuable for probing lattice occupancy, defect structures, and ion transport [227]. Raman spectroscopy further characterizes lattice vibrations, crystal symmetry, phase transitions, residual stress, defect density, and electron–phonon interactions, with peak shifts and linewidth variations serving as sensitive indicators of strain, crystallinity, alloying, and doping [228–230].

Recent advances in operando synchrotron XRD, time-resolved Raman spectroscopy, and high-energy neutron scattering enable real-time monitoring of crystal growth, phase transformations, and strain evolution during NW synthesis and device operation, and atomic imaging of phase transitions and morphology transformations [183]. Integrated with electron microscopy, spectroscopy, and computational modeling, these techniques establish comprehensive relationships between phase stability, lattice dynamics, and functional performance, providing the structural foundation for the electronic and optical characterization methods discussed in the following section.

3.4. Electronic and optical characterization

Electronic and optical characterization provides essential insight into the energy-band structure, charge transport, carrier dynamics, and light–matter interactions governing inorganic semiconductor NW performance. These measurements establish quantitative relationships among bandgap energy, carrier concentration, mobility, recombination lifetime, and quantum efficiency, supporting the optimization of NWs for PVs, photocatalysis, PEC water splitting, photodetectors, light-emitting diodes, and nanoelectronics [14].

Ultraviolet–visible absorption spectroscopy is widely used to evaluate optical absorption and estimate the optical bandgap. The relationship is commonly expressed as

$$(\alpha h\nu)^n = A\left(h\nu - E_g\right) \tag{26}$$

where α is the absorption coefficient, $h\nu$ is photon energy, A is a proportionality constant, E_g is the optical bandgap, and n depends on the transition type. Tauc analysis reveals bandgap changes associated with quantum confinement, alloying, strain, and defect engineering [231].

Photoluminescence and time-resolved photoluminescence probe band-edge emission, defect-assisted recombination, interface quality, and carrier lifetime. Spatially resolved cathodoluminescence further maps optical emission, doping variations, and nonradiative defects within individual NWs [232–234]. These techniques are particularly effective for linking crystal defects and heterointerfaces to radiative efficiency.

Electrical transport is commonly quantified through Hall-effect and field-effect measurements, which determine carrier concentration, conductivity, and mobility. Hall mobility is given by

$$\mu_H = \sigma R_H \tag{27}$$

where μ_H is Hall mobility, σ is conductivity, and R_H is the Hall coefficient. Single-NW Hall devices have enabled direct assessment of doping and transport without relying solely on geometry-dependent field-effect models [235–237]. Kelvin probe force microscopy complements these measurements by mapping surface potential and work function, revealing band bending, Fermi-level alignment, and local electric fields across heterojunctions [238].

Ultrafast transient absorption spectroscopy and time-resolved optical methods extend characterization into femtosecond-to-nanosecond regimes, resolving exciton generation, trapping, recombination, and charge transfer in individual NWs; ultrafast spectroscopy of quantum-confined states in a single CdSe nanow [239]. Collectively, these approaches establish comprehensive electronic-structure–carrier-dynamics–performance relationships and provide the foundation for subsequent electrochemical characterization.

3.5. Electrochemical characterization

Electrochemical characterization is essential for evaluating charge-transfer kinetics, catalytic activity, reaction mechanisms, and operational stability of inorganic semiconductor NWs used in PEC water splitting, electrocatalysis, batteries, supercapacitors, CO_2 conversion, and sensing. These measurements connect NW morphology, composition, and interfaces with electron transfer, ion transport, reaction rates, and durability [240–242].

Cyclic voltammetry (CV) identifies redox processes, electrochemical reversibility, capacitive behavior, and accessible surface states. LSV is commonly used to determine onset potential, overpotential, and current density for the hydrogen evolution and oxygen evolution reactions. Tafel analysis further relates overpotential to reaction rate and provides mechanistic information, although meaningful comparisons require standardized electrolyte, loading, resistance correction, and surface-area normalization [240,241]. NW arrays are particularly advantageous because their high surface area and direct electrical pathways can improve catalytic utilization and mass transport [242,243].

ESI probes solution resistance, interfacial capacitance, charge-transfer resistance, and diffusion limitations. A simplified Randles response is expressed as

$$Z(\omega) = R_s + \left(\frac{1}{R_{ct}} + j\omega C_{dl}\right)^{-1} \tag{28}$$

where R_s is solution resistance, R_{ct} is charge-transfer resistance, C_{dl} is double-layer capacitance, j is the imaginary unit, and ω is angular frequency. Lower R_{ct} generally indicates faster interfacial charge transfer. Although C_{dl} is often used to approximate electrochemically active surface area, this interpretation requires material-specific capacitance assumptions.

Chronoamperometry and chronopotentiometry assess current or potential stability during prolonged operation and reveal catalyst degradation, corrosion, passivation, and mass-transport limitations [244]. Advanced scanning electrochemical microscopy spatially maps local reactivity, while electrochemical quartz-crystal microbalance measurements track interfacial mass changes during deposition, dissolution, and ion insertion [245,246]. When coupled with operando spectroscopy, microscopy, ML, and multiscale modeling, these methods reveal catalyst reconstruction and performance-limiting mechanisms under realistic conditions.

3.6. Correlative and multimodal characterization

Correlative and multimodal characterization has emerged as a powerful strategy for elucidating the complex structure–composition–property–performance relationships of inorganic semiconductor NWs. Unlike conventional single-technique analyses, this approach integrates complementary imaging, spectroscopy, diffraction, and computational methods to simultaneously probe morphology, crystallography, chemistry, electronic structure, and functional behavior across multiple spatial and temporal scales. By linking atomic-scale observations with device-level performance, correlative characterization provides mechanistic insight into NW growth, interface engineering, defect evolution, and degradation processes [188,194,196,203].

A representative example is the integration of SEM with electron backscatter diffraction (EBSD), where SEM reveals NW morphology while EBSD maps crystallographic orientation, grain boundaries, texture, and local strain [199,201]. Similarly, TEM combined with electron EELS simultaneously resolves atomic structure, elemental distribution, oxidation states, and electronic bonding, making it particularly valuable for investigating heterojunctions, core–shell NWs, and defect-rich interfaces [197,209]. Correlative optical characterization further integrates Raman spectroscopy with PL to establish quantitative relationships among crystal quality, lattice strain, phonon behavior, defect states, and carrier recombination dynamics [228,230]. Likewise, combining XRD with DFT enables experimental validation of crystal structures, lattice distortions, phase stability, and electronic band structures, strengthening predictive materials design [247].

Recent advances in AI have transformed multimodal characterization through automated image segmentation, crystallographic indexing, spectral interpretation, and defect recognition from large experimental datasets [208,248,249]. Deep learning-assisted analysis of electron microscopy, Raman spectroscopy, diffraction, and synchrotron data substantially improves analytical accuracy and throughput. Furthermore, integrating multimodal datasets with digital twin frameworks enables continuous synchronization between experiments and physics-based simulations, supporting [250] real-time prediction of microstructural evolution and device performance [251]. As illustrated in Fig. 7, this convergence of advanced characterization, computational modeling, and AI establishes a comprehensive analytical ecosystem that accelerates semiconductor NW discovery and provides the experimental foundation for autonomous materials engineering. The advanced characterization techniques for inorganic semiconductor NWs discussed throughout this section, together with their operating principle, advantages, limitations, representative applications, and supporting literature, are summarized in Table 3.

4. Green energy applications

Inorganic semiconductor NWs have emerged as key materials for green energy technologies due to their distinctive structural, electronic, and optical properties. Features such as high aspect ratio, large surface area, tunable band structure, and efficient charge transport enable superior energy conversion and storage compared to bulk counterparts [23,256,257]. Progress in synthesis, heterostructure design, surface passivation, and defect control has further enhanced their performance

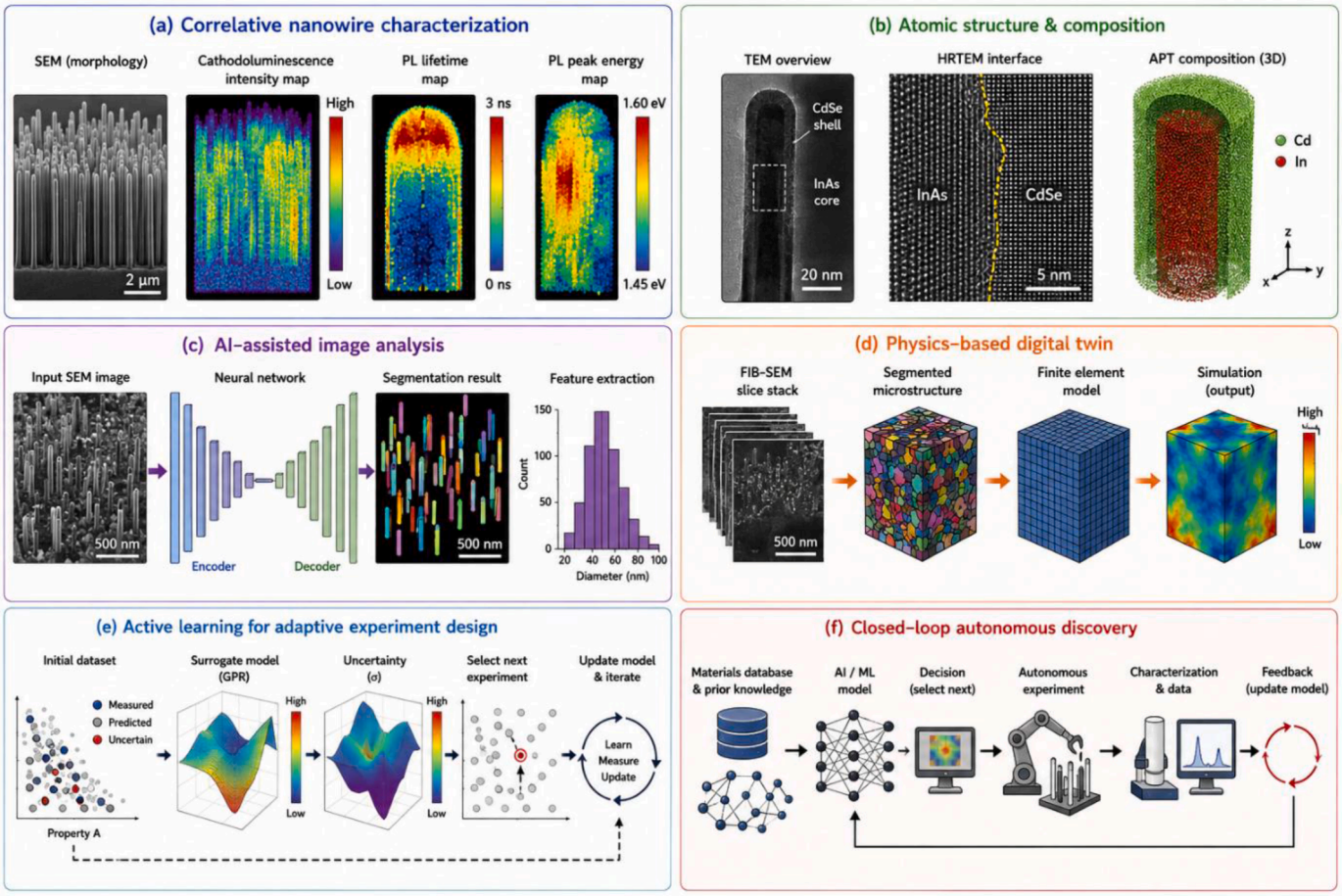


Fig. 7. AI-enabled correlative characterization ecosystem for autonomous semiconductor nanowire engineering. Representative examples show (a) correlated structural and optoelectronic mapping of GaAs/AlGaAs NWs, (b) atomic-scale structural and compositional characterization of InAs/CdSe core–shell NWs, (c) AI-assisted electron-microscopy image segmentation, (d) reconstruction of experimental microstructures into physics-based digital twins, (e) active-learning-guided selection of subsequent experiments or calculations, and (f) closed-loop autonomous materials characterization and optimization. Panels are adapted from Das et al. [252], Kaladzhian et al. [27], Rühle et al. [253], Bolyachkin et al. [254], Lookman et al. [255], and Kusne et al. [29], respectively, under the Creative Commons Attribution 4.0 International License (CC BY 4.0). Changes include cropping, resizing, relabeling, and integration into the present composite figure.

across applications including solar energy conversion, hydrogen generation, carbon dioxide reduction, electrochemical storage, thermoelectrics, and flexible electronics [10,258]. This section highlights their roles in sustainable energy systems, focusing on underlying mechanisms, material systems, recent advances, performance benchmarks, and challenges toward scalable deployment.

4.1. Photovoltaic (PV)

Semiconductor NWs have attracted considerable attention as efficient photoabsorbers for next-generation PVsystems due to their one-dimensional architecture, which simultaneously enhances light absorption, carrier separation, and optical confinement while minimizing material usage [259]. In contrast to conventional planar solar cells, NW-based devices—particularly those employing radial p–n junctions—separate the pathways of photon absorption and charge carrier collection. Light is primarily absorbed along the axial direction of the NW, whereas photogenerated carriers are extracted radially over short distances. This geometry significantly reduces recombination losses and enables efficient charge collection even in materials with limited minority-carrier diffusion lengths [133,259,260].

The power conversion efficiency of a photovoltaic device is defined as the ratio of maximum electrical output power to incident solar power under standard AM 1.5G illumination conditions (100 $mWcm^{-2}$). The maximum output power depends on three key parameters: the open-circuit voltage, the short-circuit current density, and the fill factor.

A major strength of semiconductor NWs lies in their superior light-trapping capability. Their high aspect ratios and subwavelength dimensions promote optical resonances, multiple scattering, and waveguiding phenomena, allowing absorption levels that exceed those predicted by classical Lambert–Beer behavior. As a result, NW arrays can achieve strong optical absorption with absorber layers only a few micrometers thick, thereby reducing material consumption without compromising photocurrent generation [259,260].

Silicon NWs remain the most extensively studied system due to their earth abundance, environmental compatibility, and integration with established CMOS technologies. Radial p–n junction Si NW devices exhibit improved light absorption and carrier collection relative to planar counterparts [139,261]. III–V materials such as GaAs and InP offer further advantages. GaAs NWs, with a direct bandgap of approximately 1.42 eV and high carrier mobility, are well suited for high-efficiency single-junction and tandem solar cells [139,261]. InP NWs, characterized by an optimal direct bandgap (~1.34 eV), low surface recombination when properly passivated, and strong radiation resistance, are particularly promising for both terrestrial and space-based photovoltaic applications [51,262].

Despite substantial advances in optical management, radial-junction design, and surface passivation, a persistent gap remains between the theoretical potential of III–V NW photovoltaics and experimentally demonstrated device efficiencies [263]. Recent assessments indicate

Table 3
Advanced characterization techniques for inorganic semiconductor NWs.

Characterization Technique	Operating Principle	Information Obtained	Typical Spatial Resolution	Major Advantages	Limitations	Representative Applications
SEM	Scanning focused electron beam over specimen surface	Surface morphology, NW diameter, alignment, density, fracture morphology	1–10 nm	Rapid imaging, large field of view, minimal sample preparation	Limited crystallographic and chemical information	Morphology analysis, growth evaluation, device inspection
Field-Emission SEM (FESEM)	High-brightness field-emission electron source	High-resolution surface morphology	<1–2 nm	Superior resolution and image contrast	Higher instrument cost	High-aspect-ratio NWs, catalyst morphology
TEM	Electron transmission through ultrathin specimen	Internal microstructure, crystal defects, interfaces	0.1–0.2 nm	Atomic-resolution imaging	Complex specimen preparation	Crystal defects, heterostructures, core–shell NWs
HRTEM	Phase-contrast imaging of lattice fringes	Atomic lattice, interplanar spacing, dislocations	<0.1 nm	Direct atomic-scale structural observation	Beam-sensitive materials may degrade	Atomic interface characterization
Scanning TEM (STEM)	Focused scanning electron probe through specimen	Atomic structure with simultaneous spectroscopy	0.05–0.2 nm	Enables simultaneous EDS and EELS mapping	Requires advanced instrumentation	Atomic chemical mapping
Selected Area Electron Diffraction (SAED)	Electron diffraction from selected crystal region	Crystal symmetry, phase identification, orientation	Nanometer scale	Accurate local crystallography	Small sampling volume	Phase identification, polytypism
Electron Backscatter Diffraction (EBSD)	Diffraction of backscattered electrons	Grain orientation, texture, grain boundaries	20–100 nm	Large-area crystallographic mapping	Limited for very small NWs	Crystal orientation analysis
Energy-Dispersive X-ray Spectroscopy (EDS)	Detection of characteristic X-rays	Elemental composition, elemental mapping	1–10 nm (STEM); ~100 nm (SEM)	Fast elemental analysis	Poor sensitivity for light elements	Dopant distribution, alloy composition
Electron EELS	Measurement of electron energy losses	Chemical bonding, oxidation state, elemental distribution	<1 nm	Atomic-scale chemical analysis	Requires TEM	Interface chemistry, valence state analysis
XPS	Photoelectron emission induced by X-rays	Surface composition, oxidation states, chemical bonding	Sampling depth 5–10 nm	Excellent surface sensitivity	Limited bulk information	Surface passivation, interface chemistry
Secondary Ion Mass Spectrometry (SIMS)	Sputtering and mass analysis of secondary ions	Dopant concentration, elemental depth profiling	10–100 nm depth	Extremely high elemental sensitivity	Destructive analysis	Dopant profiling, impurity analysis
Atom Probe Tomography (APT)	Field evaporation with time-of-flight mass spectrometry	Three-dimensional atomic composition	~0.2–0.5 nm	Near-atomic 3D chemical mapping	Complex specimen preparation	Dopant segregation, interface composition
XRD	XRD by crystal planes	Crystal structure, phase identification, crystallite size	Bulk averaged	Non-destructive, quantitative phase analysis	Limited spatial resolution	Phase evolution, crystallinity
Synchrotron XRD	High-brilliance synchrotron X-rays	Residual strain, phase transformation, lattice distortion	High reciprocal-space resolution	Exceptional sensitivity	Limited facility access	Operando structural analysis
Raman Spectroscopy	Inelastic scattering of monochromatic light	Crystal quality, phonons, lattice strain, phase	~0.5–1 μm	Non-destructive, rapid	Weak Raman scattering for some materials	Strain mapping, phase identification
Photoluminescence (PL)	Radiative recombination following optical excitation	Bandgap, defects, recombination pathways	~1 μm	Sensitive to defect states	Requires optically active materials	Optical quality evaluation
Time-Resolved PL (TRPL)	Time-dependent photoluminescence decay	Carrier lifetime, recombination dynamics	Optical diffraction limited	Direct carrier lifetime measurement	Specialized instrumentation	Charge separation efficiency
Cathodoluminescence (CL)	Electron beam-induced light emission	Local optical emission, defect distribution	10–100 nm	Correlates optical and structural properties	Vacuum operation required	Localized defect characterization
Hall Effect Measurement	Voltage generated under magnetic field	Carrier concentration, mobility, conductivity	Bulk measurement	Quantitative transport parameters	Difficult for individual NWs	Electrical transport analysis
Kelvin Probe Force Microscopy (KPFM)	Atomic force microscopy with surface potential mapping	Work function, surface potential, band bending	10–50 nm	High-resolution electrical mapping	Surface sensitive	Heterojunction characterization
ESI	Frequency-dependent impedance measurement	Charge-transfer resistance, capacitance, diffusion	Device level	Comprehensive kinetic information	Requires equivalent circuit fitting	Electrocatalysis, PEC characterization
Scanning Electrochemical Microscopy (SECM)	Local electrochemical probe scanning	Local catalytic activity, reaction kinetics	~1–10 μm	Spatially resolved electrochemistry	Slow scanning speed	Electrocatalyst mapping
Operando Synchrotron Spectroscopy		Dynamic phase evolution, electronic structure	Technique dependent		Specialized facilities required	

(*continued on next page*)

Table 3 (*continued*)

Characterization Technique	Operating Principle	Information Obtained	Typical Spatial Resolution	Major Advantages	Limitations	Representative Applications
	Real-time synchrotron characterization during operation			Direct observation under realistic conditions		Batteries, photocatalysis, PEC devices
Correlative Multimodal Characterization	Integration of multiple complementary techniques	Structure–composition–property relationships	Multi-scale	Comprehensive materials understanding	Complex data integration	Digital twins, AI-assisted materials discovery

that junction quality, surface recombination, contact resistance, array uniformity, and scalable fabrication increasingly determine the device-level performance ceiling. This distinction shifts the research question from whether NWs can provide exceptional light trapping to whether their nanoscale optical advantages can be retained after electrical contacting, array integration, and large-area manufacturing [263].

Advances in surface passivation, heterostructure design, and tandem integration have led to significant improvements in NW solar cell performance. InP NW array devices have achieved certified efficiencies exceeding 13% [51], while GaAs NW solar cells have reached efficiencies close to 19% through optimized surface treatment and junction engineering. In parallel, conventional crystalline silicon technologies have surpassed 27% efficiency, and silicon–perovskite tandem cells have exceeded 34% [264], underscoring the critical role of nanostructured architectures and interface engineering in advancing photovoltaic performance toward theoretical limits.

Fig. 8 illustrates the working principles of NW-based photovoltaic devices. Vertically aligned NW arrays form radial p–n junctions that enable efficient absorption of incident solar radiation. The resulting electron–hole pairs are separated by the built-in electric field and transported to the respective electrodes with minimal recombination. At the individual NW level, radial carrier collection minimizes diffusion distances, thereby enhancing efficiency. The corresponding energy band diagram shows photon-induced excitation across the bandgap and subsequent carrier separation. Overall, NW photovoltaic architectures offer key advantages, including enhanced light trapping, efficient carrier transport, reduced reflection losses, and improved energy conversion efficiency compared with traditional planar designs.

4.2. PEC water splitting

PEC water splitting offers a direct route for converting solar energy into hydrogen using semiconductor-based photoelectrodes. When illuminated with photons of sufficient energy, electrons are promoted from the VB to the conduction band, generating electron–hole pairs. For efficient operation, the semiconductor band edges must straddle the redox potentials of water, such that the conduction band minimum is more negative than the hydrogen evolution potential (0 V vs. RHE) and the VB maximum is more positive than the oxygen evolution potential (+1.23 V vs. RHE), thereby enabling overall water splitting [268].

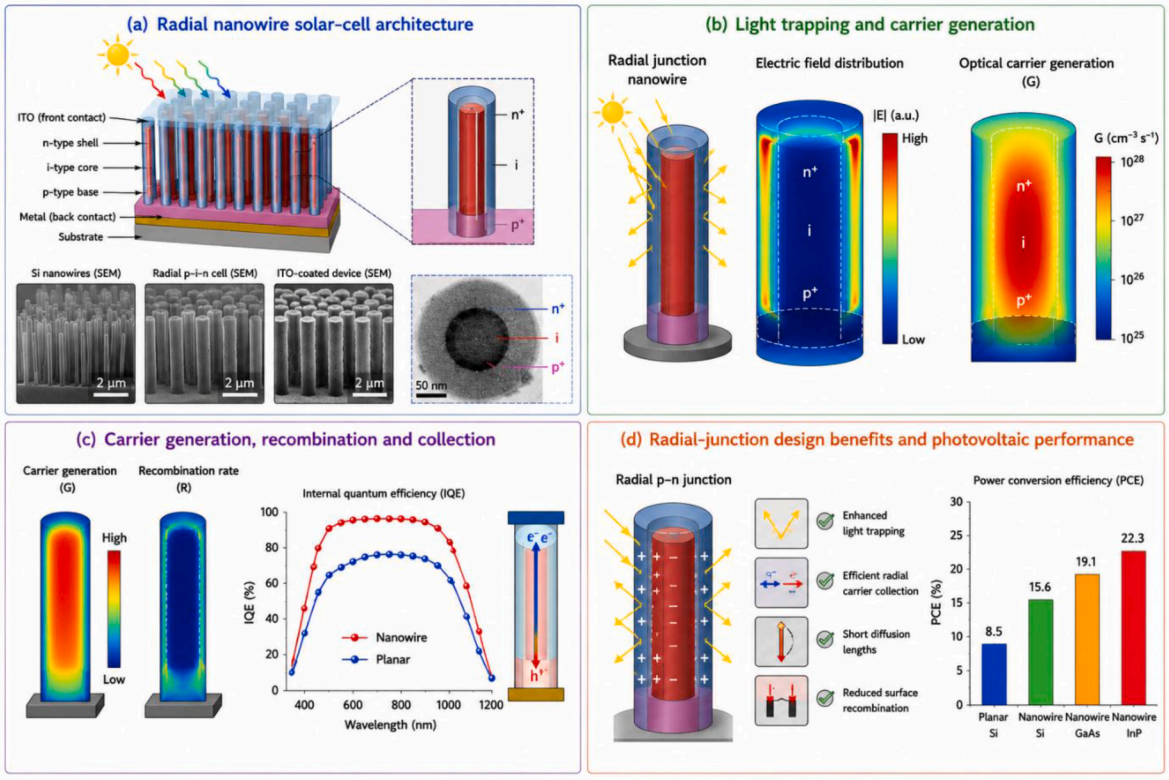


Fig. 8. Nanowire photovoltaic architectures and operating mechanisms for enhanced solar-energy conversion. Representative examples show (a) coaxial radial-junction SiNW solar-cell architecture, (b) light trapping and enhanced photocarrier generation in radial SiNW structures, (c) spatial carrier generation, recombination, and extraction in standing nanowire photovoltaic devices, and (d) radial-junction design effects on photovoltaic efficiency. Panels are adapted from Yu et al. [265], Ko et al. [266], Zeng et al. [267], and Cabrera-España and Rahman [260], respectively. Panels (a) and (c) are adapted under CC BY 3.0, while panels (b) and (d) are adapted under CC BY 4.0. Changes include cropping, resizing, relabeling, and integration into the present composite figure.

A typical PEC configuration comprises a photoanode and a photocathode. At the photoanode, photogenerated holes oxidize water to produce oxygen, while at the photocathode, electrons reduce protons to generate hydrogen. These coupled half-reactions together drive the overall solar-assisted water-splitting process.

Fig. 9 illustrates the operating principles of semiconductor NW-based PEC systems. Vertically aligned NW photoelectrodes absorb incident solar radiation and generate charge carriers that are efficiently separated and transported to reaction sites. Electrons flow through the external circuit toward the photocathode to drive the HER, while holes remain at the photoanode to facilitate oxygen evolution. At the nanoscale, the radial geometry of individual NWs shortens carrier transport distances, promoting efficient charge separation and minimizing recombination. The corresponding band alignment highlights the requirement for energetically favorable positions of the conduction and valence bands relative to the redox potentials of water. The complete PEC process involves hydrogen evolution ($2H^+ + 2e^- \rightarrow H_2$) at the cathode and oxygen evolution ($2H_2O \rightarrow O_2 + 4H^+ + 4e^-$) at the anode, yielding the overall reaction ($2H_2O \rightarrow 2H_2 + O_2$). NW architectures offer key advantages, including enhanced light absorption, improved charge separation, rapid carrier transport, and reduced recombination losses, all of which contribute to higher solar-to-hydrogen conversion efficiency.

Several semiconductor NW materials have been extensively investigated for PEC applications. TiO_2 NWs are chemically stable but limited by their wide bandgap (3.0–3.2 eV), which confines absorption to the ultraviolet region [72]. Hematite (Fe_2O_3) exhibits a narrower bandgap (~2.1 eV) and visible-light activity, although its performance is constrained by short hole diffusion lengths and slow oxygen evolution kinetics [273]. $BiVO_4$ is a leading visible-light photoanode, but its activity must be evaluated together with durability. Orientation, facet, interface, and cocatalyst engineering can raise the photocurrent to approximately 6.0–6.1 mA cm^{-2} at 1.23 V_RHE under one-sun conditions, approaching a large fraction of the theoretical photocurrent [274]. However, sustained operation is limited by surface recombination, vanadium dissolution, photocorrosion, cocatalyst/interface evolution, and electrolyte-dependent degradation [275]. Reported stability therefore spans very different timescales depending on the protection strategy; for example, Au/$Co(OH)_x$-modified $BiVO_4$ has shown stable continuous output for approximately 42 h [275], while more strongly anchored interfacial protection strategies have demonstrated substantially longer operation in recent studies. Consequently, comparisons should report photocurrent retention together with test duration, electrolyte composition, applied potential, illumination intensity, Faradaic efficiency, and post-operation structural/chemical analysis. High initial photocurrent alone should not be interpreted as evidence of practical PEC durability [274,275].

Recent progress in heterostructure engineering, cocatalyst incorporation, and surface passivation has markedly enhanced the performance of NW-based PEC devices. Advanced photoelectrodes now achieve photocurrent densities exceeding 8 $mAcm^{-2}$, onset potentials below 0.4 V vs. RHE, and solar-to-hydrogen efficiencies approaching or

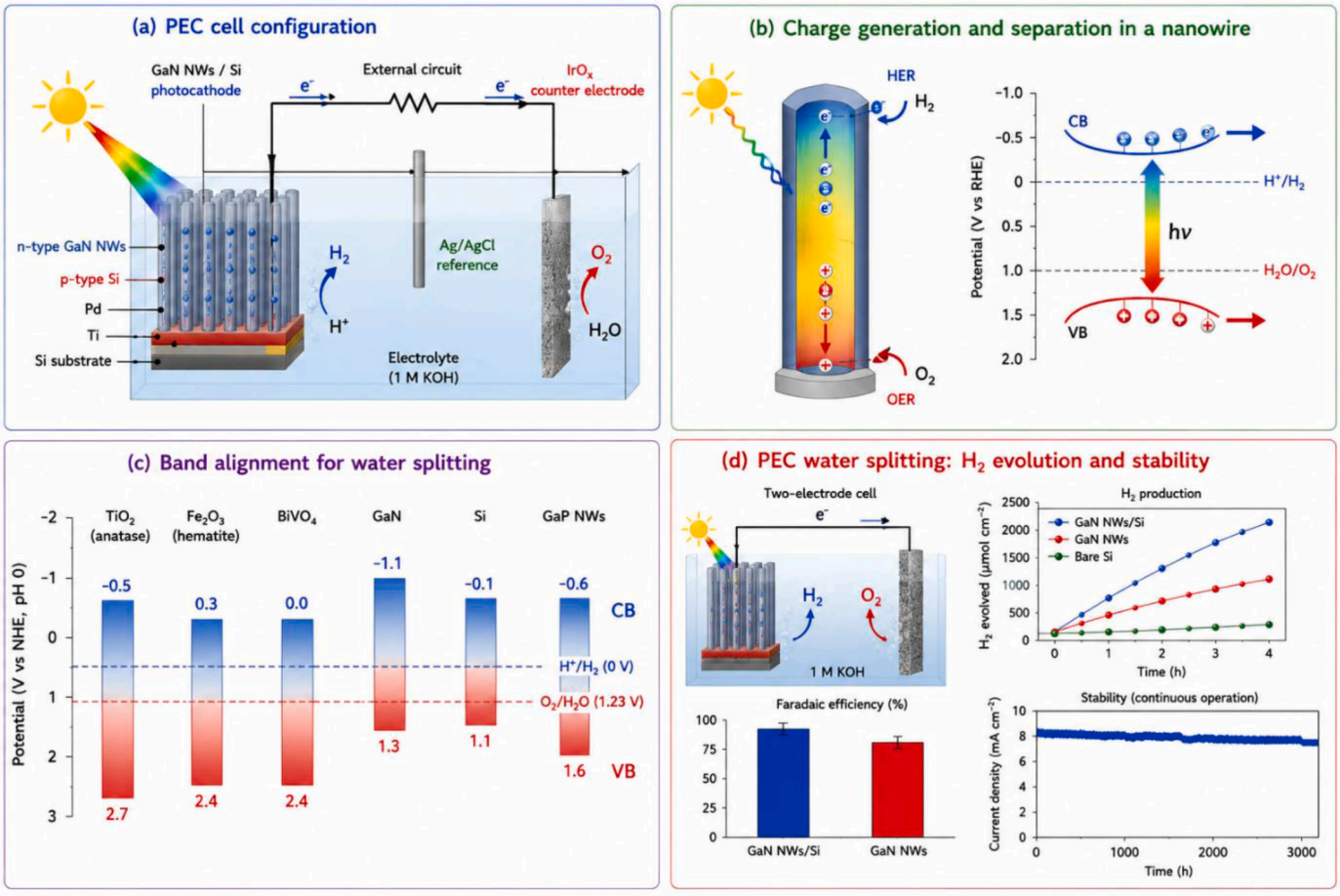


Fig. 9. Photoelectrochemical water splitting using semiconductor nanowire photoelectrodes. Representative examples illustrate (a) a GaN-nanowire/Si PEC-cell configuration, (b) photogenerated charge separation and directional carrier transport in semiconductor NWs, (c) semiconductor band-edge positions relative to the H^+/H_2 and O_2/H_2O redox potentials, and (d) nanowire-enabled photoelectrochemical hydrogen evolution, Faradaic efficiency, and operational stability. Panels are adapted from Xiao et al. [269], Chowdhury et al. [270], Standing et al. [271], and Dong et al. [272], respectively, under the Creative Commons Attribution 4.0 International License (CC BY 4.0). Changes include cropping, resizing, relabeling, and integration into the present composite figure.

surpassing 10% in tandem configurations, highlighting the promise of semiconductor NWs for scalable solar hydrogen generation [10,273].

4.3. Hydrogen evolution

The HER represents the cathodic process in both electrochemical water splitting and PEC hydrogen generation, where electrons reduce protons or water molecules to produce molecular hydrogen. In acidic environments, HER proceeds via proton reduction, whereas in alkaline conditions it involves water dissociation followed by hydrogen formation.

The performance of HER catalysts is largely governed by their intrinsic activity, typically assessed through the overpotential (η) required to reach a current density of 10 mA cm^{-2} and the Tafel slope, which provides insight into reaction kinetics. Catalysts exhibiting low overpotentials (generally below 100 mV) and small Tafel slopes (below 60 mV dec^{-1}) are indicative of rapid reaction rates and high catalytic efficiency [276,277].

Fig. 10 presents the key photocatalytic mechanisms underlying solar-driven hydrogen production and carbon dioxide reduction using semiconductor NWs. Upon illumination with photons of energy equal to or exceeding the bandgap, electrons are excited from the VB to the conduction band, generating electron–hole pairs. These carriers are then effectively separated and transported to the catalyst surface, where electrons drive reduction reactions such as hydrogen evolution, while holes participate in oxidation processes.

One-dimensional semiconductor NWs offer several advantages for HER, including large surface-to-volume ratios, abundant active sites, and short charge transport pathways that facilitate rapid electron transfer and reduced recombination. For instance, Mo S_2 NWs expose a high density of catalytically active edge sites, NiO NWs demonstrate strong chemical stability in alkaline electrolytes, and CoP NWs combine high electrical conductivity with catalytic activity comparable to noble metals [142,280]. Platinum-decorated silicon NWs remain among the most effective photocathodes due to their minimal overpotential, efficient charge transfer, and high hydrogen generation rates [281]. Furthermore, recent advances in heterostructure design, cocatalyst integration, and defect engineering have significantly improved the activity and durability of NW-based HER systems, reinforcing their potential for efficient and scalable solar hydrogen production [282].

4.4. Photocatalysis

Semiconductor NWs have emerged as efficient photocatalysts due to their one-dimensional structure, which enhances light absorption, accelerates charge transport, and suppresses electron–hole recombination. When irradiated with photons of energy equal to or exceeding the bandgap, electrons are excited to the conduction band, leaving holes in the valence band. These charge carriers initiate surface redox reactions that generate reactive oxygen species, notably superoxide and hydroxyl radicals, which are highly effective in decomposing organic contaminants and inactivating microorganisms into benign end products [283,284].

Common NW photocatalysts, including TiO_2, ZnO, WO_3, CdS, and GaN, exhibit improved activity due to their high surface area and efficient charge separation. Beyond environmental remediation, these materials are also applied in solar hydrogen generation, CO_2 photoreduction, and self-cleaning technologies. Performance has been further enhanced through heterojunction formation, cocatalyst incorporation, and defect engineering, which improve visible-light absorption and catalytic efficiency [285–287]. As illustrated in Fig. 10(b), photogenerated electrons migrate to catalytic sites such as Pt, MoS_2, Ni, or CoP to drive hydrogen evolution, while holes oxidize water to sustain the reaction cycle.

4.5. CO_2 reduction

Photocatalytic and PEC CO_2 reduction provide a pathway for converting greenhouse gases into useful fuels and chemicals using solar energy. Upon illumination, semiconductor NW photocathodes generate electron–hole pairs, where electrons participate in CO_2 reduction and

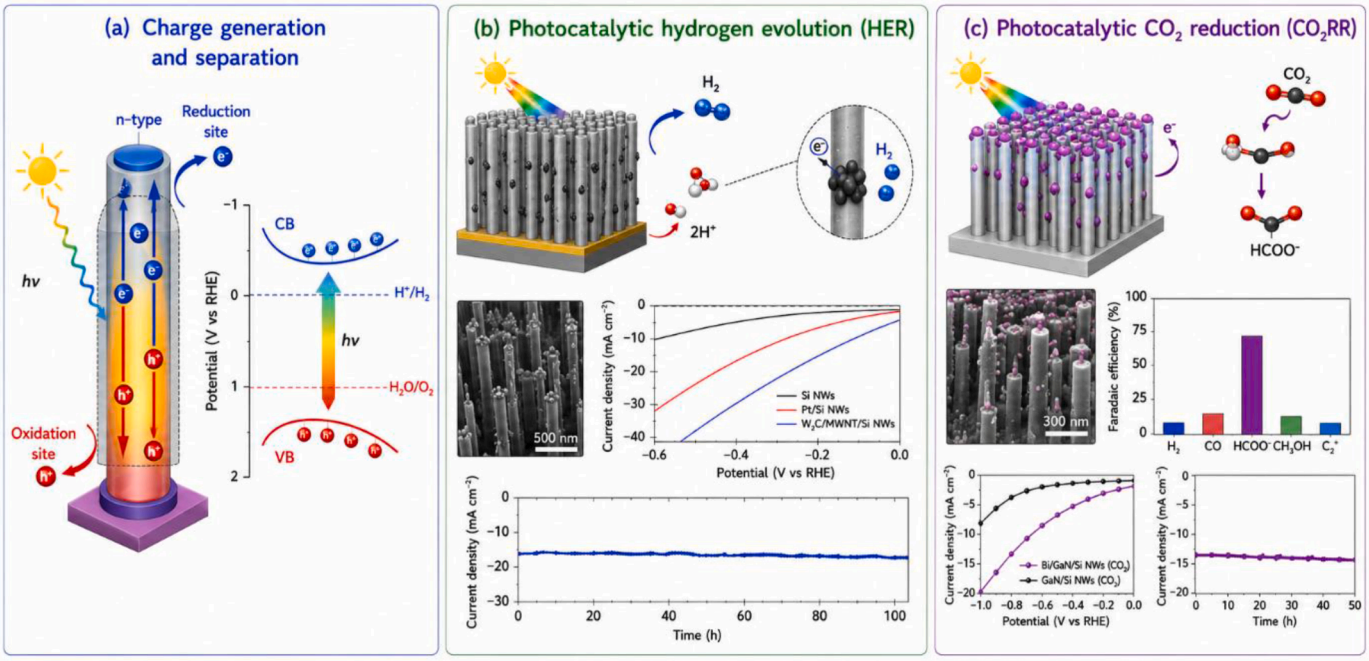


Fig. 10. Photocatalytic hydrogen evolution and CO_2 reduction pathways using semiconductor nanowire photocatalysts. Representative examples illustrate (a) light-induced carrier generation, separation, and transport in semiconductor NWs, (b) solar-driven hydrogen evolution using catalyst-decorated Si NWs, and (c) CO_2 reduction to formate using Bi-decorated GaN/Si nanowire photocathodes. Panels are adapted from Chowdhury et al. [270], Gong et al. [278], and Pan et al. [279], respectively, under the Creative Commons Attribution 4.0 International License (CC BY 4.0). Changes include cropping, resizing, relabeling, and integration into the present composite figure.

holes drive complementary oxidation reactions.

The reduction process involves multi-electron, proton-coupled pathways that yield products such as CO, CH_4, CH_3OH, and HCOOH, depending on catalyst composition and operating conditions. Semiconductor NWs enhance CO_2 conversion by offering large surface areas, efficient charge separation, and short carrier transport distances. Materials such as Si, GaN, Cu_2O, and InP demonstrate strong performance due to favorable band-edge alignment and carrier mobility [288–290].

System performance is typically evaluated using Faradaic efficiency, product selectivity, photocurrent density, and operational stability. Advances in heterostructure design, cocatalyst integration (e.g., Cu, Ag, Au), and defect engineering have significantly improved conversion efficiency and selectivity, positioning NW-based systems as promising platforms for artificial photosynthesis and carbon-neutral fuel production [155,256,282,291,292]. As shown in Fig. 10(c), CO_2 molecules adsorb onto active sites and undergo sequential reduction reactions, with NW architectures enhancing light harvesting, carrier transport, and catalytic activity.

4.6. Lithium-ion batteries

Inorganic semiconductor NWs are promising electrode materials for LIBs (LIBs) due to their ability to provide short Li^+ diffusion pathways, large electrode–electrolyte interfaces, and effective accommodation of volume changes during cycling. The fundamental lithiation/delithiation reaction is expressed as:

$$\mathrm{Host} + x\mathrm{Li}^+ + xe^- \rightleftharpoons \mathrm{Li}_x\mathrm{Host} \quad (29)$$

where *Host* represents the active electrode material.

Battery performance is evaluated based on specific capacity, cycling stability, Coulombic efficiency, and rate capability. Silicon NWs offer an exceptionally high theoretical capacity (~4200 $mAhg^{-1}$), though they suffer from significant volume expansion during cycling [293,294]. SnO_2 NWs provide a capacity of ~782 $mAhg^{-1}$ through combined conversion and alloying mechanisms [295], while TiO_2 NWs exhibit excellent structural stability and long cycle life despite a lower capacity (~335 mAh g^{-1}) [293,296,297].

Recent developments, including core–shell NW designs, carbon coating, and heterostructure engineering, have improved conductivity, mechanical stability, and reversible capacity. As illustrated in Fig. 11, vertically aligned NW electrodes facilitate efficient lithiation/delithiation processes and enhance electrochemical performance. Their intrinsic advantages—such as rapid ion diffusion, efficient electron transport, and high surface area—make semiconductor NWs strong candidates for next-generation high-energy-density storage systems.

4.7. Sodium-ion batteries

SIBs are increasingly recognized as viable alternatives to lithium-ion systems for large-scale energy storage, primarily due to the abundance, low cost, and widespread availability of sodium resources. Similar to LIBs, charge storage is governed by the reversible insertion and extraction of Na^+ ions within host electrode materials. However, the larger ionic radius of Na^+ (1.02 Å) compared to Li^+ (0.76 Å) leads to slower diffusion kinetics and greater structural stress during cycling, necessitating electrode materials with open frameworks and strong mechanical stability [256,300].

Fig. 11 illustrates the sodiation/desodiation process ($Na^+ + e^- + \mathrm{Host} \rightleftharpoons \mathrm{NaHost}$), along with representative electrode materials such as $NaTi_2(PO_4)_3$, TiO_2, Fe_2O_3, and SnO_2 [301,302]. NW architectures play a critical role in accommodating the larger Na^+ ions, improving structural integrity, and enhancing rate performance and cycling stability.

Semiconductor NWs offer distinct advantages for sodium storage, including high surface area, short ion diffusion lengths, and efficient electron transport. $NaTi_2(PO_4)_3$ NWs, featuring a NASICON-type framework, enable fast Na^+ transport and stable cycling with theoretical capacities near 133 $mAhg^{-1}$ [23,301]. TiO_2 NWs exhibit excellent structural durability and long cycle life, although their capacity is typically limited to 150–200 $mAhg^{-1}$ [301]. In contrast, Fe_2O_3 NWs

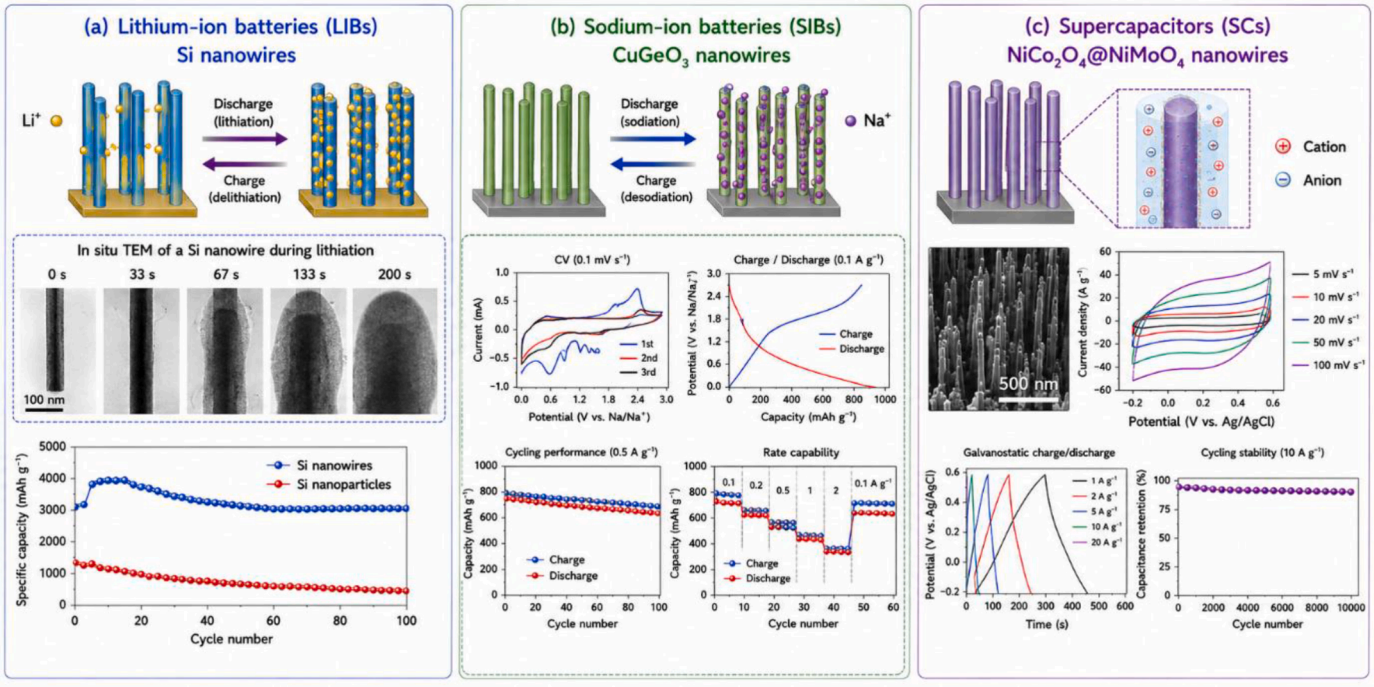


Fig. 11. Semiconductor nanowire architectures for electrochemical energy storage. Representative examples illustrate (a) lithiation and structural evolution of Si NWs for lithium-ion storage, (b) reversible sodium storage and electrochemical performance of $CuGeO_3$ NWs, and (c) hierarchical $NiCo_2O_4$@$NiMoO_4$ nanowire electrodes for high-rate supercapacitive storage. Panels are adapted from Shen et al. [191], Fu et al. [298], and Huang et al. [299], respectively, under the Creative Commons Attribution 4.0 International License (CC BY 4.0). Changes include cropping, resizing, relabeling, and integration into the present composite figure.

provide much higher theoretical capacity (~1007 $mAhg^{-1}$) via conversion reactions but suffer from significant volume changes during cycling [256,303]. Recent strategies such as carbon coating, heterostructure formation, and composite NW design have improved conductivity, capacity retention, and long-term stability, reinforcing the potential of NW-based electrodes for cost-effective sodium-ion storage [301].

4.8. Supercapacitors

Semiconductor NWs have also gained attention as electrode materials for supercapacitors, where their one-dimensional morphology enables large electrochemically active surface areas, rapid electron transport, and short ion diffusion paths, resulting in high power density and excellent cycling durability [304]. The performance of SCs is typically evaluated using specific capacitance, along with energy density and rate capability.

Among NW-based materials, MnO_2 exhibits a high theoretical pseudocapacitance (~1370 Fg^{-1}) [153], $NiCo_2O_4$ offers high electrical conductivity and specific capacitance exceeding 1000 Fg^{-1} [305], and ZnO NWs provide structural stability and serve as effective scaffolds for composite electrodes [303,304]. Advances in hierarchical NW arrays, carbon-integrated hybrids, and core–shell structures have significantly improved electrochemical performance, including capacitance retention and cycling stability [306].

Fig. 11 also illustrates NW-based supercapacitors, highlighting both electric double-layer and pseudocapacitive charge storage mechanisms using materials such as MnO_2, $NiCo_2O_4$, ZnO, and TiO_2. Rapid ion adsorption/desorption, high power delivery, and reversible charge storage are key features of these systems. Additionally, Fig. 11 emphasizes the broader advantages of NW architectures, including reduced ion diffusion distances, increased active surface area, improved mechanical robustness during repeated cycling, and compatibility with scalable electrode fabrication. These attributes position semiconductor NWs as strong candidates for next-generation rechargeable batteries and high-performance supercapacitors.

4.9. Thermoelectric devices

Semiconductor NWs have gained significant interest for thermoelectric applications, where heat is directly converted into electricity via the Seebeck effect. Their one-dimensional structure enhances performance by intensifying phonon scattering at surfaces and interfaces, which lowers thermal conductivity while preserving effective electrical transport [158–160]. Thermoelectric efficiency is quantified by the dimensionless figure of merit, *ZT*, which depends on the Seebeck coefficient, electrical conductivity, temperature, and thermal conductivity; higher *ZT* values correspond to improved energy conversion efficiency.

Among NW materials, Bi_2Te_3 remains the leading candidate for near-room-temperature operation due to its high Seebeck coefficient and intrinsically low thermal conductivity. Silicon NWs exhibit significantly reduced thermal conductivity compared to bulk silicon as a result of enhanced phonon-boundary scattering, achieving *ZT* values in the range of 0.6–1.0 at elevated temperatures [159,307]. PbTe NWs demonstrate *ZT* values exceeding 1 at high temperatures, making them suitable for waste-heat recovery in industrial systems [308,309]. Ongoing advances in alloying, defect engineering, and core–shell NW structures continue to improve thermoelectric performance, supporting the development of efficient and sustainable energy-harvesting devices [310].

4.10. Flexible and wearable energy devices

Semiconductor NWs are also increasingly utilized in flexible and wearable energy systems due to their mechanical compliance, high electrical conductivity, and compatibility with low-temperature processing techniques [311,312]. When integrated onto flexible substrates such as polyethylene terephthalate (PET), polyimide (PI), polydimethylsiloxane (PDMS), or textile fibers, NW networks can tolerate repeated mechanical deformation while maintaining stable electrical properties [313,314].

Materials such as Si, ZnO, Ag-coated semiconductor NWs, and III–V NW arrays enable reliable charge transport under bending and stretching conditions, making them well suited for flexible electronics. These NW-based systems have been widely applied in wearable biosensors, flexible PVs, triboelectric and piezoelectric nanogenerators, and self-powered devices for health monitoring, environmental sensing, and portable energy harvesting 59,188]. Recent progress in heterostructure design, stretchable encapsulation, and printable fabrication methods has further enhanced mechanical durability, energy conversion efficiency, and long-term stability, accelerating the transition toward practical wearable technologies [312,313,315,316].

For clarity, the major applications of inorganic semiconductor NWs in green energy systems—including representative materials, operating mechanisms, key performance indicators, advantages, and existing challenges—are summarized in Table 4.

Comparison across energy applications reveals a recurring principle: the same nanoscale feature that improves an intrinsic performance metric can accelerate a competing loss mechanism [296,321]. High surface area increases catalytic and electrochemical accessibility but also increases the density of surface states, parasitic reactions, and chemically vulnerable interfaces [296,321]. Short radial carrier-collection distances reduce bulk recombination in photovoltaic and photoelectrochemical architectures, yet require highly conformal junctions and passivation to prevent surface recombination from becoming dominant [321]. Similarly, short ion-diffusion distances improve rate capability in battery electrodes, but increased electrode–electrolyte contact can intensify solid-electrolyte-interphase formation and irreversible reactions [296]. Consequently, reported improvements in photocurrent, capacity, catalytic rate, or thermoelectric response should be interpreted together with stability, loading, geometry, contact architecture, and operating conditions rather than as isolated indicators of technological superiority [296,321].

4.11. Device integration and translation challenges

Translation from high-performing individual NWs to practical devices remains a major bottleneck [109,322]. At the single-nanowire level, contact resistance, Schottky barriers, surface contamination, and contact-induced strain can dominate measured transport [323]. At the array and module levels, additional variability arises from nanowire diameter, length, orientation, density, junction depth, doping activation, interface quality, and local contact area. Consequently, ensemble performance can be substantially lower than the properties inferred from isolated NWs [109,322].

Large-area integration requires reproducible alignment or vertical registration, low-resistance contacts, substrate-compatible processing, robust interconnects, and encapsulation without damaging the nanowire surface or altering band alignment. For photovoltaic and photoelectrochemical devices, parasitic optical absorption, series resistance, electrolyte sealing, bubble management, and corrosion protection become system-level constraints. For batteries and supercapacitors, binder/current-collector interfaces, electrode loading, electrolyte accessibility, and mechanical adhesion determine whether nanoscale transport advantages survive at practical areal capacities [296,324]. Flexible systems add cyclic fatigue, delamination, and packaging requirements, whereas thermoelectric modules require low-resistance thermal and electrical contacts [20].

These considerations show that device integration must be treated as a co-design problem. Nanowire composition and morphology should be optimized together with contact metallurgy, substrate, encapsulation, thermal management, manufacturability, yield, and reliability. Future studies should therefore report not only intrinsic nanowire metrics but

Table 4
Green-energy applications, performance indicators, challenges, and relative technology readiness of representative inorganic semiconductor NWs.

Green-energy application	Representative NW materials	Working principle	Key performance indicators	Major advantages	Current challenges	Technology-readiness level*	Refs.
Photovoltaics (PV)	Si, GaAs, InP, CdTe	Photon absorption and radial p–n junction charge separation	PCE: 13–19% (NW); >34% (Si–perovskite tandem)	Superior light trapping; short carrier-diffusion distance; reduced reflection; high carrier-collection efficiency	Surface recombination; fabrication cost; large-area integration	Level 4 — Advanced	[48, 259, 317]
PEC water splitting	TiO_2, Fe_2O_3, $BiVO_4$, ZnO, GaN	Solar-driven water splitting	Photocurrent: >8 mA cm^{-2}; STH: ≈10% or higher	High surface area; efficient charge separation; rapid carrier transport	Photocorrosion; slow OER kinetics; long-term stability	Level 3 — Intermediate–advanced	[72, 318, 319]
Hydrogen evolution reaction (HER)	MoS_2, CoP, NiO, Pt-coated Si	Electrocatalytic proton reduction	Overpotential: <100 mV; Tafel slope: <60 mVdec^{-1}	High catalytic activity; abundant active sites; fast electron transfer	Noble-metal dependence; catalyst durability	Level 4 — Advanced	[281, 320]
Photocatalysis	TiO_2, ZnO, WO_3, CdS, GaN	Photogenerated oxidation–reduction reactions	High degradation efficiency; enhanced H_2 evolution	Large active surface; efficient charge separation; strong redox capability	Limited visible-light response; photocorrosion	Level 2 — Intermediate	[283, 284]
CO_2 reduction	Si, GaN, Cu_2O, InP	Multi-electron CO_2 photoreduction	Faradaic efficiency: >80% (selected systems)	Improved CO_2 adsorption; high selectivity; efficient electron transport	Product selectivity; competing HER; catalyst stability	Level 2 — Intermediate	[155, 290]
Lithium-ion batteries (LIBs)	Si, SnO_2, TiO_2	Reversible lithiation/ delithiation	Si: 4200 $mAhg^{-1}$; SnO_2: 782 $mAhg^{-1}$; TiO_2: 335 mAh g^{-1}	High capacity; short Li^+ diffusion path; improved cycling	Volume expansion; conductivity loss	Level 4 — Advanced	[153, 293, 305]
Sodium-ion batteries (SIBs)	$NaTi_2(PO_4)_3$, TiO_2, Fe_2O_3	Reversible Na^+ insertion/extraction	$NaTi_2(PO_4)_3$: 133 $mAhg^{-1}$	Low cost; excellent structural stability; rapid Na^+ transport	Slow Na^+ diffusion; structural strain	Level 3 — Intermediate–advanced	[301, 302]
Supercapacitors (SCs)	MnO_2, $NiCo_2O_4$, ZnO	Electric double-layer and pseudocapacitive storage	Specific capacitance: >1000 Fg^{-1}; MnO_2 theoretical: 1370 Fg^{-1}	High power density; rapid charging; long cycle life	Low energy density; electrode degradation	Level 4 — Advanced	[153, 304, 305]
Thermoelectric devices	Bi_2Te_3, Si, PbTe	Seebeck effect (heat-to-electricity conversion)	ZT ≈ 0.6–1.5	Reduced thermal conductivity; enhanced phonon scattering	Material toxicity; fabrication complexity	Level 2 — Intermediate	[158, 160, 309]
Flexible and wearable energy devices	Si, ZnO, GaN, Ag-coated NWs	Flexible energy harvesting and storage	Stable performance after >1000 bending cycles	Lightweight; flexible; wearable; multifunctional	Mechanical durability; encapsulation; scalable manufacturing	Level 4 — Advanced	[311, 315, 316]

also device area, active-material loading, contact scheme, fabrication yield, stability, and performance dispersion across statistically meaningful device populations [324]. Thus, the technologically relevant optimization target is not the highest-performing isolated NW, but the architecture that retains sufficient nanoscale functionality after statistically variable NW populations are contacted, packaged, operated, and manufactured at scale [263,296].

4.12. Device integration and translation challenges

Translation from high-performing individual NWs to practical devices remains a major bottleneck [109,322]. At the single-nanowire level, contact resistance, Schottky barriers, surface contamination, and contact-induced strain can dominate measured transport [323]. At the array and module levels, additional variability arises from nanowire diameter, length, orientation, density, junction depth, doping activation, interface quality, and local contact area. Consequently, ensemble performance can be substantially lower than the properties inferred from isolated NWs [109,322].

Large-area integration requires reproducible alignment or vertical registration, low-resistance contacts, substrate-compatible processing, robust interconnects, and encapsulation without damaging the nanowire surface or altering band alignment. For photovoltaic and photoelectrochemical devices, parasitic optical absorption, series resistance, electrolyte sealing, bubble management, and corrosion protection become system-level constraints. For batteries and supercapacitors, binder/current-collector interfaces, electrode loading, electrolyte accessibility, and mechanical adhesion determine whether nanoscale transport advantages survive at practical areal capacities [296,324]. Flexible systems add cyclic fatigue, delamination, and packaging requirements, whereas thermoelectric modules require low-resistance thermal and electrical contacts [20].

These considerations show that device integration must be treated as a co-design problem. Nanowire composition and morphology should be optimized together with contact metallurgy, substrate, encapsulation, thermal management, manufacturability, yield, and reliability. Future studies should therefore report not only intrinsic nanowire metrics but also device area, active-material loading, contact scheme, fabrication yield, stability, and performance dispersion across statistically meaningful device populations [324].

5. Future directions: toward autonomous semiconductor NW engineering

5.1. From materials discovery to autonomous materials engineering

Despite this potential, autonomous nanowire discovery remains constrained by several nontrivial barriers that are common to emerging self-driving laboratories (SDLs) for materials research [325,326]. First, materials datasets available for machine learning are often limited,

heterogeneous, and incomplete, while experimental metadata, unsuccessful experiments, and detailed processing histories are not consistently captured or reported [327,328]. This limitation is particularly consequential for nanowire synthesis, where relationships among precursor chemistry, catalyst state, substrate preparation, temperature, pressure, growth history, morphology, and resulting properties can be highly process-specific. Inadequate metadata and inconsistent data-management practices can therefore restrict reproducibility, model training, and reuse of experimental knowledge across autonomous platforms [328].

Second, differences in reactor configuration, precursor delivery, catalyst history, substrate preparation, equipment calibration, and characterization protocols can generate substantial experimental variability and domain shifts, thereby limiting the transferability of models and optimization policies between laboratories [325,326,329]. Autonomous workflows also require interoperable hardware, software, data infrastructure, and machine-readable experimental protocols; however, current laboratory ecosystems frequently comprise heterogeneous instruments and software environments that were not originally designed for closed-loop communication [325,327,328]. Reproducibility, reconfigurability, modularity, and interoperability must therefore become explicit design requirements for autonomous materials laboratories rather than secondary considerations [329,330].

Third, uncertainty arising from experimental noise, measurement precision, simulations, and surrogate models must be quantified and propagated through the decision-making loop [175,329]. This is particularly important for Bayesian optimization, active learning, and related sequential-design strategies because an autonomous system can otherwise direct experiments toward regions favored by model uncertainty or experimental artifacts rather than toward physically robust materials and processing conditions. Indeed, experimental precision, accessible parameter space, operational lifetime, optimization efficiency, and model validation have been identified as critical performance metrics for assessing the reliability of SDLs [175]. Robust autonomous discovery therefore requires not only predictive accuracy but also uncertainty-aware decision making, appropriate benchmarking, and mechanisms for detecting anomalous or out-of-domain experimental conditions [175,329].

Finally, physical automation introduces practical constraints involving hardware reliability, maintenance, contamination, calibration drift, safety interlocks, exception handling, material consumption, operational cost, and integration of human expertise [325,326,330]. Full laboratory autonomy should therefore not be viewed simply as the elimination of human participation. Recent perspectives instead emphasize human-in-the-loop approaches in which researchers retain responsibility for defining scientific objectives, interpreting unexpected phenomena, supervising safety-critical operations, and revising experimental strategies while AI and robotics perform repetitive experimentation, data analysis, and optimization [329,330]. Furthermore, current SDLs span different levels of autonomy, from algorithm-guided and semi-closed-loop experimentation to fully closed-loop platforms, while genuinely self-motivated systems capable of independently defining scientific objectives remain aspirational [7]. Consequently, near-term autonomous nanowire research is more realistically envisioned as human-supervised, uncertainty-aware closed-loop experimentation with progressively increasing levels of autonomy, rather than fully independent materials discovery [175,329,330].

5.2. Operando and multimodal characterization

Future advances in semiconductor NW engineering could enable increasingly rely on operando and multimodal characterization, where structural, chemical, electronic, and electrochemical processes are monitored in real time under realistic operating conditions rather than through conventional post-mortem analysis. Recent developments in operando TEM, synchrotron XRD, Raman spectroscopy, XPS, 4D scanning transmission electron microscopy (4D-STEM), atom probe tomography (APT), and correlative microscopy enable simultaneous observation of defect evolution, interface reconstruction, phase transformations, ion diffusion, charge separation, and catalyst degradation with nanometer-to-atomic spatial resolution [185,203,221]. Time-resolved characterization further reveals transient structural and electronic processes governing carrier transport and reaction kinetics during device operation [250]. Integrating these complementary techniques with computational modeling and AI-assisted data fusion enables direct correlation between dynamic microstructural evolution and functional performance. Such multimodal experimental ecosystems could enable provide the mechanistic understanding required to validate predictive simulations, accelerate inverse materials design, and establish continuously learning digital twins for autonomous semiconductor NW engineering.

5.3. Physics-informed artificial intelligence

AI is poised to transform semiconductor NW engineering; however, future progress could enable depend on integrating physical principles into data-driven models rather than relying solely on conventional ML. Unlike purely statistical approaches, physics-informed neural networks (PINNs) embed governing differential equations, conservation laws, and boundary conditions directly into the learning process, enabling robust prediction of carrier transport, diffusion, heat transfer, and electrochemical phenomena from limited experimental data [331,332]. Likewise, graph neural networks (GNNs) naturally represent atomic structures as interconnected graphs, allowing accurate prediction of crystal stability, defect energetics, and electronic properties while preserving chemical topology [333]. Recent developments in scientific ML, Bayesian optimization, generative AI, and foundation models have further expanded the capability to perform inverse materials design, autonomous hypothesis generation, and uncertainty-aware optimization across vast chemical spaces [334,335]. Equally important, explainable AI (XAI) and uncertainty quantification provide interpretable predictions and confidence estimates, facilitating reliable decision-making and accelerating experimental validation [336]. Consequently, the future of semiconductor NW research lies in physics-guided AI ecosystems, where experimental observations, computational simulations, and mechanistic understanding are continuously integrated into self-improving models that enhance prediction accuracy while preserving scientific interpretability rather than replacing established physical theories.

5.4. Digital twins for semiconductor NWs

Digital twin technology is emerging as a transformative framework for semiconductor NW research by establishing a continuously synchronized virtual representation of physical materials, devices, and manufacturing processes. Unlike conventional computational models, digital twins integrate real-time experimental measurements, multimodal characterization, physics-based simulations, manufacturing data, and device operating conditions into adaptive predictive models that evolve throughout the material lifecycle [337,338]. For semiconductor NWs, this framework enables continuous updating of structural, chemical, electronic, and electrochemical states using inputs from operando microscopy, spectroscopy, electrical characterization, and computational simulations. Such dynamic synchronization supports predictive degradation analysis, device optimization, remaining lifetime prediction, autonomous diagnostics, and intelligent manufacturing by continuously comparing measured behavior with simulated responses [339]. Coupling digital twins with AI, high-performance computing, and autonomous experimentation further enables closed-loop optimization in which predictive models recommend new synthesis conditions or operating parameters, while subsequent experiments refine the virtual model. Building upon the multimodal characterization framework

described in Section 3, digital twins provide the computational infrastructure required for real-time decision-making and autonomous semiconductor NW engineering, significantly accelerating materials discovery, improving device reliability, and reducing experimental cost.

5.5. Sustainable and scalable manufacturing

The environmental burden of nanowire manufacturing depends strongly on the synthesis route, material system, process energy demand, precursor chemistry, and production yield [340,341]. Vapor-phase methods such as CVD, MOCVD, MBE, and VLS growth can provide high crystallinity, precise dimensional control, and well-defined interfaces, but their environmental performance can be adversely affected by elevated processing temperatures, vacuum infrastructure, carrier-gas consumption, low precursor-utilization efficiencies, and energy-intensive supporting equipment [340,342]. In contrast, wet-chemical, hydrothermal, solvothermal, and electrodeposition routes can operate under comparatively moderate thermal conditions, although their overall sustainability remains sensitive to solvent toxicity, precursor chemistry, water consumption, purification requirements, reaction yield, and waste treatment [341,343]. A recent cradle-to-gate comparison of hydrothermal ZnO nanowire synthesis routes, for example, demonstrated that changes in reagent selection and processing conditions can substantially alter the environmental footprint of nominally similar nanowire products [341]. Catalyst-assisted synthesis introduces additional considerations because catalyst materials and residual contaminants may affect resource consumption, purification requirements, and subsequent device processing. Consequently, scalable nanowire synthesis should be assessed using functionally relevant indicators such as energy consumption per unit of functional material or device area, precursor utilization, solvent and water intensity, material yield, hazardous-input requirements, and waste generation rather than production throughput alone [340,341,343].

End-of-life management is particularly challenging for nanowire-enabled devices because the active nanowire material typically constitutes only one component of a heterogeneous architecture containing substrates, transparent conductors, polymer binders, encapsulants, catalysts, electrolytes, and metallic contacts. Such multi-material integration can complicate physical separation and selective recovery and can result in valuable or critical elements being diluted, contaminated, or lost during conventional recycling operations [344,345]. Similar challenges are already evident in photovoltaic modules, energy-storage systems, and electronic products, where intimate combinations of metals, semiconductors, polymers, ceramics, and adhesives can require sequential mechanical, thermal, hydrometallurgical, and electrochemical treatments for material recovery [344]. Design-for-disassembly, detachable interfaces, substrate reuse, recoverable catalyst systems, and recycling-compatible material combinations should therefore be considered during device development rather than only at end of life [344,345]. For battery, catalytic, and electrode architectures, regeneration, refurbishment, or direct reuse of a structurally intact nanowire scaffold may in some cases preserve more functional value than complete decomposition to elemental feedstocks, consistent with circular-design approaches that prioritize retention of product and material functionality [344,345].

Life-cycle assessment (LCA), techno-economic analysis (TEA), and safe-and-sustainable-by-design (SSbD) principles should therefore be incorporated into nanowire development at an early stage rather than being applied only after materials and processing routes have been fixed [340,343,346]. Recent sustainability frameworks for nanomaterials explicitly demonstrate the value of combining environmental assessment, economic analysis, green-chemistry principles, and process-design metrics to identify pathways that simultaneously reduce environmental burdens and production costs [343]. Likewise, SSbD frameworks emphasize iterative consideration of material efficiency, hazardous-substance minimization, resource use, safety, circularity, and life-cycle impacts during the design and scale-up of advanced materials [346]. Such assessments should account for electricity mix, precursor production, reactor utilization, process yield, material losses, device lifetime, replacement frequency, resource criticality, and end-of-life scenarios [340,346]. Accordingly, the nanowire architecture that delivers the highest laboratory-scale efficiency may not necessarily provide the lowest life-cycle impact if it depends on scarce or hazardous constituents, high-energy vacuum processing, low manufacturing yield, short operational lifetime, or energy- and reagent-intensive recovery processes [340,343]. The practical objective should therefore shift from single-metric performance maximization toward multi-objective optimization of functionality, manufacturability, economic viability, environmental impact, toxicity, resource criticality, durability, and circularity [343,346].

6. Conclusion

Inorganic semiconductor NWs have evolved from model one-dimensional NWs into a versatile class of functional materials that underpin a broad spectrum of sustainable energy technologies. As demonstrated throughout this review, their exceptional performance originates not from nanoscale dimensions alone, but from the deliberate engineering of composition, crystal structure, electronic band alignment, defects, interfaces, morphology, and device architectures. The integration of these interconnected design strategies has transformed NW research from empirical synthesis toward predictive materials engineering, enabling unprecedented control over charge generation, carrier transport, light management, catalytic activity, ion diffusion, and long-term structural stability across applications including PVs, PEC water splitting, photocatalysis, batteries, supercapacitors, thermoelectrics, sensing, and flexible electronics.

This review has emphasized that high-performance NW systems emerge through the synergistic optimization of structure–composition–property–performance relationships rather than isolated improvements in individual material properties. Advances in DFT, multiscale computational modeling, high-throughput simulations, and data-driven materials design now complement sophisticated synthesis techniques and advanced characterization methods, providing a comprehensive understanding of the atomic-scale mechanisms governing NW functionality. Equally important, the convergence of multimodal characterization, operando microscopy and spectroscopy, AI, and scientific ML is enabling direct correlation between structural evolution and device performance, thereby establishing a new paradigm for rational NW engineering.

Despite remarkable scientific progress, several challenges continue to limit widespread industrial implementation. Achieving reproducible large-scale synthesis, precise control of crystal defects and interfaces, long-term operational stability, environmentally benign manufacturing, and economically viable production remains essential for commercialization. Future advances could enable therefore depend not only on developing higher-performance materials but also on integrating scalable manufacturing, green chemistry, life-cycle assessment, and techno-economic analysis into the design process. Addressing these challenges could enable accelerate the transition of semiconductor NWs from laboratory-scale demonstrations to commercially deployable energy technologies.

Looking forward, semiconductor NW research is entering an era of Intelligent NW Engineering, where advanced synthesis, multimodal characterization, computational materials science, physics-informed AI, digital twins, autonomous laboratories, robotics, and high-performance computing are integrated within continuously learning closed-loop discovery platforms. This emerging ecosystem represents a fundamental shift from conventional sequential experimentation toward autonomous materials discovery, in which experiments, simulations, and AI iteratively improve one another to accelerate innovation. Such a

transformative framework has the potential to dramatically reduce development time and cost while enabling the rational discovery of next-generation semiconductor NWs with unprecedented performance, reliability, and sustainability. Ultimately, this convergence establishes inorganic semiconductor NWs as a cornerstone technology for achieving carbon-neutral energy systems and advancing the future of autonomous materials engineering.

Data availability

Data could enable be made available on request.

CRediT authorship contribution statement

Sunday Temitope Oyinbo: Conceptualization, Data curation, Methodology, Writing – original draft, Writing – review & editing. Hoe-Gil Lee: Conceptualization, Project administration, Supervision, Writing – review & editing. Ismail O. Rotimi: Project administration, Supervision, review & editing. Tien-Chien Jen: Project administration, Review & editing.

Declaration of interests

The authors declare that they have no known competing financial interests or personal relationships that could have appeared to influence the work reported in this paper.

References

[1] R.S. Wagner, W.C. Ellis, Vapor-liquid-solid mechanism of single crystal growth, Appl. Phys. Lett. 4 (1964) 89–90, https://doi.org/10.1063/1.1753975.

[2] Y. Liu, G. Zhu, Vapor-phase growth of single-crystal defect-free nanowires: interface dynamics, morphology control, and emerging applications, Chem. Phys. Rev 6 (2025), https://doi.org/10.1063/5.0281822.

[3] A.M. Morales, C.M. Lieber, A Laser ablation method for the synthesis of crystalline semiconductor nanowires, Science 279 (1998) 208–211, https://doi.org/10.1126/science.279.5348.208.

[4] Z. Xu, H. Tang, W. Luo, Y. Li, Q. Lv, L. Qiu, Q. Tao, S. Ni, C. Wu, Z. Wang, Z. Ye, R. Zhang, N. Zhou, C. Liu, J. Li, M. Liu, X.D. Wang, Z. Liu, L.S. Liao, H. Dong, L. Zhang, J. Li, Single-crystal growth of complex non-fullerene acceptor molecules via cocrystallization, Nat. Commun. 17 (2026), https://doi.org/10.1038/s41467-026-69997-7, 3175-.

[5] J. Hu, T.W. Odom, C.M. Lieber, Chemistry and physics in one dimension: synthesis and properties of nanowires and nanotubes, Acc. Chem. Res. 32 (1999) 435–445, https://doi.org/10.1021/ar9700365.

[6] C.M. Lieber, Z.L. Wang, Functional nanowires, MRS Bull. 32 (2007) 99–108, https://doi.org/10.1557/mrs2007.41.

[7] P. Yang, Semiconductor nanowire, what's next II? Next Mater. 1 (2023) 100014 https://doi.org/10.1016/j.nxmate.2023.100014.

[8] C.Y. Hsu, A.M. Rheima, Z. sabri Abbas, M.U. Faryad, M.M. Kadhim, U.S. Altimari, A.H. Dawood, A. dhari jawad al-bayati, Z.T. Abed, R.S. Radhi, A.S. Jaber, S. K. Hachim, F.K. Ali, Z.H. Mahmoud, G. Behzadi pour, E. Kianfar, Nanowires properties and applications: a review study, South Afr. J. Chem. Eng. 46 (2023) 286–311, https://doi.org/10.1016/J.SAJCE.2023.08.006.

[9] M. Samykano, Progress in one-dimensional nanostructures, Mater. Charact. 179 (2021), https://doi.org/10.1016/j.matchar.2021.111373.

[10] N.P. Dasgupta, J. Sun, C. Liu, S. Brittman, S.C. Andrews, J. Lim, H. Gao, R. Yan, P. Yang, 25th anniversary article: semiconductor nanowires - synthesis, characterization, and applications, Adv. Mater. 26 (2014) 2137–2184, https://doi.org/10.1002/adma.201305929.

[11] H.J. Joyce, Q. Gao, H.H. Tan, C. Jagadish, Y. Kim, J. Zou, L.M. Smith, H. E. Jackson, J.M. Yarrison-Rice, P. Parkinson, M.B. Johnston, III–V semiconductor nanowires for optoelectronic device applications, Prog. Quant. Electron. 35 (2011) 23–75, https://doi.org/10.1016/j.pquantelec.2011.03.002.

[12] E. Barrigón, M. Heurlin, Z. Bi, B. Monemar, L. Samuelson, Synthesis and applications of III–V nanowires, Chem. Rev. 119 (2019) 9170–9220, https://doi.org/10.1021/acs.chemrev.9b00075.

[13] P. Yang, 30 years of semiconductor nanowire research: a personal journey, Isr. J. Chem. 65 (2025) e202300127, https://doi.org/10.1002/ijch.202300127.

[14] M.A. Fardy, Semiconductor Nanowires and Nanotubes for Energy Conversion, 2010.

[15] E. Garnett, P. Yang, Light trapping in silicon nanowire solar cells, Nano Lett. 10 (2010) 1082–1087, https://doi.org/10.1021/NL100161Z.

[16] B. Tian, X. Zheng, T.J. Kempa, Y. Fang, N. Yu, G. Yu, J. Huang, C.M. Lieber, Coaxial silicon nanowires as solar cells and nanoelectronic power sources, Nature 449 (2009) 885–889, https://doi.org/10.1038/nature06181.

[17] T.J. Kempa, B. Tian, D.R. Kim, J. Hu, X. Zheng, C.M. Lieber, Single and tandem axial p-i-n nanowire photovoltaic devices, Proc. Natl. Acad. Sci. U. S. A. 105 (2008) 11095–11100, https://doi.org/10.1073/pnas.0802959105.

[18] C. Liu, J. Tang, H.M. Chen, B. Liu, P. Yang, A fully integrated nanosystem of semiconductor nanowires for direct solar water splitting, Nano Lett. 13 (2013) 2989–2992, https://doi.org/10.1021/nl401615t.

[19] K. Yu, H. Wang, X. Wang, W. Liang, X. Liang, Y. Zhang, X. Liu, Y. Mai, Nanowires in energy storage devices: structures, synthesis, and applications, Adv. Energy Mater. 8 (2018) 1802369, https://doi.org/10.1002/aenm.201802369.

[20] N.I. Goktas, P. Wilson, A. Ghukasyan, D. Wagner, S. McNamee, R.R. LaPierre, Nanowires for energy: a review, Appl. Phys. Rev. 5 (2018), https://doi.org/10.1063/1.5054842/124236.

[21] Q. Su, J. Ji, W. Wang, W. Ren, Q. An, Coaxial one-dimensional nanowires: artificial interface engineering for next-generation, Energy Storage, Small (2026) e74608, https://doi.org/10.1002/smll.74608.

[22] Y. Xia, P. Yang, Y. Sun, Y. Wu, B. Mayers, B. Gates, Y. Yin, F. Kim, H. Yan, One-dimensional nanostructures: synthesis, characterization, and applications, Adv. Mater. 15 (2003) 353–389, https://doi.org/10.1002/adma.200390087.

[23] M. Nehra, N. Dilbaghi, G. Marrazza, A. Kaushik, R. Abolhassani, Y.K. Mishra, K. H. Kim, S. Kumar, 1D semiconductor nanowires for energy conversion, harvesting and storage applications, Nano Energy 76 (2020), https://doi.org/10.1016/j.nanoen.2020.104991.

[24] H. Hijazi, M. Zeghouane, V.G. Dubrovskii, Thermodynamics of the vapor–liquid–solid growth of ternary III–V nanowires in the presence of silicon, Nanomaterials 11 (2021) 1–8, https://doi.org/10.3390/NANO11010083.

[25] H. Lin, S. Xing, A. Jiang, M. Li, Q. Chen, Z. Wang, L. Jiang, H. Li, J. Wang, C. Zhou, Controlled synthesis of large-area oriented ZnO nanoarrays, Nanomaterials 14 (2024), https://doi.org/10.3390/NANO14121028.

[26] J. Yoon, F. Huang, K.H. Shin, J.I. Sohn, W.K. Hong, Effects of applied voltages on the charge transport properties in a ZnO nanowire field effect transistor, Materials 13 (2020), https://doi.org/10.3390/MA13020268.

[27] M. Kaladzhian, N. von den Driesch, N. Demarina, I. Povstugar, E. Zimmermann, M.M. Jansen, J.H. Bae, C. Krause, B. Bennemann, D. Grützmacher, T. Schäpers, A. Pawlis, Growth and electrical characterization of hybrid core/shell InAs/CdSe nanowires, ACS Appl. Mater. Interfaces 16 (2024) 11035–11042, https://doi.org/10.1021/ACSAMI.3C18267.

[28] L. Ward, A. Agrawal, A. Choudhary, C. Wolverton, A general-purpose machine learning framework for predicting properties of inorganic materials, npj Comput. Mater. 2 (2016), https://doi.org/10.1038/NPJCOMPUMATS.2016.28.

[29] A.G. Kusne, H. Yu, C. Wu, H. Zhang, J. Hattrick-Simpers, B. DeCost, S. Sarker, C. Oses, C. Toher, S. Curtarolo, A.V. Davydov, R. Agarwal, L.A. Bendersky, M. Li, A. Mehta, I. Takeuchi, On-the-fly closed-loop materials discovery via Bayesian active learning, Nat. Commun. 11 (2020) 5966, https://doi.org/10.1038/s41467-020-19597-w.

[30] T. Hanrath, B.A. Korgel, Chemical surface passivation of Ge nanowires, J. Am. Chem. Soc. 126 (2004) 15466–15472, https://doi.org/10.1021/ja0465808.

[31] V.S.E.D. Minot, Y. Yaish, P.L. McEuen, Role of molecular surface passivation in electrical transport properties of InAs nanowires, Nano Lett. 7 (2007) 367–371, https://doi.org/10.1021/nl0629234.

[32] J.B.H.M.O. Demichel, M. Heiss, A.F. i Morral, Y. Dan, K. Seo, K. Takei, J.H. Meza, A. Javey, K.B. Crozier, Dramatic reduction of surface recombination by in situ surface passivation of silicon nanowires, Nano Lett. 11 (2011) 2323–2329, https://doi.org/10.1021/nl201179n.

[33] A.C. Ford, others, Removal of surface states and recovery of band-edge emission in InAs nanowires, Nano Lett. 12 (2012) 1340–1343, https://doi.org/10.1021/nl300015w.

[34] C.-C. Chang, others, Electrical and optical characterization of surface passivation in GaAs nanowires, Nano Lett. 12 (2012) 4484–4489, https://doi.org/10.1021/nl301391h.

[35] Nitride surface passivation of GaAs nanowires: impact on electrical and optical properties, Nano Lett. 14 (2014), https://doi.org/10.1021/nl502909k.

[36] J.L. Boland, S. Conesa-Boj, P. Parkinson, G. Tütüncüoglu, F. Matteini, D. Rüffer, A. Casadei, F. Amaduzzi, F. Jabeen, C.L. Davies, H.J. Joyce, L.M. Herz, A. Fontcuberta I Morral, M.B. Johnston, Modulation doping of GaAs/AlGaAs core-shell nanowires with effective defect passivation and high electron mobility, Nano Lett. 15 (2015) 1336–1342, https://doi.org/10.1021/NL504566T.

[37] Y. Liu, J.V. Knutsson, N. Wilson, E. Young, S. Lehmann, K.A. Dick, C. J. Palmstrøm, A. Mikkelsen, R. Timm, Self-selective formation of ordered 1D and 2D GaBi structures on wurtzite GaAs nanowire surfaces, Nat. Commun. 12 (2021), https://doi.org/10.1038/S41467-021-26148-4.

[38] P. Nukala, C.C. Lin, R. Composto, R. Agarwal, Ultralow-power switching via defect engineering in germanium telluride phase-change memory devices, Nat. Commun. 7 (2016), https://doi.org/10.1038/NCOMMS10482.

[39] G. Liao, N. Luo, K.Q. Chen, H.Q. Xu, Electronic structures of free-standing nanowires made from indirect bandgap semiconductor gallium phosphide, Sci. Rep. 6 (2016), https://doi.org/10.1038/SREP28240.

[40] Z.X. Yang, Y. Yin, J. Sun, L. Bian, N. Han, Z. Zhou, L. Shu, F. Wang, Y. Chen, A. Song, J.C. Ho, Chalcogen passivation: an in-situ method to manipulate the morphology and electrical property of GaAs nanowires, Sci. Rep. 8 (2018), https://doi.org/10.1038/S41598-018-25209-X.

[41] S. Gao, S. Hong, S. Park, H.Y. Jung, W. Liang, Y. Lee, C.W. Ahn, J.Y. Byun, J. Seo, M.G. Hahm, H. Kim, K. Kim, Y. Yi, H. Wang, M. Upmanyu, S.G. Lee, Y. Homma, H. Terrones, Y.J. Jung, Catalyst-free synthesis of sub-5 nm silicon nanowire arrays with massive lattice contraction and wide bandgap, Nat. Commun. 13 (2022), https://doi.org/10.1038/S41467-022-31174-X.

[42] J. Ma, B. Cao, S. Dong, Y. Tian, M. Wang, J. Xiong, S. Sun, MLMD: a programming-free AI platform to predict and design materials, npj Comput. Mater. 10 (2024), https://doi.org/10.1038/S41524-024-01243-4.

[43] S.A. Ahad, T. Kennedy, H. Geaney, {Si} Nanowires: From Model System to Practical {Li}-Ion Anode Material and Beyond, ACS Energy Lett. 9 (2024) 1548–1561, https://doi.org/10.1021/acsenergylett.4c00262.

[44] S. Raman, K.V. Meena, S. Vetrivel, R. Sankar A, Silicon nanowire piezoresistor and its applications: a review, Nanotechnology 35 (2024), https://doi.org/10.1088/1361-6528/ad555e.

[45] C.K. Chan, H. Peng, G. Liu, K. McIlwrath, X.F. Zhang, R.A. Huggins, Y. Cui, High-performance lithium battery anodes using silicon nanowires, Nat. Nanotechnol. 3 (2008) 31–35, https://doi.org/10.1038/nnano.2007.411.

[46] A. Garcia-Gil, S. Biswas, J.D. Holmes, A review of self-seeded germanium nanowires: synthesis, growth mechanisms and potential applications, Nanomaterials 11 (2021) 2002, https://doi.org/10.3390/nano11082002.

[47] I. Gavrilin, I. Marinkin, A. Skundin, T. Kulova, A. Pavlikov, L. Volkova, R. Volkov, N. Borgardt, A. Merkulov, F. Napolskiy, A. Rudnykh, V. Krivchenko, Germanium nanowires as anode material for lithium-ion batteries with ability to charge at subzero temperatures, Batter. \& Supercaps 8 (2025) e202400748, https://doi.org/10.1002/batt.202400748.

[48] A. Mukherjee, D. Ren, P.E. Vullum, J. Huh, B.O. Fimland, H. Weman, GaAs/AlGaAs Nanowire Array Solar Cell Grown on Si with Ultrahigh Power-per-Weight Ratio, ACS Photonics 8 (2021) 2355–2366, https://doi.org/10.1021/ACSPHOTONICS.1C00527.

[49] D. V Prashant, S.K. Agnihotri, S. Bhattarai, R. Pandey, Systematic Investigation of the Optoelectronic Properties of {GaAs} Nanowire and Nanocone Solar Cells: Effect of Geometrical Nonuniformities, Angle of Incidence, and Structural and Electronic Parameters, ACS Appl. Electron. Mater. (2023), https://doi.org/10.1021/acsaelm.3c00657.

[50] L.-Q. Yue, Y.-L. Shi, N.-F. Sun, S. Qiang, J.-K. Qin, L. Zhen, C.-Y. Xu, {InP} Low-Dimensional Nanomaterials for Electronic and Optoelectronic Device Applications: A Review, Adv. Sens. Res. 2 (2023) 2200101, https://doi.org/10.1002/adsr.202200101.

[51] J. Wallentin, N. Anttu, D. Asoli, M. Huffman, I. Åberg, M.H. Magnusson, G. Siefer, P. Fuss-Kailuweit, F. Dimroth, B. Witzigmann, H.Q. Xu, L. Samuelson, K. Deppert, M.T. Borgström, InP nanowire array solar cells achieving 13.8% efficiency by exceeding the ray optics limit, Science (80) 339 (2013) 1057–1060, https://doi.org/10.1126/SCIENCE.1230969.

[52] A. Abdullah, A. Waseem, I. V Bagal, M.A. Johar, M.A. Kulkarni, J.K. Lee, S.-W. Ryu, Stable and Efficient Photoelectrochemical Water Splitting of {GaN} Nanowire Photoanode Coated with {Au} Nanoparticles by Hot-Electron-Assisted Transport, ACS Appl. Energy Mater. 4 (2021) 13759–13765, https://doi.org/10.1021/acsaem.1c02486.

[53] A. Abdullah, I. V Bagal, A. Waseem, M.A. Kulkarni, H. Thaalbi, J.K. Lee, S.-W. Ryu, Engineering {GaN} Nanowire Photoanode Interfaces for Efficient and Stable Photoelectrochemical Water Splitting, Mater. Today Phys. 28 (2022) 100846, https://doi.org/10.1016/j.mtphys.2022.100846.

[54] J. Wang, B. Weng, P. Larson, Y. Liu, Synthesis and characterization of self-assembled ZnO nanoarrays on hybrid structural fibers, Surfaces and Interfaces 16 (2019) 188–193, https://doi.org/10.1016/j.surfin.2018.10.006.

[55] Z.L. Wang, J. Song, Piezoelectric nanogenerators based on zinc oxide nanowire arrays, Science (80) 312 (2006) 242–246, https://doi.org/10.1126/science.1124005.

[56] X. Liu, L. Gu, Q. Zhang, J. Wu, Y. Long, Z. Fan, All-Printable Band-Edge Modulated {ZnO} Nanowire Photodetectors with Ultra-High Detectivity, Nat. Commun. 5 (2014) 4007, https://doi.org/10.1038/ncomms5007.

[57] A. Costas, C. Florica, N. Preda, N. Apostol, A. Kuncser, A. Nitescu, I. Enculescu, Radial Heterojunction Based on Single {ZnO–Cu_{x}O} Core–Shell Nanowire for Photodetector Applications, Sci. Rep. 9 (2019) 5553, https://doi.org/10.1038/s41598-019-42060-w.

[58] Y.J. Hwang, C. Hahn, B. Liu, P. Yang, Photoelectrochemical Properties of {TiO2} Nanowire Arrays: A Study of the Dependence on Length and Atomic Layer Deposition Coating, ACS Nano 6 (2012) 5060–5069, https://doi.org/10.1021/nn300679d.

[59] W.-Q. Wu, B.-X. Lei, H.-S. Rao, Y.-F. Xu, Y.-F. Wang, C.-Y. Su, D.-B. Kuang, Hydrothermal Fabrication of Hierarchically Anatase {TiO2} Nanowire Arrays on {FTO} Glass for Dye-Sensitized Solar Cells, Sci. Rep. 3 (2013) 1352, https://doi.org/10.1038/srep01352.

[60] P.-Y. Hsieh, Y.-H. Chiu, T.-H. Lai, M.-J. Fang, Y.-T. Wang, Y.-J. Hsu, {TiO2} Nanowire-Supported Sulfide Hybrid Photocatalysts for Durable Solar Hydrogen Production, ACS Appl. Mater. \& Interfaces 11 (2019) 3006–3015, https://doi.org/10.1021/acsami.8b17858.

[61] J. Su, X. Feng, J.D. Sloppy, L. Guo, C.A. Grimes, Vertically Aligned {WO3} Nanowire Arrays Grown Directly on Transparent Conducting Oxide Coated Glass: Synthesis and Photoelectrochemical Properties, Nano Lett 11 (2011) 203–208, https://doi.org/10.1021/nl1034573.

[62] Z.-X. Cai, H.-Y. Li, X.-N. Yang, X. Guo, {NO} Sensing by Single Crystalline {WO3} Nanowires, Sensors Actuators B Chem 219 (2015) 346–353, https://doi.org/10.1016/j.snb.2015.05.036.

[63] Y. Ling, G. Wang, D.A. Wheeler, J.Z. Zhang, Y. Li, Sn-Doped hematite nanostructures for photoelectrochemical water splitting, Nano Lett 11 (2011) 2119–2125, https://doi.org/10.1021/nl200708y.

[64] M. Li, Y. Yang, Y. Ling, W. Qiu, F. Wang, T. Liu, Y. Song, X. Liu, P. Fang, Y. Tong, Y. Li, Morphology and doping engineering of Sn-Doped hematite nanowire photoanodes, Nano Lett 17 (2017) 2490–2495, https://doi.org/10.1021/acs.nanolett.7b00184.

[65] L. Li, Z. Lou, G. Shen, Hierarchical {CdS} Nanowires Based Rigid and Flexible Photodetectors with Ultrahigh Sensitivity, ACS Appl. Mater. \& Interfaces 7 (2015) 23507–23514, https://doi.org/10.1021/acsami.5b06070.

[66] S. Guan, X. Fu, Y. Zhang, Z. Peng, β-NiS modified CdS nanowires for photocatalytic H2 evolution with exceptionally high efficiency, Chem. Sci. 9 (2018) 1574–1585, https://doi.org/10.1039/C7SC03928J.

[67] H. Choi, J.G. Radich, P. V Kamat, Sequentially Layered {CdSe/CdS} Nanowire Architecture for Improved Nanowire Solar Cell Performance, J. Phys. Chem. C 118 (2014) 206–213, https://doi.org/10.1021/jp410235s.

[68] A. Kolmakov, D.O. Klenov, Y. Lilach, S. Stemmer, M. Moskovits, Enhanced Gas Sensing by Individual {SnO2} Nanowires and Nanobelts Functionalized with {Pd} Catalyst Particles, Nano Lett 5 (2005) 667–673, https://doi.org/10.1021/nl050082v.

[69] M. Gu, A. Kushima, Y. Shao, J.-G. Zhang, J. Liu, N.D. Browning, J. Li, C. Wang, Probing the Failure Mechanism of {SnO2} Nanowires for Sodium-Ion Batteries, Nano Lett 13 (2013) 5203–5211, https://doi.org/10.1021/nl402633n.

[70] Y. Cao, D. Liu, X. Ni, X. Meng, Y. Zhou, Z. Sun, Y. Kuang, Better Charge Separation in {CuO} Nanowire Array Photocathodes: Micro-/Nanostructure Regulation for Photoelectrochemical Reaction, ACS Appl. Energy Mater. 3 (2020) 6334–6343, https://doi.org/10.1021/acsaem.0c00554.

[71] P.M. Rao, others, Simultaneously efficient light absorption and charge separation in WO3/BiVO4 core/shell nanowire photoanode for photoelectrochemical water oxidation, Nano Lett 14 (2014) 1099–1105, https://doi.org/10.1021/nl500022z.

[72] J. Resasco, H. Zhang, N. Kornienko, N. Becknell, H. Lee, J. Guo, A.L. Briseno, P. Yang, TiO2/BiVO4 nanowire heterostructure photoanodes based on type II band alignment, ACS Cent. Sci. 2 (2016) 80, https://doi.org/10.1021/acscentsci.5b00402.

[73] P. Varadhan, others, Surface passivation of GaN nanowires for enhanced photoelectrochemical water splitting, Nano Lett. 17 (2017) 1520–1528, https://doi.org/10.1021/acs.nanolett.6b04559.

[74] L.E. Black, others, Effective surface passivation of InP nanowires by atomic-layer-deposited Al2O3, Nano Lett. 17 (2017), https://doi.org/10.1021/acs.nanolett.7b02972.

[75] R.J. Theeuwes, J. Melskens, W. Beyer, U. Breuer, L.E. Black, W.J.H. Berghuis, B. Macco, W.M.M. Kessels, POx/Al2O3 stacks for surface passivation of Si and InP, Sol. Energy Mater. Sol. Cells 246 (2022) 111911, https://doi.org/10.1016/J.SOLMAT.2022.111911.

[76] J.Y. Lu, Y.J. Bao, T.Z. Feng, Q. Lv, Y.L. Shi, X.D. Wang, Development and applications of epitaxial heterostructures based on organic nanowires, Chem. Soc. Rev. (2026), https://doi.org/10.1039/D5CS01277E/1276289.

[77] D.W.L.J. Lauhon, M.S. Gudiksen, C.M. Lieber, Epitaxial core-shell and core-multishell nanowire heterostructures, Nature 420 (2002) 57–61, https://doi.org/10.1038/nature01141.

[78] L. Zeng, E. Olsson, Unveiling variations in electronic and atomic structures due to nanoscale wurtzite and zinc blende phase separation in GaAs nanowires, Nano Lett 24 (2024) 6644–6650, https://doi.org/10.1021/ACS.NANOLETT.4C01262.

[79] T. Dursap, M. Vettori, A. Danescu, C. Botella, P. Regreny, G. Patriarche, M. Gendry, J. Penuelas, Crystal phase engineering of self-catalyzed GaAs nanowires using a RHEED diagram, Nanoscale Adv 2 (2020) 2127–2134, https://doi.org/10.1039/D0NA00273A.

[80] X. Li, J. Ni, R. Zhang, A thermodynamic model of Diameter- and temperature-dependent semiconductor nanowire growth, Sci. Rep. 7 (2017), https://doi.org/10.1038/S41598-017-15077-2.

[81] L. Balaghi, others, Widely tunable GaAs bandgap via strain engineering in core/shell nanowires with large lattice mismatch, Nat. Commun. 10 (2019) 2793, https://doi.org/10.1038/s41467-019-10654-7.

[82] S. Martí-Sánchez, M. Botifoll, E. Oksenberg, C. Koch, C. Borja, M.C. Spadaro, V. Di Giulio, Q. Ramasse, F.J. García de Abajo, E. Joselevich, J. Arbiol, Sub-nanometer mapping of strain-induced band structure variations in planar nanowire core-shell heterostructures, Nat. Commun. 13 (2022) 4089, https://doi.org/10.1038/s41467-022-31778-3.

[83] A.S.M.J. Islam, M.S. Hasan, M.S. Islam, A.G. Bhuiyan, C. Stampfl, J. Park, Crystal orientation-dependent tensile mechanical behavior and deformation mechanisms of zinc-blende ZnSe nanowires, Sci. Rep. 13 (2023), https://doi.org/10.1038/S41598-023-30601-3.

[84] H. Liu, X. Zhang, N. Xu, C. Han, N. Wu, B. Wang, Y. Wang, Progress of One-Dimensional {SiC} Nanomaterials: Design, Fabrication and Sensing Applications, Nanomaterials 14 (2024) 187, https://doi.org/10.3390/nano14020187.

[85] M.S. Ram, K.-M. Persson, A. Irish, A. Jönsson, R. Timm, L.-E. Wernersson, High-density logic-in-memory devices using vertical indium arsenide nanowires on silicon, Nat. Electron. 4 (2021) 914–920, https://doi.org/10.1038/s41928-021-00688-5.

[86] A. Abrand, M.A. Baboli, S.M. Hubbard, P.K. Mohseni, Localized Self-Assembly of {InAs} Nanowire Arrays on Reusable {Si} Substrates for Substrate-Free Optoelectronics, ACS Appl. Nano Mater. 5 (2022) 840–851, https://doi.org/10.1021/acsanm.1c03557.

[87] H.J. Joyce, J. Wong-Leung, Q. Gao, H. Hoe Tan, C. Jagadish, Q. Joyce, J. Wong-Leung, C. Jagadish, Phase perfection in zinc blende and wurtzite III-V nanowires using basic growth parameters, Nano Lett 10 (2010) 908–915, https://doi.org/10.1021/nl903688v.

[88] T. Dursap, M. Vettori, C. Botella, P. Regreny, N. Blanchard, M. Gendry, N. Chauvin, M. Bugnet, A. Danescu, J. Penuelas, Wurtzite phase control for self-assisted GaAs nanowires grown by molecular beam epitaxy, Nanotechnology 32 (2021), https://doi.org/10.1088/1361-6528/ABDA75.

[89] R. Rurali, Structural, electronic, and transport properties of silicon nanowires, Rev. Mod. Phys. 82 (2010) 427–449, https://doi.org/10.1103/RevModPhys.82.427.
[90] X. Zhao, C.M. Wei, L. Yang, M.Y. Chou, Quantum confinement and electronic properties of silicon nanowires, Phys. Rev. Lett. 92 (2004), https://doi.org/10.1103/PHYSREVLETT.92.236805.
[91] M. Dimitrievska, others, The advantage of nanowire configuration in band-structure engineering, Adv. Funct. Mater. 31 (2021) 2105426, https://doi.org/10.1002/adfm.202105426.
[92] X. Zhang, F. Zhang, R. Yi, N. Wang, Z. Su, M. Zhang, B. Zhao, Z. Li, J. Qu, J. M. Cairney, Y. Lu, J. Zhao, X. Gan, H.H. Tan, C. Jagadish, L. Fu, Telecom-band multiwavelength vertical emitting quantum well nanowire laser arrays, Light Sci. Appl. 13 (2024), https://doi.org/10.1038/S41377-024-01570-7.
[93] N. Luo, G.Y. Huang, G. Liao, L.H. Ye, H.Q. Xu, Band-inverted gaps in InAs/GaSb and GaSb/InAs core-shell nanowires, Sci. Rep. 6 (2016), https://doi.org/10.1038/SREP38698.
[94] G. Liao, N. Luo, K.Q. Chen, H.Q. Xu, Electronic structures of [1 1 1]-oriented free-standing InAs and InP nanowires, J. Phys. Condens. Matter 28 (2016) 135303, https://doi.org/10.1088/0953-8984/28/13/135303.
[95] B.S.P.W. Leu, K. Cho, Surface chemical control of the electronic structure of silicon nanowires: density functional calculations, Phys. Rev. B 73 (2006) 195320, https://doi.org/10.1103/PhysRevB.73.195320.
[96] M. Nolan, S. O'Callaghan, G. Fagas, J.C. Greer, T. Frauenheim, Silicon nanowire band gap modification, Nano Lett 7 (2007) 34–38, https://doi.org/10.1021/NL061888D.
[97] M. Amato, M. Palummo, S. Ossicini, Band structure analysis in SiGe nanowires, Mater. Sci. Eng. B 177 (2012) 705–711, https://doi.org/10.1016/J.MSEB.2011.10.008.
[98] Composition-graded ZnxCd1-xSe@ZnO core-shell nanowire arrays for photoelectrochemical hydrogen generation, J. Phys. Chem. C (2011), https://doi.org/10.1021/jp204747w.
[99] S. Corby, L. Francàs, A. Kafizas, J.R. Durrant, Determining the role of oxygen vacancies in the photoelectrocatalytic performance of WO3 for water oxidation, Chem. Sci. 11 (2020) 2907–2914, https://doi.org/10.1039/C9SC06325K.
[100] S.F. Duan, Y.F. Ji, W. Wang, D.F. Han, H.Y. Wang, Q.Y. Wei, C.F. Li, F. Jia, D. X. Han, L. Niu, D.D. Qin, C.L. Tao, Unraveling the impact of electrochemically created oxygen vacancies on the performance of ZnO nanowire photoanodes, ACS Sustain. Chem. Eng. 7 (2019) 18165–18173, https://doi.org/10.1021/ACSSUSCHEMENG.9B05442.
[101] L. Hou, M. Zhang, Z. Guan, Q. Li, J. Yang, Effect of annealing ambience on the formation of surface/bulk oxygen vacancies in TiO 2 for photocatalytic hydrogen evolution, Appl. Surf. Sci. 428 (2018) 640–647, https://doi.org/10.1016/j.apsusc.2017.09.144.
[102] L. Hou, Z. Guan, M. Zhang, C. He, Q. Li, J. Yang, Adjusting the ratio of bulk single-electron-trapped oxygen vacancies/surface oxygen vacancies in TiO2 for efficient photocatalytic hydrogen evolution, Catal. Sci. Technol. 8 (2018) 2809–2817, https://doi.org/10.1039/C8CY00644J.
[103] K. Zekentes, J. Choi, V. Stambouli, E. Bano, O. Karker, K. Rogdakis, Progress in {SiC} Nanowire Field-Effect-Transistors for Integrated Circuits and Sensing Applications, Microelectron. Eng. 255 (2022) 111704, https://doi.org/10.1016/j.mee.2021.111704.
[104] G. Badawy, E.P.A.M. Bakkers, Electronic transport and quantum phenomena in nanowires, Chem. Rev. 124 (2024) 2419–2440, https://doi.org/10.1021/ACS.CHEMREV.3C00656.
[105] F. Shang, C. Zha, H. Zhu, Z. Zhang, Y. Shen, Q. Hou, L. Zhang, Y. Chu, L. Chen, J. Zhao, W. Fang, Y. Zhang, Z. Cheng, Y. Zhang, Effective surface passivation of GaAs nanowire photodetectors by a thin ZnO capping, Nanoscale 16 (2024) 12534–12540, https://doi.org/10.1039/D4NR01022A.
[106] X. Yan, Y. Liu, C. Zha, X. Zhang, Y. Zhang, X. Ren, Non-⟨111⟩-oriented semiconductor nanowires: growth, properties, and applications, Nanoscale 15 (2023) 3032–3050, https://doi.org/10.1039/D2NR06421A.
[107] M. Amato, R. Rurali, Surface physics of semiconducting nanowires, Prog. Surf. Sci. 91 (2016) 1–28, https://doi.org/10.1016/J.PROGSURF.2015.11.001.
[108] D. Ma, J. Chen, J. Li, X. Ji, J.W. Shi, A review on passivation engineering for improving photocatalytic hydrogen evolution performance, J. Mater. Chem. A 12 (2024) 12293–12324, https://doi.org/10.1039/D4TA00411F.
[109] Z. Li, Z. He, C. Xi, F. Zhang, L. Huang, Y. Yu, H.H. Tan, C. Jagadish, L. Fu, Review on III–V semiconductor nanowire array infrared photodetectors, Adv. Mater. Technol. 8 (2023) 2202126, https://doi.org/10.1002/admt.202202126. (Accessed 22 July 2026).
[110] S.T. Oyinbo, T.C. Jen, Reactive molecular dynamics simulations of nickel-based heterometallic catalysts for hydrogen evolution in an alkaline KOH solution, Comput. Mater. Sci. 201 (2022) 110860, https://doi.org/10.1016/j.commatsci.2021.110860.
[111] Y. Sun, B. Sun, J. He, C. Wang, Compositional and structural engineering of inorganic nanowires toward advanced properties and applications, InfoMat 1 (2019) 496–524, https://doi.org/10.1002/inf2.12049.
[112] S.J. Calero-Barney, A.C. Nouduri, A.N. Andriotis, M. Menon, M.K. Sunkara, Dilute anion alloyed III-Nitride nanowires for photoelectrochemical water splitting, Energy Adv 4 (2025) 699–707, https://doi.org/10.1039/D4YA00584H.
[113] C.B. Maliakkal, others, In situ analysis of catalyst composition during gold-catalyzed GaAs nanowire growth, Nat. Commun. 10 (2019) 4577, https://doi.org/10.1038/s41467-019-12437-6.
[114] L.S.K.A. Dick, C. Thelander, P. Caroff, Crystal phase engineering in single InAs nanowires, Nano Lett 10 (2010) 3494–3499, https://doi.org/10.1021/nl101632a.
[115] Q. Joyce, J. Wong-Leung, C. Jagadish, Phase perfection in zinc blende and wurtzite III-V nanowires using basic growth parameters, Nano Lett 10 (2010) 908–915, https://doi.org/10.1021/nl903688v.
[116] H.I. Jang, others, J. Johansson, J. Bolinsson, M. Ek, P. Caroff, K.A. Dick, Combinatorial approaches to understanding polytypism in III-V nanowires, ACS Nano 6 (2012) 6142–6149, https://doi.org/10.1021/nn301477x.
[117] P. Caroff, others, Controlled polytypic and twin-plane superlattices in III-V nanowires, Nat. Nanotechnol. 4 (2009) 50–55, https://doi.org/10.1038/nnano.2008.359.
[118] I. Makhfudz, H. Esmaielpour, Y. Hajati, G. Koblmüller, N. Cavassilas, Interplay of electron trapping by defect midgap state and quantum confinement to optimize the hot-carrier effect in a nanowire structure, Phys. Rev. B 110 (2024), https://doi.org/10.1103/PHYSREVB.110.L121302.
[119] E.M. Grumstrup, M.M. Gabriel, E.M. Cating, C.W. Pinion, J.D. Christesen, J. R. Kirschbrown, E.L. Vallorz, J.F. Cahoon, J.M. Papanikolas, Ultrafast carrier dynamics in individual silicon nanowires: characterization of diameter-dependent carrier lifetime and surface recombination with pump-probe microscopy, J. Phys. Chem. C 118 (2014) 8634–8640, https://doi.org/10.1021/jp502737e.
[120] T.A. Pham, A. Qamar, T. Dinh, M.K. Masud, M. Rais-Zadeh, D.G. Senesky, Y. Yamauchi, N.T. Nguyen, H.P. Phan, Nanoarchitectonics for wide bandgap semiconductor nanowires: toward the next generation of nanoelectromechanical systems for environmental monitoring, Adv. Sci. 7 (2020) 2001294, https://doi.org/10.1002/ADVS.202001294.
[121] Bandgap engineering of (BixIn1-x)2S3 nanowires for wide-spectrum photodetection, Adv. Funct. Mater. 33 (2023) 2306077, https://doi.org/10.1002/adfm.202306077.
[122] J. Wallentin, others, Bandgap engineering in III-V nanowires for tandem solar cells, Nat. Energy (2017), https://doi.org/10.1038/nenergy.2017.109.
[123] N. Jeon, others, Alloy fluctuations act as quantum-dot-like emitters in GaAs-Based nanowires, ACS Nano 9 (2015), https://doi.org/10.1021/acsnano.5b04070.
[124] F. Glas, Strain in nanowires and nanowire heterostructures, Semicond. Semimetals 93 (2015) 79–123, https://doi.org/10.1016/bs.semsem.2015.09.004.
[125] F. Grönqvist, N. Søndergaard, H.Q. Xu, Strain in semiconductor core-shell nanowires, J. Appl. Phys. 106 (2009) 53508, https://doi.org/10.1063/1.3207838.
[126] N. Han, J.J. Hou, F. Wang, S. Yip, Y.T. Yen, Z.X. Yang, G. Dong, T. Hung, Y. L. Chueh, J.C. Ho, GaAs nanowires: from manipulation of defect formation to controllable electronic transport properties, ACS Nano 7 (2013) 9138–9146, https://doi.org/10.1021/NN403767J.
[127] S.A. Dayeh, J. Wang, N. Li, J.Y. Huang, A.V. Gin, S.T. Picraux, Growth, defect formation, and morphology control of germanium-silicon semiconductor nanowire heterostructures, Nano Lett 11 (2011) 4200–4206, https://doi.org/10.1021/nl202126q.
[128] C.K. Groschner, others, Machine-learning pipeline for segmentation and defect identification in high-resolution transmission electron microscopy, Microsc. Microanal. (2021), https://doi.org/10.1017/S1431927621000184.
[129] H. Schmid, others, Doping limits of grown in situ doped silicon nanowires using phosphine, Nano Lett 9 (2009) 173–177, https://doi.org/10.1021/nl802739v.
[130] X. Yang, A. Wolcott, G. Wang, A. Sobo, R.C. Fitzmorris, F. Qian, J.Z. Zhang, Y. Li, Nitrogen-doped ZnO nanowire arrays for photoelectrochemical water splitting, Nano Lett 9 (2009) 2331–2336, https://doi.org/10.1021/nl900772q.
[131] N.A.E. Durgun, D. Çakır, S. Ciraci, Atomic and electronic structures of doped silicon nanowires: a first-principles study, Phys. Rev. B 76 (2007) 245323, https://doi.org/10.1103/PhysRevB.76.245323.
[132] A. Katzenmeyer, F. Léonard, D.L. Huffaker, Observation of free-carrier concentration gradients and surface effects in semiconductor nanowires by infrared spectroscopy, Nano Lett (2011), https://doi.org/10.1021/nl201225q.
[133] G. Dong, F. Liu, J. Liu, H. Zhang, M. Zhu, Realization of radial p-n junction silicon nanowire solar cell based on low-temperature and shallow phosphorus doping, Nanoscale Res. Lett. 8 (2013) 1–17, https://doi.org/10.1186/1556-276X-8-544.
[134] N. Shibata, others, Imaging of Built-In electric field at a p-n junction by scanning transmission electron microscopy, Sci. Rep. 5 (2015) 10040, https://doi.org/10.1038/srep10040.
[135] M. Kim, J. Kwon, H.J. Lee, K.S. Park, J. Kim, J. Kim, K. Baek, H. Yuan, J.K. Hyun, Y.S. Cho, J. Yeom, D.H. Kim, Bespoke selenium nanowires with comprehensive piezo-phototronic effects as viable p-type semiconductor-based piezo-photocatalysts, Nano Energy 114 (2023), https://doi.org/10.1016/j.nanoen.2023.108680.
[136] Different doping behaviors of silicon in zinc-blende and wurtzite GaAs nanowires, ACS Appl. Nano Mater. 6 (2023), https://doi.org/10.1021/acsanm.3c01493.
[137] W. Kim, L. Güniat, A. Fontcuberta I Morral, V. Piazza, Doping challenges and pathways to industrial scalability of III-V nanowire arrays, Appl. Phys. Rev. 8 (2021), https://doi.org/10.1063/5.0031549.
[138] M. Akbari-Saatlu, M. Procek, C. Mattsson, G. Thungström, H.-E. Nilsson, W. Xiong, B. Xu, Y. Li, H.H. Radamson, Silicon nanowires for gas sensing: a review, Nanomater. (Basel, Switzerland) 10 (2020) 1–57, https://doi.org/10.3390/nano10112215.
[139] S. Raman, A. Ravi Sankar, M. Sindhuja, Advances in silicon nanowire applications in energy generation, storage, sensing, and electronics: a review, Nanotechnology 34 (2023), https://doi.org/10.1088/1361-6528/ACB320.
[140] L. Bu, others, Surface engineering of hierarchical platinum-cobalt nanowires for efficient electrocatalysis, Nat. Commun. 7 (2016) 11850, https://doi.org/10.1038/ncomms11850.
[141] K. Jeong, P.R. Deshmukh, J. Park, Y. Sohn, W.G. Shin, ZnO-TiO2 core-shell nanowires: a sustainable photoanode for enhanced photoelectrochemical water

splitting, ACS Sustain. Chem. Eng. 6 (2018) 6518–6526, https://doi.org/10.1021/ACSSUSCHEMENG.8B00324.
[142] K.S. Pasupuleti, R.A. Jayarathna, S.Y. Hwang, P. Thi Minh Thu, D. Vidyasagar, Y. H. Shim, E.T. Kim, Y. Sohn, Y.H. Kim, M.D. Kim, NiO@GaN nanorods-based core-shell heterostructure for enhanced photoelectrochemical water splitting via efficient charge separation, J. Alloys Compd. 1009 (2024) 176882, https://doi.org/10.1016/j.jallcom.2024.176882.
[143] M.S. Gudiksen, L.J. Lauhon, J. Wang, D.C. Smith, C.M. Lieber, Growth of nanowire superlattice structures for nanoscale photonics and electronics, Nature 415 (2002) 617–620, https://doi.org/10.1038/415617a.
[144] M.T. Björk, B.J. Ohlsson, T. Sass, A.I. Persson, C. Thelander, M.H. Magnusson, K. Deppert, L.R. Wallenberg, L. Samuelson, One-dimensional heterostructures in semiconductor nanowhiskers, Appl. Phys. Lett. 80 (2002) 1058–1060, https://doi.org/10.1063/1.1447312.
[145] M. Oliva, G. Gao, E. Luna, L. Geelhaar, R.B. Lewis, Axial GaAs/Ga(As,Bi) nanowire heterostructures, Nanotechnology 30 (2019) 425601, https://doi.org/10.1088/1361-6528/AB3209.
[146] F. Glas, Critical dimensions for the plastic relaxation of strained axial heterostructures in free-standing nanowires, Phys. Rev. B 74 (2006) 121302, https://doi.org/10.1103/PhysRevB.74.121302.
[147] E.C. Garnett, P. Yang, Silicon nanowire radial p-n junction solar cells, J. Am. Chem. Soc. 130 (2008) 9224–9225, https://doi.org/10.1021/ja8032907.
[148] N.M. Ali, N.K. Allam, A.M. Abdel Haleem, N.H. Rafat, Analytical modeling of the radial p-n junction nanowire solar cells, J. Appl. Phys. 116 (2014) 24308, https://doi.org/10.1063/1.4886596.
[149] Constructing 3D branched nanowire-coated macroporous electrodes for solar-energy conversion, Angew. Chemie Int. Ed. (2014), https://doi.org/10.1002/anie.201402371.
[150] G. Zhang, T. Wang, X. Yu, H. Zhang, H. Duan, B. Lu, Nanoforest of hierarchical Co3O4@NiCo2O4 nanowire arrays for high-performance supercapacitors, Nano Energy 2 (2013) 586–594, https://doi.org/10.1016/j.nanoen.2013.07.008.
[151] A. Abdullah, F. Tariq, M.A. Kulkarni, H. Thaalbi, J.S. Ha, J. Key Lee, S.W. Ryu, High-efficiency entangled hierarchical GaN nanowire-based photoanode for solar-driven water splitting, Appl. Surf. Sci. 643 (2024), https://doi.org/10.1016/j.apsusc.2023.158647.
[152] L. Yang, others, High Thermoelectric Figure of Merit of Porous Si Nanowires from Wafer-Scale Assemblies, Nat. Commun. 12 (2021) 3926, https://doi.org/10.1038/s41467-021-24208-3.
[153] S. Ortaboy, J.P. Alper, F. Rossi, G. Bertoni, G. Salviati, C. Carraro, R. Maboudian, MnOx-decorated carbonized porous silicon nanowire electrodes for high performance supercapacitors, Energy Environ. Sci. 10 (2017) 1505–1516, https://doi.org/10.1039/C7EE00977A.
[154] H.L.L. Shen, Q. Che, X. Zhang, Mesoporous NiCo2O4 nanowire arrays grown on carbon textiles as binder-free flexible electrodes for energy storage, Adv. Funct. Mater. 24 (2014) 2630–2637, https://doi.org/10.1002/adfm.201303138.
[155] Y. Chen, J. Kang, M. Zou, K. Wang, M. Liu, W. Li, Porous carbon nanorods encapsulating bismuth nanoparticles promote p-Si nanowire array for photoelectrocatalytic CO2 reduction to formate, Ind. Eng. Chem. Res. 63 (2024) 21831–21840, https://doi.org/10.1021/ACS.IECR.4C03361.
[156] A. Lecestre, M. Martin, F. Cristiano, T. Baron, G. Larrieu, Large-scale monolithic fabrication of III–V vertical nanowires on a standard Si(100) microelectronic substrate, ACS Omega 7 (2022) 5836–5843, https://doi.org/10.1021/ACSOMEGA.1C05876.
[157] T. Ozel, B.A. Zhang, R. Gao, R.W. Day, C.M. Lieber, D.G. Nocera, Electrochemical deposition of conformal and functional layers on high aspect ratio silicon micro/nanowires, Nano Lett 17 (2017) 4502–4507, https://doi.org/10.1021/ACS.NANOLETT.7B01950.
[158] A.I. Hochbaum, R. Chen, R.D. Delgado, W. Liang, E.C. Garnett, M. Najarian, A. Majumdar, P. Yang, R. Hochbaum, R. Chen, P. Yang, Enhanced thermoelectric performance of rough silicon nanowires, Nature 451 (2008) 163–167, https://doi.org/10.1038/nature06381.
[159] F. Domínguez-Adame, M. Martín-González, D. Sánchez, A. Cantarero, Nanowires: a route to efficient thermoelectric devices, Phys. E Low-Dimensional Syst. Nanostructures 113 (2019) 213–225, https://doi.org/10.1016/j.physe.2019.03.021.
[160] G. Latronico, H. Asnaashari Eivari, P. Mele, M.H.N. Assadi, Insights into one-dimensional thermoelectric materials: a concise review of nanowires and nanotubes, Nanomaterials 14 (2024) 1272, https://doi.org/10.3390/NANO14151272.
[161] H. Fang, Y. Wu, Telluride nanowire and nanowire heterostructure-based thermoelectric energy harvesting, J. Mater. Chem. A 2 (2014) 6004–6014, https://doi.org/10.1039/C3TA14129B.
[162] A. Singh, X. Li, V. Protasenko, G. Galantai, M. Kuno, H.G. Xing, D. Jena, Polarization-Sensitive Nanowire Photodetectors Based on Solution-Synthesized {CdSe} Quantum-Wire Solids, Nano Lett 7 (2007) 2999–3006, https://doi.org/10.1021/nl0713023.
[163] A. Mannodi-Kanakkithodi, A guide to discovering next-generation semiconductor materials using atomistic simulations and machine learning, Comput. Mater. Sci. 243 (2024), https://doi.org/10.1016/j.commatsci.2024.113108.
[164] D. Nozaki, J. Kunstmann, F. Zörgiebel, W.M. Weber, T. Mikolajick, G. Cuniberti, Multiscale modeling of nanowire-based Schottky-barrier field-effect transistors for sensorapplications, Nanotechnology 22 (2011) 325703, https://doi.org/10.1088/0957-4484/22/32/325703.
[165] S.K. Achar, J.A. Keith, Small data machine learning approaches in molecular and materials science, Chem. Rev. 124 (2024) 13571–13573, https://doi.org/10.1021/acs.chemrev.4c00957.
[166] S.V. Kalinin, D. Mukherjee, K. Roccapriore, B.J. Blaiszik, A. Ghosh, M. A. Ziatdinov, A. Al-Najjar, C. Doty, S. Akers, N.S. Rao, J.C. Agar, S.R. Spurgeon, Machine learning for automated experimentation in scanning transmission electron microscopy, Npj Comput. Mater. 9 (2023) 227, https://doi.org/10.1038/s41524-023-01142-0.
[167] S. V Kalinin, others, Machine learning in scanning transmission electron microscopy, Nat. Rev. Methods Prim. 2 (2022) 43, https://doi.org/10.1038/s43586-022-00095-w.
[168] M. Hachhach, S. Bayou, A. El Kasmi, M.Z. Saidi, H. Akram, M. Hanafi, O. Achak, C. El Moujahid, T. Chafik, Towards sustainable Scaling-Up of nanomaterials fabrication: current situation, challenges, and future perspectives, Eng 6 (2025) 149, https://doi.org/10.3390/eng6070149.
[169] L. Ndlwana, N. Raleie, K.M. Dimpe, H.F. Ogutu, E.O. Oseghe, M.M. Motsa, T.A. M. Msagati, B.B. Mamba, Sustainable hydrothermal and solvothermal synthesis of advanced carbon materials in multidimensional applications: a review, Materials (Basel) 14 (2021) 5094, https://doi.org/10.3390/MA14175094.
[170] B. Shim, K.R. Park, H. Kim, C. Kim, Y. Song, W.B. Kim, Scalable fabrication of ultra-long silicon nanowires via H_2O_2-enhanced MACE for flexible hydrogen sensors, Chem. Eng. J. 520 (2025) 165632, https://doi.org/10.1016/j.cej.2025.165632.
[171] B.S.P.W. Leu, K. Cho, P.W. Leu, B. Shan, K. Cho, Surface chemical control of the electronic structure of silicon nanowires: density functional calculations, Phys. Rev. B 73 (2006) 195320, https://doi.org/10.1103/PhysRevB.73.195320.
[172] L. Balaghi, others, G. Bussone, R. Grifone, R. Hübner, J. Grenzer, M. Ghorbani-Asl, A.V. Krasheninnikov, H. Schneider, M. Helm, E. Dimakis, Widely tunable GaAs bandgap via strain engineering in core/shell nanowires with large lattice mismatch, Nat. Commun. 10 (2019) 2793, https://doi.org/10.1038/s41467-019-10654-7.
[173] D.X.T. Lookman, P.V. Balachandran, R. Yuan, T. Lookman, P.V. Balachandran, D. Xue, R. Yuan, Active learning in materials science with emphasis on adaptive sampling using uncertainties for targeted design, Npj Comput. Mater. 5 (2019) 21, https://doi.org/10.1038/s41524-019-0153-8.
[174] E. Stach, B. DeCost, A.G. Kusne, J. Hattrick-Simpers, K.A. Brown, K.G. Reyes, J. Schrier, S. Billinge, T. Buonassisi, I. Foster, C.P. Gomes, J.M. Gregoire, A. Mehta, J. Montoya, E. Olivetti, C. Park, E. Rotenberg, S.K. Saikin, S. Smullin, V. Stanev, B. Maruyama, others, Autonomous experimentation systems for materials development: a community perspective, Matter 4 (2021) 2702–2726, https://doi.org/10.1016/j.matt.2021.06.036.
[175] A.A. Volk, M. Abolhasani, Performance metrics to unleash the power of self-driving labs in chemistry and materials science, Nat. Commun. 15 (2024) 1378, https://doi.org/10.1038/s41467-024-45569-5.
[176] Y. Cui, C.M. Lieber, Functional nanoscale electronic devices assembled using silicon nanowire building blocks, Science (80) 291 (2001) 851–853, https://doi.org/10.1126/science.291.5505.851.
[177] F. Patolsky, G. Zheng, C.M. Lieber, Nanowire-based biosensors, Anal. Chem. 78 (2006) 4260–4269, https://doi.org/10.1021/AC069419J.
[178] P.J. Pauzauskie, P. Yang, Nanowire photonics, Mater. Today 9 (2006) 36–45, https://doi.org/10.1016/S1369-7021(06)71652-2.
[179] R.E. Algra, M.A. Verheijen, M.T. Borgström, L.F. Feiner, G. Immink, W.J.P. Van Enckevort, E. Vlieg, E.P.A.M. Bakkers, Twinning superlattices in indium phosphide nanowires, Nat 456 (2008) 369–372, https://doi.org/10.1038/nature07570.
[180] J. Goldberger, A.I. Hochbaum, R. Fan, P. Yang, Silicon vertically integrated nanowire field effect transistors, Nano Lett 6 (2006) 973–977, https://doi.org/10.1021/NL060166J.
[181] R. Agarwal, C.M. Lieber, Semiconductor nanowires: optics and optoelectronics, Appl. Phys. A 85 (2006) 209–215, https://doi.org/10.1007/S00339-006-3720-Z.
[182] Z.L. Wang, Zinc oxide nanostructures: growth, properties and applications, J. Phys. Condens. Matter 16 (2004) R829, https://doi.org/10.1088/0953-8984/16/25/R01.
[183] M.A. Van Huis, N.P. Young, G. Pandraud, J.F. Creemer, D. Vanmaekelbergh, A. I. Kirkland, H.W. Zandbergen, Atomic maging of phase transitions and morphology transformations in nanocrystals, Adv. Mater. 21 (2009) 4992–4995, https://doi.org/10.1002/adma.200902561.
[184] J.R. Jinschek, Advances in the environmental transmission electron microscope (ETEM) for nanoscale in situ studies of gas-solid interactions, Chem. Commun. 50 (2014) 2696–2706, https://doi.org/10.1039/C3CC49092K.
[185] F.M. Ross, Opportunities and challenges in liquid cell electron microscopy, Science (80) (2015) 350, https://doi.org/10.1126/science.aaa9886.
[186] K.W. Urban, J. Barthel, L. Houben, C.L. Jia, L. Jin, M. Lentzen, S.B. Mi, A. Thust, K. Tillmann, Progress in atomic-resolution aberration corrected conventional transmission electron microscopy (CTEM), Prog. Mater. Sci. 133 (2023) 101037, https://doi.org/10.1016/J.PMATSCI.2022.101037.
[187] J.M. Sojo-Gordillo, Y. Kaur, S. Tachikawa, N. Alayo, M. Salleras, N. Forrer, L. Fonseca, A. Morata, A. Tarancón, I. Zardo, TEM-compatible microdevice for the complete thermoelectric characterization of epitaxially integrated Si-based nanowires, Nanoscale Horizons 9 (2024) 1200–1210, https://doi.org/10.1039/D4NH00114A.
[188] P.A. Midgley, R.E. Dunin-Borkowski, Electron tomography and holography in materials science, Nat. Mater. 8 (2009) 271–280, https://doi.org/10.1038/NMAT2406;KWRD.
[189] L. Balaghi, S. Shan, I. Fotev, F. Moebus, R. Rana, T. Venanzi, R. Hübner, T. Mikolajick, H. Schneider, M. Helm, A. Pashkin, E. Dimakis, High electron mobility in strained GaAs nanowires, Nat. Commun. 12 (2021), https://doi.org/10.1038/S41467-021-27006-Z.

[190] J. Jo, Y. Tchoe, G.C. Yi, M. Kim, Real-time characterization using in situ RHEED transmission mode and TEM for investigation of the growth behaviour of nanomaterials, Sci. Rep. 8 (2018), https://doi.org/10.1038/S41598-018-19857-2.
[191] C. Shen, M. Ge, L. Luo, X. Fang, Y. Liu, A. Zhang, J. Rong, C. Wang, C. Zhou, In situ and Ex situ TEM study of lithiation behaviours of porous silicon nanostructures, Sci. Rep. 6 (2016), https://doi.org/10.1038/SREP31334.
[192] Y. Wu, P. Yang, Direct observation of vapor-liquid-solid nanowire growth, J. Am. Chem. Soc. 123 (2001) 3165–3166, https://doi.org/10.1021/ja0059084.
[193] Y. Cui, L.J. Lauhon, M.S. Gudiksen, J. Wang, C.M. Lieber, Diameter-controlled synthesis of single-crystal silicon nanowires, Appl. Phys. Lett. 78 (2001) 2214–2216, https://doi.org/10.1063/1.1363692.
[194] D.A. Muller, Structure and bonding at the atomic scale by scanning transmission electron microscopy, Nat. Mater. 8 (2009) 263–270, https://doi.org/10.1038/NMAT2380;KWRD.
[195] P.E. Batson, N. Dellby, O.L. Krivanek, Sub-ångstrom resolution using aberration corrected electron optics, Nat 418 (2002) 617–620, https://doi.org/10.1038/nature00972.
[196] O.L. Krivanek, M.F. Chisholm, V. Nicolosi, T.J. Pennycook, G.J. Corbin, N. Dellby, M.F. Murfitt, C.S. Own, Z.S. Szilagyi, M.P. Oxley, S.T. Pantelides, S.J. Pennycook, Atom-by-atom structural and chemical analysis by annular dark-field electron microscopy, Nature 464 (2010) 571–574, https://doi.org/10.1038/NATURE08879.
[197] R.F. Egerton, Electron energy-loss spectroscopy in the TEM, Reports Prog. Phys. 72 (2008) 016502, https://doi.org/10.1088/0034-4885/72/1/016502.
[198] S.V. Prikhodko, S. Sitzman, V. Gambin, S. Kodambaka, In situ electron backscattered diffraction of individual GaAs nanowires, Ultramicroscopy 109 (2008) 133–138, https://doi.org/10.1016/j.ultramic.2008.09.006.
[199] T.B. Britton, J. Jiang, Y. Guo, A. Vilalta-Clemente, D. Wallis, L.N. Hansen, A. Winkelmann, A.J. Wilkinson, Tutorial: crystal orientations and EBSD — or which way is up? Mater. Charact. 117 (2016) 113–126, https://doi.org/10.1016/J.MATCHAR.2016.04.008.
[200] N.W. Gregory, Elements of X-Ray diffraction, J. Am. Chem. Soc. 79 (2002) 1773–1774, https://doi.org/10.1021/JA01564A077.
[201] A.J. Wilkinson, T. Ben Britton, Strains, planes, and EBSD in materials science, Mater. Today 15 (2012) 366–376, https://doi.org/10.1016/S1369-7021(12)70163-3.
[202] F. Adams, X-Ray absorption and diffraction - overview, Encycl. Anal. Sci. (2004) 365–377, https://doi.org/10.1016/B0-12-369397-7/00668-3. Second Ed.
[203] C. Ophus, Four-dimensional scanning transmission electron microscopy (4D-STEM): from scanning nanodiffraction to ptychography and beyond, Microsc. Microanal. 25 (2019) 563–582, https://doi.org/10.1017/S1431927619000497.
[204] C.C. Chen, C. Zhu, E.R. White, C.Y. Chiu, M.C. Scott, B.C. Regan, L.D. Marks, Y. Huang, J. Miao, Three-dimensional imaging of dislocations in a nanoparticle at atomic resolution, Nat 496 (2013) 74–77, https://doi.org/10.1038/nature12009.
[205] P. Ercius, O. Alaidi, M.J. Rames, G. Ren, Electron tomography: a three-dimensional analytic tool for hard and soft materials research, Adv. Mater. 27 (2015) 5638–5663, https://doi.org/10.1002/adma.201501015.
[206] R.M. Neal, Pattern recognition and machine learning, J. Electron. Imaging 16 (2006) 049901, https://doi.org/10.1117/1.2819119.
[207] M.L. Taheri, E.A. Stach, I. Arslan, P.A. Crozier, B.C. Kabius, T. LaGrange, A. M. Minor, S. Takeda, M. Tanase, J.B. Wagner, R. Sharma, Current status and future directions for in situ transmission electron microscopy, Ultramicroscopy 170 (2016) 86–95, https://doi.org/10.1016/J.ULTRAMIC.2016.08.007.
[208] J. Madsen, P. Liu, J. Schiøtz, A deep learning approach to identify local structures in atomic-resolution transmission electron microscopy images, Adv. Theory Simulations 1 (2018) 1800037, https://doi.org/10.1002/adts.201800037.
[209] D.A. Muller, L. Fitting Kourkoutis, M. Murfitt, J.H. Song, H.Y. Hwang, J. Silcox, N. Dellby, O.L. Krivanek, Atomic-scale chemical imaging of composition and bonding by aberration-corrected microscopy, Science (80) 319 (2008) 1073–1076, https://doi.org/10.1126/SCIENCE.1148820.
[210] D. Dávila, A. Tarancón, C. Calaza, M. Salleras, M. Fernández-Regúlez, A. San Paulo, L. Fonseca, Monolithically integrated thermoelectric energy harvester based on silicon nanowire arrays for powering micro/nanodevices, Nano Energy 1 (2012) 812–819, https://doi.org/10.1016/J.NANOEN.2012.06.006.
[211] S. Dogan, S. Kudera, Z. Dang, F. Palazon, U. Petralanda, S. Artyukhin, L. De Trizio, L. Manna, R. Krahne, Lateral epitaxial heterojunctions in single nanowires fabricated by masked cation exchange, Nat. Commun. 91 (9) (2018), https://doi.org/10.1038/s41467-018-02878-w, 505-.
[212] M.S. Seifner, M. Sistani, F. Porrati, G. Di Prima, P. Pertl, M. Huth, A. Lugstein, S. Barth, Direct synthesis of hyperdoped germanium nanowires, ACS Nano 12 (2018) 1236, https://doi.org/10.1021/ACSNANO.7B07248.
[213] L. Zhu, others, Piezo-phototronic effect enhanced flexible solar cells based on n-ZnO/p-SnS core-shell nanowire arrays, Adv. Sci. (2017) 1600185, https://doi.org/10.1002/advs.201600185.
[214] M. Bosman, V.J. Keast, Optimizing EELS acquisition, Ultramicroscopy 108 (2008) 837–846, https://doi.org/10.1016/J.ULTRAMIC.2008.02.003.
[215] S. Hofmann, Auger- and X-Ray photoelectron spectroscopy in, Materials Science 49 (2013), https://doi.org/10.1007/978-3-642-27381-0.
[216] J.F. Moulder, W.F. Stickle, P.E. Sobol, K.D. Bomben, J. Chastain, Handbook of X-ray Photoelectron Spectroscopy A Reference Book of Standard Spectra for Identification and Interpretation of XPS Data, (n.d.).
[217] J.E. Castle, in: D. Briggs, M.P. Seah (Eds.), Practical Surface Analysis by Auger and X-ray Photoelectron Spectroscopy, John Wiley and Sons Ltd, Chichester, 1983, p. 533, https://doi.org/10.1002/SIA.740060611. £44.50, Surf. Interface Anal. 6 (1984) 302–302.
[218] J.C. Vickerman, Secondary Ion Mass spectrometry–basic Concepts, Instrumental Aspects, Applications and Trends, A. BENNINGHOVEN, F. G. RUDENAUER and H. W. WERNER, Wiley, John Wiley & Sons, Ltd, New York, 1987, p. 1277, https://doi.org/10.1002/SIA.740100811.
[219] T. Van Acker, S. Theiner, E. Bolea-Fernandez, F. Vanhaecke, G. Koellensperger, Inductively coupled plasma mass spectrometry, Nat. Rev. Methods Prim. 31 (3) (2023) 52, https://doi.org/10.1038/s43586-023-00235-w.
[220] Beer, Bestimmung der Absorption des rothen Lichts in farbigen Flüssigkeiten, Ann. Phys. 162 (1852) 78–88, https://doi.org/10.1002/andp.18521620505.
[221] Y.S. Chen, P.Y. Liu, R. Niu, A. Devaraj, H.W. Yen, R.K.W. Marceau, J.M. Cairney, Atom probe tomography for the observation of hydrogen in materials: a review, Microsc. Microanal. 29 (2023) 1–15, https://doi.org/10.1093/micmic/ozac005.
[222] D. J, A. M, C. Jj, H. Jc, L. J, M. Aw, S. P, Cryo-electron microscopy of vitrified specimens, Q. Rev. Biophys. 21 (1988) 129–228, https://doi.org/10.1017/S0033583500004297.
[223] A.L. Patterson, The scherrer formula for X-Ray particle size determination, Phys. Rev. 56 (1939) 978, https://doi.org/10.1103/PhysRev.56.978.
[224] A. Kolmakov, M. Moskovits, Chemical sensing and catalysis by one-dimensional metal-oxide nanostructures, Annu. Rev. Mater. Res. 34 (2004) 151–180, https://doi.org/10.1146/ANNUREV.MATSCI.34.040203.112141.
[225] H.E. Fischer, A.C. Barnes, P.S. Salmon, Neutron and x-ray diffraction studies of liquids and glasses, Reports Prog. Phys. 69 (2005) 233, https://doi.org/10.1088/0034-4885/69/1/R05.
[226] H.N. Chapman, K.A. Nugent, Coherent lensless X-ray imaging, Nat. Photonics 2010 412 (4) (2010) 833–839, https://doi.org/10.1038/nphoton.2010.240.
[227] X. Liang, P.E.J. Rivera-Díaz-del-Castillo, Neutron diffraction, Encycl. Mater. Met. Alloy. (2021) 695–702, https://doi.org/10.1016/B978-0-12-819726-4.00076-4.
[228] A.C. Ferrari, D.M. Basko, Raman spectroscopy as a versatile tool for studying the properties of graphene, Nat. Nanotechnol. 8 (2013) 235–246, https://doi.org/10.1038/nnano.2013.46.
[229] W. Kauschke, M. Cardona, Resonant raman scattering in semiconductors, Phys. Scr. 1989 (1989) 201, https://doi.org/10.1088/0031-8949/1989/T25/036.
[230] C. Thomsen, S. Reich, Double resonant raman scattering in graphite, Phys. Rev. Lett. 85 (2000) 5214, https://doi.org/10.1103/PhysRevLett.85.5214.
[231] L.C. Lew Yan Voon, Y. Zhang, B. Lassen, M. Willatzen, Q. Xiong, P.C. Eklund, Electronic properties of semiconductor nanowires, J. Nanosci. Nanotechnol. 8 (2008) 1–26, https://doi.org/10.1166/jnn.2008.N03.
[232] H.L. Chen, C. Himwas, A. Scaccabarozzi, P. Rale, F. Oehler, A. Lemaître, L. Lombez, J.F. Guillemoles, M. Tchernycheva, J.C. Harmand, A. Cattoni, S. Collin, Determination of n-Type doping level in single GaAs nanowires by cathodoluminescence, Nano Lett 17 (2017) 6667–6675, https://doi.org/10.1021/ACS.NANOLETT.7B02620.
[233] D.D.D. Ma, S.T. Lee, P. Mueller, S.F. Alvarado, Scanning tunneling microscope excited cathodoluminescence from ZnS nanowires, Nano Lett 6 (2006) 926–929, https://doi.org/10.1021/NL052507J.
[234] A.M. Sanchez, J.A. Gott, H.A. Fonseka, Y. Zhang, H. Liu, R. Beanland, Stable defects in semiconductor nanowires, Nano Lett 18 (2018) 3081–3087, https://doi.org/10.1021/ACS.NANOLETT.8B00620.
[235] O. Hultin, G. Otnes, L. Samuelson, K. Storm, Simplifying nanowire hall effect characterization by using a three-probe device design, Nano Lett 17 (2017) 1121–1126, https://doi.org/10.1021/ACS.NANOLETT.6B04723.
[236] O. Hultin, G. Otnes, M.T. Borgström, M. Björk, L. Samuelson, K. Storm, Comparing hall effect and field effect measurements on the same single nanowire, Nano Lett 16 (2015) 205–211, https://doi.org/10.1021/ACS.NANOLETT.5B03496.
[237] K. Storm, F. Halvardsson, M. Heurlin, D. Lindgren, A. Gustafsson, P.M. Wu, B. Monemar, L. Samuelson, Spatially resolved hall effect measurement in a single semiconductor nanowire, Nat. Nanotechnol. 711 (7) (2012) 718–722, https://doi.org/10.1038/nnano.2012.190.
[238] A. Zahmatkeshsaredorahi, R. Millan-Solsona, D.S. Jakob, L. Collins, X.G. Xu, Kelvin probe force microscopy under ambient conditions, Nat. Rev. Methods Prim. 51 (5) (2025), https://doi.org/10.1038/s43586-025-00424-9, 53-.
[239] C.R. Carey, Y. Yu, M. Kuno, G.V. Hartland, Ultrafast transient absorption measurements of charge carrier dynamics in single II−VI nanowires, J. Phys. Chem. C 113 (2009) 19077–19081, https://doi.org/10.1021/JP907147Y.
[240] C.C.L. McCrory, S. Jung, I.M. Ferrer, S.M. Chatman, J.C. Peters, T.F. Jaramillo, Benchmarking hydrogen evolving reaction and oxygen evolving reaction electrocatalysts for solar water splitting devices, J. Am. Chem. Soc. 137 (2015) 4347–4357, https://doi.org/10.1021/JA510442P.
[241] C.C.L. McCrory, S. Jung, J.C. Peters, T.F. Jaramillo, Benchmarking heterogeneous electrocatalysts for the oxygen evolution reaction, J. Am. Chem. Soc. 135 (2013) 16977–16987, https://doi.org/10.1021/JA407115P.
[242] I. Oh, J. Kye, S. Hwang, Enhanced photoelectrochemical hydrogen production from silicon nanowire array photocathode, Nano Lett 12 (2012) 298–302, https://doi.org/10.1021/NL203564S.
[243] C. Tang, L. Gan, R. Zhang, W. Lu, X. Jiang, A.M. Asiri, X. Sun, J. Wang, L. Chen, Ternary FexCo1-xP nanowire array as a robust hydrogen evolution reaction electrocatalyst with Pt-like activity: experimental and theoretical insight, Nano Lett 16 (2016) 6617–6621, https://doi.org/10.1021/ACS.NANOLETT.6B03332.
[244] C. Wei, Z. Wang, K. Otani, D. Hochfilzer, K. Zhang, R. Nielsen, I. Chorkendorff, J. Kibsgaard, Benchmarking electrocatalyst stability for acidic oxygen evolution reaction: the crucial role of dissolved ion concentration, ACS Catal 13 (2023) 14058–14069, https://doi.org/10.1021/ACSCATAL.3C03257.
[245] D. Polcari, P. Dauphin-Ducharme, J. Mauzeroll, Scanning electrochemical microscopy: a comprehensive review of experimental parameters from 1989 to

2015, Chem. Rev. 116 (2016) 13234–13278, https://doi.org/10.1021/ACS.CHEMREV.6B00067.
[246] A.J. Bard, G. Denuault, C. Lee, D. Mandler, D.O. Wipf, Scanning electrochemical microscopy - a new technique for the characterization and modification of surfaces, Acc. Chem. Res. 23 (2002) 357–363, https://doi.org/10.1021/AR00179A002.
[247] G. Kresse, J. Furthmüller, Efficient iterative schemes for ab initio total-energy calculations using a plane-wave basis set, Phys. Rev. B - Condens. Matter Mater. Phys. 54 (1996) 11169–11186, https://doi.org/10.1103/PhysRevB.54.11169.
[248] M. Ziatdinov, others, Deep learning of atomically resolved scanning transmission electron microscopy images: chemical identification and tracking local transformations, ACS Nano 11 (2017) 12742–12752, https://doi.org/10.1021/acsnano.7b07504.
[249] Z. Diao, K. Ueda, L. Hou, F. Li, H. Yamashita, M. Abe, AI-Equipped scanning probe microscopy for autonomous site-specific atomic-level characterization at room temperature, Small Methods 9 (2025) 2400813, https://doi.org/10.1002/SMTD.202400813;PAGEGROUP:STRING:PUBLICATION.
[250] S.V. Kalinin, M. Ziatdinov, J. Hinkle, S. Jesse, A. Ghosh, K.P. Kelley, A.R. Lupini, B.G. Sumpter, R.K. Vasudevan, Automated and autonomous experiments in electron and scanning probe microscopy, ACS Nano 15 (2021) 12604–12627, https://doi.org/10.1021/ACSNANO.1C02104.
[251] L. Qingzhi, B. Yujie, Q. Lanqing, F. Haoran, T. Jianyu, Z. Wei, Z. Chunxiao, Development of a virtual twin model and digital twin system for thermal systems based on multi-reduced order method, Results Eng 27 (2025) 106695, https://doi.org/10.1016/j.rineng.2025.106695.
[252] I. Das, K. Minehisa, F. Ishikawa, P. Parkinson, S. Church, Wafer-scale correlated morphology and optoelectronic properties in GaAs/AlGaAs core-shell nanowires, APL Mater 13 (2025), https://doi.org/10.1063/5.0258062.
[253] B. Rühle, J.F. Krumrey, V.D. Hodoroaba, Workflow towards automated segmentation of agglomerated, non-spherical particles from electron microscopy images using artificial neural networks, Sci. Rep. 11 (2021), https://doi.org/10.1038/S41598-021-84287-6.
[254] A. Bolyachkin, E. Dengina, N. Kulesh, X. Tang, H. Sepehri-Amin, T. Ohkubo, K. Hono, Tomography-based digital twin of Nd-Fe-B permanent magnets, Npj Comput. Mater. 10 (2024), https://doi.org/10.1038/S41524-024-01218-5.
[255] D.X.T. Lookman, P.V. Balachandran, R. Yuan, Active learning in materials science with emphasis on adaptive sampling using uncertainties for targeted design, Npj Comput. Mater. 5 (2019) 21, https://doi.org/10.1038/s41524-019-0153-8.
[256] D. Shakthivel, A.S. Dahiya, R. Mukherjee, R. Dahiya, Inorganic semiconducting nanowires for green energy solutions, Curr. Opin. Chem. Eng. 34 (2021) 100753. https://www.sciencedirect.com/science/article/pii/S221133982100085X. (Accessed 6 July 2026).
[257] K.P. Musselman, A. Wisnet, D.C. Iza, H.C. Hesse, C. Scheu, J.L. MacManus-Driscoll, L. Schmidt-Mende, Strong efficiency improvements in ultra-low-cost inorganic nanowire solar cells, Adv. Mater. 22 (2010), https://doi.org/10.1002/ADMA.201001455.
[258] Y.Z. Long, M. Yu, B. Sun, C.Z. Gu, Z. Fan, Recent advances in large-scale assembly of semiconducting inorganic nanowires and nanofibers for electronics, sensors and photovoltaics, Chem. Soc. Rev. 41 (2012) 4560–4580, https://doi.org/10.1039/C2CS15335A.
[259] Y. Zhang, H. Liu, Nanowires for high-efficiency, low-cost solar photovoltaics, Cryst 9 (2019) 87, https://doi.org/10.3390/CRYST9020087.
[260] F.J. Cabrera-España, B.M.A. Rahman, Optical and electrical analyses of solar cells with a radial PN junction and incorporating an innovative NW design that mimics ARC layers, Nanomaterials 13 (2023) 1649, https://doi.org/10.3390/nano13101649.
[261] K.Q. Peng, S.T. Lee, Silicon nanowires for photovoltaic solar energy conversion, Adv. Mater. 23 (2011) 198–215.
[262] D. Van Dam, N.J.J. Van Hoof, Y. Cui, P.J. Van Veldhoven, E.P.A.M. Bakkers, J. Gómez Rivas, J.E.M. Haverkort, High-efficiency nanowire solar cells with omnidirectionally enhanced absorption due to self-aligned indium-tin-oxide Mie scatterers, ACS Nano 10 (2016) 11414–11419, https://doi.org/10.1021/acsnano.6b06874.
[263] P. Prete, N. Lovergine, High efficiency III-V nanowire solar cells: the road ahead. https://doi.org/10.1088/2399-1984/ae0fee, 2025.
[264] A.H. Trojnar, C.E. Valdivia, R.R. Lapierre, K. Hinzer, J.J. Krich, Optimizations of GaAs nanowire solar cells, IEEE J. Photovoltaics 6 (2016) 1494–1501, https://doi.org/10.1109/JPHOTOV.2016.2600339.
[265] L. Yu, S. Misra, J. Wang, S. Qian, M. Foldyna, J. Xu, Y. Shi, E. Johnson, P.R. I. Cabarrocas, Understanding light harvesting in radial junction amorphous silicon thin film solar cells, Sci. Rep. 4 (2014), https://doi.org/10.1038/SREP04357.
[266] M.D. Ko, T. Rim, K. Kim, M. Meyyappan, C.K. Baek, High efficiency silicon solar cell based on asymmetric nanowire, Sci. Rep. 5 (2015), https://doi.org/10.1038/SREP11646.
[267] Y. Zeng, Q. Ye, W. Shen, Design principles for single standing nanowire solar cells: going beyond the planar efficiency limits, Sci. Rep. 4 (2014), https://doi.org/10.1038/SREP04915.
[268] S.T. Oyinbo, T.C. Jen, Hydrogen evolution reaction in an alkaline environment through nanoscale Ni, Pt, NiO, Fe/Ni and Pt/Ni surfaces: reactive molecular dynamics simulation, Mater. Chem. Phys. 271 (2021) 124886, https://doi.org/10.1016/j.matchemphys.2021.124886.
[269] Y. Xiao, X. Kong, S. Vanka, W.J. Dong, G. Zeng, Z. Ye, K. Sun, I.A. Navid, B. Zhou, F.M. Toma, H. Guo, Z. Mi, Oxynitrides enabled photoelectrochemical water splitting with over 3,000 hrs stable operation in practical two-electrode configuration, Nat. Commun. 14 (2023), https://doi.org/10.1038/S41467-023-37754-9.
[270] F.A. Chowdhury, M.L. Trudeau, H. Guo, Z. Mi, A photochemical diode artificial photosynthesis system for unassisted high efficiency overall pure water splitting, Nat. Commun. 9 (2018), 1707-, https://www.nature.com/articles/s41467-018-04067-1. (Accessed 29 August 2026).
[271] A. Standing, S. Assali, L. Gao, M.A. Verheijen, D. Van Dam, Y. Cui, P.H.L. Notten, J.E.M. Haverkort, E.P.A.M. Bakkers, Efficient water reduction with gallium phosphide nanowires, Nat. Commun. 6 (2015), https://doi.org/10.1038/NCOMMS8824.
[272] W.J. Dong, Y. Xiao, K.R. Yang, Z. Ye, P. Zhou, I.A. Navid, V.S. Batista, Z. Mi, Pt nanoclusters on GaN nanowires for solar-asssisted seawater hydrogen evolution, Nat. Commun. 14 (2023), https://doi.org/10.1038/S41467-023-35782-Z.
[273] K. Sivula, F. Le Formal, M. Grätzel, Solar water splitting: progress using hematite (α-Fe 2O3) photoelectrodes, ChemSusChem 4 (2011) 432–449, https://doi.org/10.1002/cssc.201000416.
[274] H.S. Han, S. Shin, D.H. Kim, I.J. Park, J.S. Kim, P.S. Huang, J.K. Lee, I.S. Cho, X. Zheng, Boosting the solar water oxidation performance of a BiVO4 photoanode by crystallographic orientation control, Energy Environ. Sci. 11 (2018) 1299–1306, https://doi.org/10.1039/C8EE00125A.
[275] X. Chen, X. Li, Y. Peng, H. Yang, Y. Tong, M.S. Balogun, Y. Huang, Tailoring Carrier Dynamics of BiVO4 Photoanode via Dual Incorporation of Au and Co(OH)x Cooperative Modification for Photoelectrochemical Water Splitting, Adv. Funct. Mater. 35 (2025), https://doi.org/10.1002/ADFM.202416091.
[276] S. Anantharaj, S. Kundu, Do the evaluation parameters reflect intrinsic activity of electrocatalysts in electrochemical water splitting? ACS Energy Lett 4 (2019) 1260–1264, https://doi.org/10.1021/ACSENERGYLETT.9B00686.
[277] S. Anantharaj, S. Noda, V.R. Jothi, S.C. Yi, M. Driess, P.W. Menezes, Strategies and perspectives to catch the missing pieces in energy-efficient hydrogen evolution reaction in alkaline media, Angew. Chem. Int. Ed. Engl. 60 (2021) 18981, https://doi.org/10.1002/ANIE.202015738.
[278] Q. Gong, Y. Wang, Q. Hu, J. Zhou, R. Feng, P.N. Duchesne, P. Zhang, F. Chen, N. Han, Y. Li, C. Jin, Y. Li, S.T. Lee, Ultrasmall and phase-pure W2C nanoparticles for efficient electrocatalytic and photoelectrochemical hydrogen evolution, Nat. Commun. 71 (7) (2016), https://doi.org/10.1038/ncomms13216, 13216-.
[279] Y. Pan, H. Zhang, B. Zhang, F. Gong, J. Feng, H. Huang, S. Vanka, R. Fan, Q. Cao, M. Shen, Z. Li, Z. Zou, R. Xiao, S. Chu, Renewable formate from sunlight, biomass and carbon dioxide in a photoelectrochemical cell, Nat. Commun. 141 (14) (2023), https://doi.org/10.1038/s41467-023-36726-3, 1013-.
[280] M. Law, L.E. Greene, A. Radenovic, T. Kuykendall, J. Liphardt, P. Yang, ZnO-Al2O3 and ZnO-TiO2 core-shell nanowire dye-sensitized solar cells, J. Phys. Chem. B 110 (2006) 22652–22663, https://doi.org/10.1021/JP0648644.
[281] S. Li, P. Zhang, X. Song, L. Gao, Photoelectrochemical hydrogen production of TiO2 passivated Pt/Si-nanowire composite photocathode, ACS Appl. Mater. Interfaces 7 (2015) 18560–18565, https://doi.org/10.1021/ACSAMI.5B04936.
[282] D.W. Bahnemann, M. Mohsin, T. Ishaq, I. Ahmad Bhatti, A. Jilani, A.A. Melaibari, N.H. Abu-Hamdeh, Semiconductor nanomaterial photocatalysts for water-splitting hydrogen production: the holy grail of converting solar energy to fuel. https://doi.org/10.3390/nano13030546, 2023.
[283] J. Luo, S. Zhang, M. Sun, L. Yang, S. Luo, J.C. Crittenden, A critical review on energy conversion and environmental remediation of photocatalysts with remodeling crystal lattice, surface, and interface, ACS Nano 13 (2019) 9811–9840, https://doi.org/10.1021/ACSNANO.9B03649.
[284] J. Hong, K.H. Cho, V. Presser, X. Su, Recent advances in wastewater treatment using semiconductor photocatalysts, Curr. Opin. Green Sustain. Chem. 36 (2022) 100644, https://doi.org/10.1016/J.COGSC.2022.100644.
[285] J. Deng, Y. Su, D. Liu, P. Yang, B. Liu, C. Liu, Nanowire photoelectrochemistry, Chem. Rev. 119 (2019) 9221–9259, https://doi.org/10.1021/acs.chemrev.9b00232.
[286] L. Yang, Z. Chen, J. Zhang, C.-A.A. Wang, SrTiO3/TiO2 heterostructure nanowires with enhanced electron-hole separation for efficient photocatalytic activity, Front. Mater. Sci. 13 (2019) 342–351, https://doi.org/10.1007/S11706-019-0477-9.
[287] N.N. Uyen, N.C. Toan, N. Truong, L.A. Tu, P.H. Le, Plasmonic Au–TiO2nanowire/nanotube heterostructures for multifunctional photocatalysis: dye and pesticide degradation, water splitting, and antibacterial activity, Nanoscale Adv 7 (2025) 7317–7332, https://doi.org/10.1039/d5na00765h.
[288] H. Pang, L. Liu, S. Ouyang, H. Xu, Y. Li, D. Wang, Structure, optical properties, and photocatalytic activity towards H2 generation and CO2 reduction of GaN nanowires via vapor-liquid-solid process, Int. J. Photoenergy 2014 (2014) 894396, https://doi.org/10.1155/2014/894396.
[289] X. Guo, Q. Li, Y. Liu, T. Jin, Y. Chen, L. Guo, T. Lian, Enhanced light-driven charge separation and H2Generation efficiency in WSe2Nanosheet-Semiconductor nanocrystal heterostructures, ACS Appl. Mater. Interfaces 12 (2020) 44769–44776, https://doi.org/10.1021/ACSAMI.0C12931.
[290] Z. Chen, G. Zhang, S. Cao, G. Chen, C. Li, R. Izquierdo, S. Sun, Advanced semiconductor catalyst designs for the photocatalytic reduction of CO2, Mater. Reports Energy 3 (2023) 100193, https://doi.org/10.1016/J.MATRE.2023.100193.
[291] S.T. Lee, N. Wang, C.S. Lee, Semiconductor nanowires: synthesis, structure and properties, Mater. Sci. Eng. A 286 (2000) 16–23, https://doi.org/10.1016/S0921-5093(00)00658-4.
[292] A. Conte, M. Baron, S. Bonacchi, S. Antonello, A. Aliprandi, Copper and silver nanowires for CO2 electroreduction, Nanoscale 15 (2023) 3693, https://doi.org/10.1039/D2NR06687D.

[293] L.F. Cui, R. Ruffo, C.K. Chan, H. Peng, Y. Cui, Crystalline-amorphous core−shell silicon nanowires for high capacity and high current battery electrodes, Nano Lett 9 (2008) 491–495, https://doi.org/10.1021/NL8036323.
[294] X. Li, S. Xiong, J. Li, X. Liang, J. Wang, J. Bai, Y. Qian, MnO@carbon core-shell nanowires as stable high-performance anodes for lithium-ion batteries, Chemistry 19 (2013) 11310–11319, https://doi.org/10.1002/CHEM.201203553.
[295] Y. Lei, N. Du, W. Liu, H. Wu, D. Yang, Synthesis of Co/SnO2 core-shell nanowire arrays and their electrochemical performance as anodes of lithium-ion batteries, Ionics 2510 (25) (2019) 4651–4658, https://doi.org/10.1007/S11581-019-03029-X.
[296] C. Yang, K.S.R. Chandran, A critical review of silicon nanowire electrodes and their energy storage capacities in Li-ion cells, RSC Adv 13 (2023), https://doi.org/10.1039/D2RA07326A.
[297] L.F. Cui, Y. Yang, C.M. Hsu, C. Yi, Carbon-silicon Core-shell nanowires as high capacity electrode for lithium lon batteries, Nano Lett 9 (2009) 3370–3374, https://doi.org/10.1021/nl901670t.
[298] L. Fu, X. Zheng, L. Huang, C. Shang, K. Lu, X. Zhang, B. Wei, X. Wang, Synthesis and investigation of CuGeO3 nanowires as anode materials for advanced sodium-ion batteries, Nanoscale Res. Lett. 13 (2018), https://doi.org/10.1186/S11671-018-2609-Z.
[299] L. Huang, W. Zhang, J. Xiang, H. Xu, G. Li, Y. Huang, Hierarchical core-shell NiCo 2 O 4 @NiMoO 4 nanowires grown on carbon cloth as integrated electrode for high-performance supercapacitors, Sci. Rep. 6 (2016), https://doi.org/10.1038/SREP31465.
[300] G. Zhou, L. Xu, G. Hu, L. Mai, Y. Cui, Nanowires for electrochemical energy storage, Chem. Rev. 119 (2019) 11042–11109, https://doi.org/10.1021/ACS.CHEMREV.9B00326.
[301] W. Ye, F. Wu, N. Shi, H. Zhou, Q. Chi, W. Chen, S. Du, P. Gao, H. Li, S. Xiong, Metal–semiconductor phase twinned hierarchical MoS2 nanowires with expanded interlayers for sodium-ion batteries with ultralong cycle life, Small 16 (2020), https://doi.org/10.1002/smll.201906607.
[302] J.M. Tarascon, Na-ion versus Li-ion batteries: complementarity rather than competitiveness, Joule 4 (2020) 1616–1620, https://doi.org/10.1016/j.joule.2020.06.003.
[303] A. Machín, K. Fontánez, J.C. Arango, D. Ortiz, J. De León, S. Pinilla, V. Nicolosi, F. I. Petrescu, C. Morant, F. Márquez, One-dimensional (1d) nanostructured materials for energy applications, Materials (Basel) 14 (2021) 2609, https://doi.org/10.3390/ma14102609.
[304] S. Rai, R. Bhujel, M. Khadka, R.L. Chetry, B.P. Swain, J. Biswas, Synthesis, characterizations, and electrochemical studies of ZnO/reduced graphene oxide nanohybrids for supercapacitor application, Mater. Today Chem. 20 (2021) 100472, https://doi.org/10.1016/J.MTCHEM.2021.100472.
[305] Y. Gan, C. Wang, X. Chen, P. Liang, H. Wan, X. Liu, Q. Tan, H. Wu, H. Rao, H. H. Wang, J. Zhang, Y. Wang, P.A. van Aken, H.H. Wang, High conductivity Ni12P5 nanowires as high-rate electrode material for battery-supercapacitor hybrid devices, Chem. Eng. J. 392 (2020) 123661, https://doi.org/10.1016/J.CEJ.2019.123661.
[306] M. Sun, Z. Li, Q. Fang, S. Han, C. Cai, H. Li, W. Shen, X. Liu, Y. Fu, Room-temperature synthesized porous Cu(OH)2/Cu7S4 hybrid nanowires as a high-performance electrode material for asymmetric supercapacitors, J. Mater. Chem. A 8 (2020) 724–734, https://doi.org/10.1039/c9ta11515c.
[307] H. Wang, J.H. Bahk, C. Kang, J. Hwang, K. Kim, J. Kim, P. Burke, J.E. Bowers, A. C. Gossard, A. Shakouri, W. Kim, Right sizes of nano- and microstructures for high-performance and rigid bulk thermoelectrics, Proc. Natl. Acad. Sci. U. S. A. 111 (2014) 10949–10954, https://doi.org/10.1073/pnas.1403601111.
[308] J.R. Sootsman, H. Kong, C. Uher, J.J. D'Angelo, C.I. Wu, T.P. Hogan, T. Caillat, M. G. Kanatzidis, Large enhancements in the thermoelectric power factor of bulk PbTe at high temperature by synergistic nanostructuring, Angew. Chemie - Int. Ed. 47 (2008) 8618–8622, https://doi.org/10.1002/anie.200803934.
[309] M. Liu, W. Ma, Enhanced thermoelectric performance of PbTe nanocomposites with Sb nanoinclusions, ACS Omega 9 (2024) 17097, https://doi.org/10.1021/ACSOMEGA.3C09241.
[310] J. Zhang, D. Wu, D. He, D. Feng, M. Yin, X. Qin, J. He, Extraordinary thermoelectric performance realized in n-Type PbTe through multiphase nanostructure engineering, Adv. Mater. 29 (2017), https://doi.org/10.1002/ADMA.201703148.
[311] L. Xiao, B. Yin, Z. Geng, J. Li, R. Jia, K. Zhang, Flexible wearable devices based on self-powered energy supply, Nano Energy 142 (2025) 111157, https://doi.org/10.1016/j.nanoen.2025.111157.
[312] K. Manoharan, M. Pumera, Roadmap of flexible electrodes for next-generation wearable electronics, Energy & Fuels 40 (2026) 2319–2337, https://doi.org/10.1021/ACS.ENERGYFUELS.5C05463.
[313] J. Kim, J. Lee, D. Son, M.K. Choi, D.H. Kim, Deformable devices with integrated functional nanomaterials for wearable electronics, Nano Converg 3 (2016) 4, https://doi.org/10.1186/S40580-016-0062-1.
[314] C. Dang, M. Liu, Z. Lin, W. Yan, Selenium nanomaterials enabled flexible and wearable electronics, Chem Synth 314 (3) (2023), https://doi.org/10.20517/CS.2022.33 (2023) N/A-N/A.
[315] H. Kim, K.R. Pyun, M.T. Lee, H.B. Lee, S.H. Ko, Recent advances in sustainable wearable energy devices with nanoscale materials and macroscale structures, Adv. Funct. Mater. 32 (2022) 2110535, https://doi.org/10.1002/ADFM.202110535. ;ISSUE:ISSUE:DOI.
[316] Z. Liu, J. Xu, D. Chen, G. Shen, Flexible electronics based on inorganic nanowires, Chem. Soc. Rev. 44 (2015) 161–192, https://doi.org/10.1039/c4cs00116h.
[317] A. Saha, M.A. Fatin, T. Rahman, M. Hossain, Light trapping and guided mode enhancement in perovskite/Si tandem solar cells with embedded silicon nanowires, RSC Adv 15 (2025) 49063–49073, https://doi.org/10.1039/D5RA07413D.
[318] K. Li, W.J. Dong, Z. Mi, Photoelectrochemical water splitting under concentrated sunlight: best practices and protocols, Front. Energy Res. 13 (2025), https://doi.org/10.3389/fenrg.2025.1550153.
[319] Y. Zhu, L. He, Y. Ni, G. Li, D. Li, W. Lin, Q. Wang, L. Li, H. Yang, Recent progress on photoelectrochemical water splitting of graphitic carbon nitride (g−CN) electrodes, Nanomaterials 12 (2022) 2374, https://doi.org/10.3390/NANO12142374.
[320] S. Choi, J. Hwang, T.H. Lee, H.H. Kim, S.P. Hong, C. Kim, M.J. Choi, H.K. Park, S. S.M. Bhat, J.M. Suh, J. Lee, K.S. Choi, S.H. Hong, J.C. Shin, H.W. Jang, Photoelectrochemical hydrogen production at neutral pH phosphate buffer solution using TiO2 passivated InAs Nanowire/p-Si heterostructure photocathode, Chem. Eng. J. 392 (2020) 123688, https://doi.org/10.1016/j.cej.2019.123688.
[321] G. Otnes, M.T. Borgström, Towards high efficiency nanowire solar cells, Nano Today 12 (2017) 31–45, https://doi.org/10.1016/j.nantod.2016.10.007.
[322] X. Yan, Y. Li, X. Zhang, Semiconductor nanowire heterodimensional structures toward advanced optoelectronic devices, Nanoscale Horizons 10 (2024) 56–77, https://doi.org/10.1039/D4NH00385C.
[323] J. Koch, L. Liborius, P. Kleinschmidt, W. Prost, N. Weimann, T. Hannappel, Impact of the tip-to-semiconductor contact in the electrical characterization of nanowires, ACS Omega 9 (2024) 5788–5797, https://doi.org/10.1021/ACSOMEGA.3C08729.
[324] Y. Wang, Nanowire materials for supercapacitor electrode: preparation, performance and prospects, J. Energy Storage 97 (2024), https://doi.org/10.1016/j.est.2024.112848.
[325] Z. Ren, Z. Ren, Z. Zhang, T. Buonassisi, J. Li, Autonomous experiments using active learning and AI, Nat. Rev. Mater. 8 (2023) 563–564, https://doi.org/10.1038/S41578-023-00588-4.
[326] Y. Xie, K. Sattari, C. Zhang, J. Lin, Toward autonomous laboratories: convergence of artificial intelligence and experimental automation, Prog. Mater. Sci. 132 (2023), https://doi.org/10.1016/j.pmatsci.2022.101043.
[327] G. Tom, S.P. Schmid, S.G. Baird, Y. Cao, K. Darvish, H. Hao, S. Lo, S. Pablo-García, E.M. Rajaonson, M. Skreta, N. Yoshikawa, S. Corapi, G.D. Akkoc, F. Strieth-Kalthoff, M. Seifrid, A. Aspuru-Guzik, Self-driving laboratories for chemistry and materials science, Chem. Rev. 124 (2024) 9633–9732, https://doi.org/10.1021/acs.chemrev.4c00055.
[328] B.G. Pelkie, L.D. Pozzo, The laboratory of Babel: highlighting community needs for integrated materials data management, Digit. Discov. 2 (2023) 544–556, https://doi.org/10.1039/D3DD00022B.
[329] H. Hysmith, E. Foadian, S.P. Padhy, S.V. Kalinin, R.G. Moore, O.S. Ovchinnikova, M. Ahmadi, The future of self-driving laboratories: from human in the loop interactive AI to gamification, Digit. Discov. 3 (2024) 621–636, https://doi.org/10.1039/D4DD00040D.
[330] S. Lo, S.G. Baird, J. Schrier, B. Blaiszik, N. Carson, I. Foster, A. Aguilar-Granda, S. V. Kalinin, B. Maruyama, M. Politi, H. Tran, T.D. Sparks, A. Aspuru-Guzik, Review of low-cost self-driving laboratories in chemistry and materials science: the "frugal twin" concept, Digit. Discov 3 (2024) 842–868, https://doi.org/10.1039/D3DD00223C.
[331] M. Raissi, P. Perdikaris, G.E. Karniadakis, Physics-informed neural networks: a deep learning framework for solving forward and inverse problems involving nonlinear partial differential equations, J. Comput. Phys. 378 (2019) 686–707, https://doi.org/10.1016/J.JCP.2018.10.045.
[332] Y. Wu, B. Sicard, S.A. Gadsden, Physics-informed machine learning: a comprehensive review on applications in anomaly detection and condition monitoring, Expert Syst. Appl. 255 (2024) 124678, https://doi.org/10.1016/J.ESWA.2024.124678.
[333] T. Xie, J.C. Grossman, Crystal graph convolutional neural networks for an accurate and interpretable prediction of material properties, Phys. Rev. Lett. 120 (2018) 145301, https://doi.org/10.1103/PhysRevLett.120.145301.
[334] H. Butler, D.W. Davies, A. Walsh, K.T. Butler, D.W. Davies, H. Cartwright, O. Isayev, A. Walsh, Machine learning for molecular and materials science, Nature 559 (2018) 547–555, https://doi.org/10.1038/s41586-018-0337-2.
[335] S.B.J. Schmidt, M.R.G. Marques, M.A.L. Marques, Recent advances and applications of machine learning in solid-state materials science, Npj Comput. Mater. 5 (2019) 83, https://doi.org/10.1038/s41524-019-0221-0.
[336] M. Abdar, F. Pourpanah, S. Hussain, D. Rezazadegan, L. Liu, M. Ghavamzadeh, P. Fieguth, X. Cao, A. Khosravi, U.R. Acharya, V. Makarenkov, S. Nahavandi, A review of uncertainty quantification in deep learning: techniques, applications and challenges, Inf. Fusion 76 (2021) 243–297, https://doi.org/10.1016/j.inffus.2021.05.008.
[337] M. Grieves, J. Vickers, Digital twin: mitigating unpredictable, undesirable emergent behavior in complex systems, Transdiscipl. Perspect. Complex Syst. New Find. Approaches (2017) 85–113, https://doi.org/10.1007/978-3-319-38756-7_4.
[338] F. Tao, H. Zhang, A. Liu, A.Y.C.C. Nee, Digital twin in industry: State-of-the-art, IEEE Trans. Ind. Informatics 15 (2019) 2405–2415, https://doi.org/10.1109/TII.2018.2873186.
[339] A. Fuller, Z. Fan, C. Day, C. Barlow, Digital twin: enabling technologies, challenges and open research, IEEE Access 8 (2020) 108952–108971, https://doi.org/10.1109/ACCESS.2020.2998358.
[340] M. Gheibi, E. Canga, M. Eldessouki, Life cycle assessment of nanowires for sustainable material production: a systematic review, Results Eng 29 (2026), https://doi.org/10.1016/j.rineng.2025.108300.

[341] J. Silk, S. Beitone, M. Hoque, C. Ternon, D. Evrard, D. Riassetto, Comparative cradle-to-gate life cycle assessment of hydrothermal zinc oxide nanowire synthesis methods, Green Chem 28 (2026) 2429–2439, https://doi.org/10.1039/D5GC03866A.

[342] G. Pallas, M.G. Vijver, W.J.G.M. Peijnenburg, J. Guinée, Ex ante life cycle assessment of GaAs/Si nanowire–based tandem solar cells: a benchmark for industrialization, Int. J. Life Cycle Assess. 25 (2020) 1767–1782, https://doi.org/10.1007/S11367-020-01791-Z.

[343] K. Lan, H.S.H. Wang, T. Lee, C.A. de Assis, R.A. Venditti, Y. Zhu, Y. Yao, A modeling framework to identify environmentally greener and lower-cost pathways of nanomaterials, Green Chem 26 (2024) 3466–3478, https://doi.org/10.1039/D3GC04036D.

[344] V. Sahajwalla, R. Hossain, Rethinking circular economy for electronics, energy storage, and solar photovoltaics with long product life cycles, MRS Bull 48 (2023) 375–385, https://doi.org/10.1557/S43577-023-00519-2.

[345] T. Hummen, A. Sudheshwar, Fitness of product and service design for closed-loop material recycling: a framework and indicator, Resour. Conserv. Recycl. 190 (2023), https://doi.org/10.1016/J.RESCONREC.2022.106661.

[346] A. Kostapanou, K.R. Chatzipanagiotou, S. Damilos, F. Petrakli, E.P. Koumoulos, Safe-and-Sustainable-by-Design framework: (re-)designing the advanced materials lifecycle, Sustain 16 (2024), https://doi.org/10.3390/SU162310439.